同志社大学

DOSHISHA UNIVERSITY

Development of a Low-Voltage Ambient Mobility Spectrometer for Atmospheric Pressure Plasma Diagnostics

---

Plasma Physics Laboratory
Department of Electrical and Electronic Engineering
Graduate School of Science and Engineering

PENADO KEITH NEALSON MONTANEZ
ペーナド キース ニールソン モンタネズ
1416203303

Motoi Wada, Ph.D
和田 元
Adviser

ABSTRACT

Development of a Low-Voltage Ambient Mobility Spectrometer for Atmospheric Pressure Plasma Diagnostics

by PENADO KEITH NEALSON MONTANEZ

Ion mobility spectrometry is a method that allows the measure of ion species in a swarm by analyzing their inherent mobilities. In the spectrometer, the swarm is separated into its discrete components by interacting with a strong electric field, and collisions with the neutral gases. While the method could be applied under vacuum, it is more convenient to perform it at atmospheric pressures allowing faster analysis of large molecules.

The study demonstrate the diagnostics of a capacitively-coupled RF AP source using the low-voltage ambient mobility spectrometer. The design of the compact spectrometer device is similar to that of typical drift tube ion mobility devices. The shutter region contain mesh at the plasma facing side of the spectrometer results to an observed phase-locked signal at the detector. Even in the absence of an electric field, the time varying voltage at the shutter is enough to produce this type of signal at the detector.

The principle for low-electric field ion mobility spectrometry for positively charged species has developed in this study using the asymmetric current behavior. Analysis of the ion transport in the drift field shows the presence of peaks in the time-of-flight spectrum during the positive phase corresponding to the reduced mobilities of 3.0 cm^2/Vs, and 2.7 cm^2/Vs measured at an applied bias of 100, and 5-50 V respectively. The peak could possibly be attributed to the drift of O^+, and Ar^+ ions inside the spectrometer.

The principle for low-electric field mobility spectrometry of electrons has been studied for diagnostics of an atmospheric pressure plasma source. At negative field intensities of 0.33 V/cm -33.3 V/cm the presence of a phase dependant signal relative to the shutter potential is observed. The average electron mobilities measured in this study report mobilities of 81.7, 82.6, and 85 cm^2/Vs corresponding to the 30, 100, and 200 mesh sizes respectively measured at E = 0.33- 33.33 V/cm.

Numerical calculations of the ion transport inside the ambient mobility spectrometer has been conducted using an approximation of the single particle motion of ions, and a collective fluid behavior of the system to simulate the swarm behavior of ion species inside the ambient spectrometer. Diffusive-like behavior of the swarm was observed from the results of the PIC code while the Finite Difference method applied to the 1D Fluid model equation confirms the high-pass filter characteristics of the mesh at low electric fields.

The study is one of the first that discusses measurements of ion mobilities at very low electric fields in the absence of a neutral gas. The proof of concept that this method could be applied at this scale opens up the possibility of expanding the theory even further such that we are able to realize the analysis of trace substances even faster than before.

Acknowledgements

I would like to acknowledge and give my utmost gratitude to my supervisor, Professor Motoi Wada, without whom this research would have not been made possible. His continual presence, insight, and assistance throughout my research and stay here at Doshisha University ultimately resulted to the completion of this project. I will forever be grateful for the many chances, and opportunities that you have given me.

I would also like to recognize the support and contributions of my perpetual co-author and friend, Dr. Allen Vincent Catapang. His experimental expertise and deep understanding of plasma science resulted to various break throughs achieved in this study. Hopefully this would not be the end to our scientific collaboration.

I would like to thank as well the aide of my other Filipino lab members- Dr. James Hernandez, Mr. Jose Abalos, and Ms. Arantxa Montallana for their continuous assistance both inside and outside of the laboratory.

I would also like to give special thanks to my parents- Mrs. Ma. Carmen Penado and Mr. Nestor Penado, to my sisters- Ms. Nestee Marie Penado and Ms. Kristeen Marie Penado, to my aunt- Ms. Erlou Penado, and to my uncles- Mr. Nilo Penado and Mr. Ismael Penado. Their presence, company, and advice over the years helped me to become what I am today.

Finally I would like to give my gratitude to my many international friends I have made over the years here in Kyoto. You are far too many to name but always know that you have too helped me both big and small over the years. From Toriki Doshishamae to Kamogawa to Lake Biwa, I hope that the party does not end here.

From gacha, to beers, to snakes, and all
to cherry blossom springs, and coffee in fall
I left with you a part of me,
and memories that will forever be
I hope this is not the end as it usually is,
but to new beginnings so God help me please

CONTENTS

LIST OF FIGURES

LIST OF TABLES

Chapter 1

INTRODUCTION

Ion mobility spectrometry (IMS) is an electrophoretic method that allows the measurement of ion species in an ionized swarm by analyzing their inherent mobilities [1]. The method involves the separation of the swarm into discrete ion components in the presence of an applied electric field and a neutral gas environment to obtain the components' inherent mobilities. Separation of the swarm is achieved through ion-neutral collisions, while the applied electric field accelerates the discrete ion packets towards the detector where a distinct electronic signal is obtained.

While the method could be applied under vacuum allowing a more controlled environment for accurate measurements of trace ion species, the process has expanded to be done under atmospheric pressures allowing for faster analysis of large molecules such as narcotics, and explosives, and analysis of samples that are difficult to introduce into vacuum systems such as biological samples.

IMS typically requires applied electric fields of about 1- 100 kV/cm to obtain the mobilities of ions. This requirement hinders the design of more compact devices due to the size of the voltage sources needed to produce these fields. The need for an inert buffer gas environment similarly requires additional equipment so that the neutral gas environment can be sustained during spectrometry.

This dissertation presents a novel compact ion mobility spectrometer that is able to obtain the mobilities of charged species at very low electric fields of up to 33.3 V/cm at ambient pressures. The design of the ambient mobility spectrometer does not require any equipment to maintain a neutral buffer gas environment by measuring the mobility of ions in ambient air.

The design involves the addition of a wire mesh at the plasma facing side of the electronic shutter that periodically switches between a low negative, and a high positive potential resulting to a time-resolved detector signal relative to the applied shutter potential. The detector current varies over a range of operating parameters such as the shutter voltage, shutter frequency, and the applied electric field in the drift region. This unique signal allows the measurement of the mobilities of charged species by analyzing the arrival time of charged species based from the first derivative of the signal in these regions.

1.1 Objectives and Motivations

A fast, low-cost method of analyzing trace molecular species such as aromatics and other volatile substances is of interest especially in areas where limited resources are available. The developed low-voltage ambient mobility spectrometer may prove to be useful in these situations. The design of which allows the identification of such substances at a much lower cost than typical mobility spectrometers which are available in the market.

Therefore the research aims to establish the instrumentation, and the corresponding theory of the developed low-voltage ambient mobility spectrometer such that the mobilities of charged species may be obtained from the distinct spectrometer signal.

1.2 Organization

The dissertation consists of five main parts and seven chapters following the introduction. A review on the fundamental theories of atmospheric pressure (AP) plasma, AP plasma diagnostics, and ion mobility spectrometry is described in Chapter 2. Literature discussing the relevant concepts in the dissertation are presented here to lay the theoretical foundation of the research for the reader.

Chapter 3 presents the radio frequency (RF) AP plasma sources developed in this study to serve as the ion/electron sources for IMS. The chapter covers the design, and operation of two RF AP plasma source configurations. These sources were characterized using optical emission spectroscopy and double probe measurements to characterize the produced plasma. By investigating the source characteristics, valuable insights regarding their suitability for integration into the mobility spectrometer are obtained.

Chapter 4 delves into the design of the ambient mobility spectrometer. The chapter aims to establish a clear understanding of the spectrometer's functioning under ambient conditions. The schematic design, and typical operation procedures of the mobility spectrometer is discussed. It was found that the addition of a mesh-type shutter electrode allows the observation of a distinct current signal at the detector. Results of the double probe analysis of the plasma near the mesh electrode vicinity were conducted to clarify the observed phenomena are also presented in this chapter.

In Chapter 5, the spectrometer's operation during the application of a positive electric field to the drift region is investigated. In this particular operation mode, the distinct detector signal observed enables the determination of the ion mobilities of positive ions. In contrast, Chapter 6 focuses on the spectrometer's operation in the presence of a negative electric field. The observed signal in this operation mode allows the measurement of the mobilities of negatively charged species in the ionized swarm which are predominantly electrons.

Numerical calculations on the motion of charged species inside the spectrometer are discussed in Chapter 7. Utilizing the equation of motions, the motion of a charged particle given a electrostatic potential distribution of the spectrometer and the neighboring charged particle species are obtained. A more efficient simulation model by solving the one dimensional fluid model is able to explain the time varying flux of particles inside the spectrometer resulting to a distinct detector signal. Overall, the chapter tries to ground the observed phenomena to known physical concepts, contributing to a more comprehensive understanding of the system.

Finally, Chapter 8 serves as a culmination of the research findings presented throughout the dissertation. It summarizes the key outcomes and discoveries and presents recommendations for future research directions, highlighting potential areas of exploration and further investigation.

Chapter 2

FUNDAMENTAL THEORY AND PRINCIPLES

This chapter discusses the fundamental theories and supporting literature regarding the topics discussed in this dissertation. An introduction to plasma science, specifically atmospheric pressure plasmas, is first presented. Here we describe the fundamentals of plasma as a state of matter, and how variations in pressures directly affect the characteristics of the plasma. Methods of plasma generation are also described here with a more detailed discussion on radio frequency plasma excitation.

The next section discusses diagnostic methods used to characterize atmospheric pressure plasmas. At the atomic level, plasma can be described in terms of the excitation and de-excitation of charged species which can be quantified using optical emission spectroscopy (OES). In contrast, the bulk properties of plasma such as energy and density of charged species are typically obtained using probe analysis such as double probe measurements.

The last section in this chapter deals with the theory of ion mobility spectrometry. The basic theory of separation, drift acceleration, and detection of charged species in a drift tube ion mobility spectromeer are presented here. Other methods and devices used to quantify of ion mobilities are also presented in this section.

2.1 Introduction to Atmospheric Pressure Plasma Systems

Plasma is generally termed as the fourth state of matter. As energy is introduced to matter, the atoms that constitute the material get energized enough to overcome the intermolecular forces in between the atoms allowing them to move more freely. Further increasing the energy results to electrons escaping the atomic force of the nuclei causing the creation of a swarm of ions, electrons, and neutrals. This collection of particles is called plasma and is typically characterized by a quasi-neutral charge and a collective behavior. Plasma can be observed naturally in the stars and in the auroras up north, but are typically produced in laboratory or industry settings where a constant energy source, typically electrical, is used to ignite, and sustain the discharge of plasma. [2].

The universe is approximately made up of over 99.9 % of plasma [3]. And like majority of the universe, that 99 % of plasma exists in a vacuum. We however, do not exist in a vacuum but at ambient pressures and temperatures where plasma barely exists naturally. Plasmas that are created under these conditions are generally referred to as atmospheric pressure (AP) plasmas [4].

AP plasma has the primary advantage of the lack of need for vacuum systems making them easily accessible, and cheaper to produce. This allows the plasma to be applied towards materials that don't thrive in a vacuum environment such as organic materials and liquids. Characteristic of AP plasma is the presence of atmospheric gases such as Oxygen and Nitrogen in the swarm. [6–9].

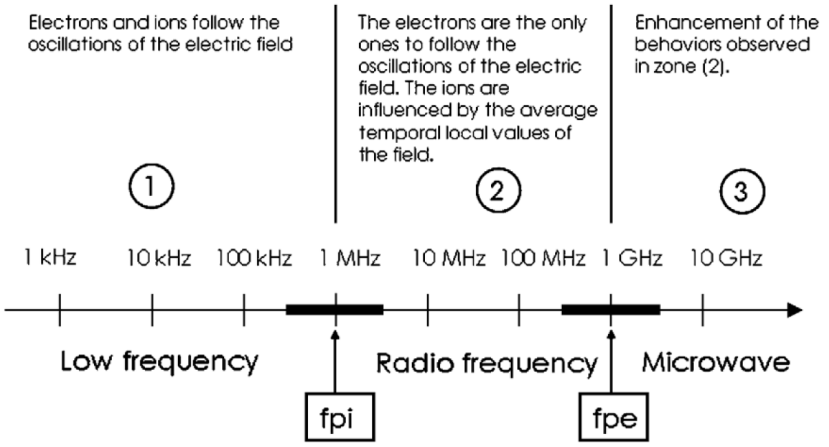

FIGURE 2.1: Description on the frequency dependent behavior of the charged species in plasma at increasing input voltage frequencies. Figures were obtained from the publication of C Tendero, et. al. [5].

$$n = \frac{P}{k_B T} \tag{2.1}$$

$$\ell = \frac{k_B T}{\Omega P \sqrt{2}} \tag{2.2}$$

When compared to the typical case of vacuum plasmas, as the pressure is increased from high vacuum, the mean free path of particles, ℓ, or the average distance before a collision occurs, decreases due to the increased density of gas particles, n, where P is the pressure in [Pa], k_B is the Boltzmann constant, and T is the absolute temperature in [K]. Under atmospheric conditions, this mean free path is less than Debye length, λ_D, or the length at which electrostatic forces may affect the plasma. Here Ω refers to the collision cross-section of the particles. The decreased mean free path observed as pressure increases results to the behavior of AP plasma being dominated more by collisions and diffusive effects when compared to their vacuum counterparts.

Pressure [Pa]	Neutral Density [cm^{-3}]	Mean Free Path
10^{-5} - 10^{-2}	10^{9} - 10^{13}	1 km- 10 cm
10^{-2} - 10^{0}	10^{13} - 10^{16}	10 cm- 0.1 mm
10^{0} - 10^{5}	10^{16} - 10^{19}	0.1 mm- 0.1 μm
101325 (1 atm)	2.7 x 10^{19}	64 nm

TABLE 2.1: Dependence of the mean free path of air on pressure and neutral gas density.

Plasma can be classified according to the driving frequency of the applied electric potential to discharge and sustain the plasma (Fig. 2.1). Up to a frequency of 1 MHz, plasma can be classified as a low-frequency or DC discharges. In this range, electrons and ions follow the oscillation of the electric field. AP sources such as dielectric barrier discharges, plasma jets, corona discharges, and gliding arc discharges fall within this range of operations.

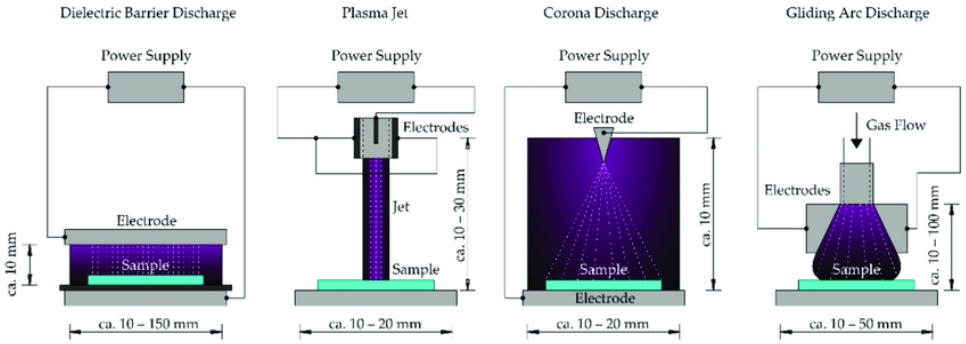

FIGURE 2.2: Schematic diagram of low frequency plasma discharge systems [10].

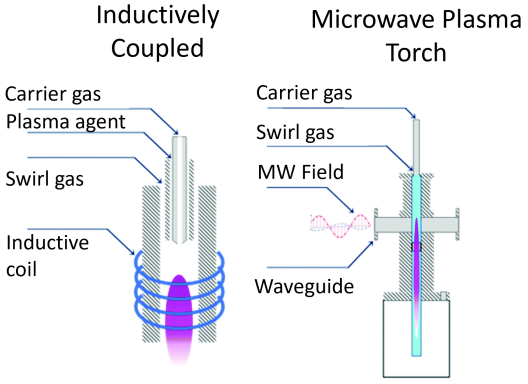

FIGURE 2.3: Schematic diagram of high frequency plasma discharge systems [11].

High frequency AP sources are those that function above the 1 MHz threshold. At f = 1 MHz-1 GHz, the plasma can be classified as an radio frequency (RF) discharge. At this frequency only electrons area able to move in accordance with the applied electric field resulting to ion motion being dominated by the localized field as a result of the highly mobile electron behavior. At $f > 1$ GHz, the discharge can be classified as a microwave discharge. In these types of plasmas, the localized field effects typical for RF sources are greatly increased. In some cases where $f >> 1$ GHz, electrons would also fail to move in accordance to the applied field resulting to the plasma being opaque to the field such that the field cannot propagate through the plasma but are rather attenuated rapidly. As the driving frequency of the plasma increases so does its properties such as its temperature and density. Plasma sources such as inductively coupled plasma and microwave plasma torches fall into these frequency ranges. [5, 12].

2.1.1 Radiofrequency AP Systems

Radiofrequency (RF) sources are plasma sources that are operated at an applied potential frequency of f = 1-100 MHz. Typically RF sources operate at an applied frequency of 13.56 MHz such that the skin depth (the depth at which the electromagnetic field penetrates the plasma) is relatively shallow, allowing efficient energy transfer to the plasma [13]. Depending on the excitation mode, RF sources could be categorized into two categories: capacitively coupled plasma (CCP), and inductively coupled plasma (ICP) sources.

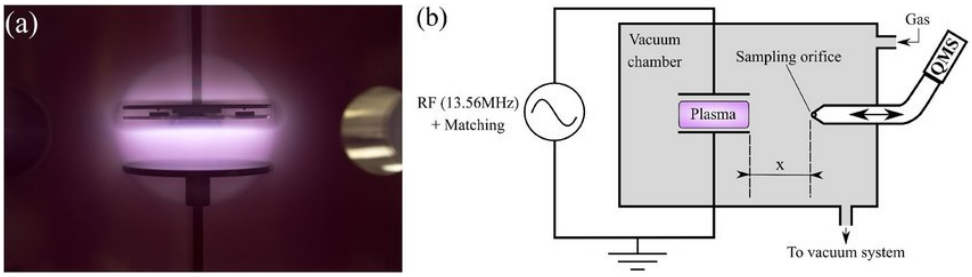

FIGURE 2.4: (a) Picture of a typical capacitvely coupled plasma source. (b) Corresponding schematic diagram of the CCP source coupled to a mass spectrometer. [15].

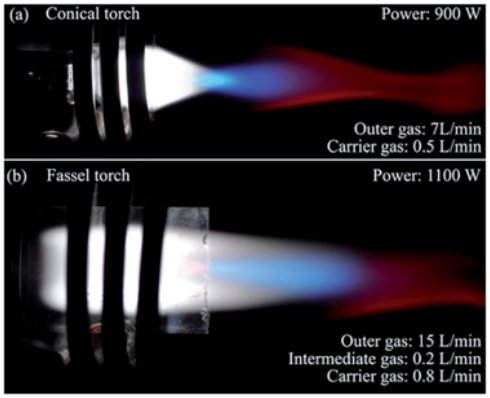

FIGURE 2.5: Images of inductively coupled plasma produced in the varied torch configurations.[16]

CCP devices utilize the electric field produced by the RF electrode with respect ground to realize the electrical breakdown of the gas. The simplest case of a CCP source is when the a RF electrode is positioned a few millimeters away from a ground electrode (Fig. 2.4). The electric field produced in between the electrodes result in the formation of plasma. Due to the simplicity of the electrode configuration, the plasma source may be easily scaled to industrial levels. The CCP source is typically characterized by high energy particles where typically further increasing the power goes into accelerating the charged species rather than the generation of new charged species. [14].

In contrast, ICP devices utilize the magnetic field produced by the alternating RF potential applied to an inductor to ionize the gas (Fig. 2.5). At low powers, the consecutive coils of the inductor acts as a capacitive source where the oscillations of charge species follow the local electric fields in between the coils. This phenomenon is referred to as the E mode. As the power in the inductor is increased, the magnitude of the magnetic field increases resulting to confinement of plasma in between the coils resulting to higher densities in these areas. This phenomenon is referred to as the H mode. The transition from E to H mode is characteristic of ICP sources. Since the magnetic field here is at the strongest at the center of the inductor, this reduces the contact of the plasma with the electrodes or walls of the system which allows the use of reactive gas species without deteriorating the system itself [5].

While both are effective methods of plasma production they both are dependent on the input power and density of the precursor gas. Typically however, ICP sources report higher densities due to the magnetic field confinement while CCP sources produce higher energy particles since due to increased electron acceleration by the applied electric field.

2.2 Atmospheric Pressure Plasma Diagnostics Methods

Like all states of matter, plasma has properties inherent to the state as well. At the atomic level, plasma may be described in terms of the continuous ionization and recombination of ions and neutrals while the bulk properties of the material describe the energies and densities of the ionized discharge. In particular, the bulk characteristics of plasma include but are not limited to the electron, and ion temperatures (T_e, and T_i), and densities (n_e, and n_i), the plasma Debye length (λ_D) and mean free path (ℓ), and the space potential of the plasma (V_p) . To quantify these characteristic diagnostic methods such as optical emission spectroscopy, and probe analysis are typically employed.

2.2.1 Optical Emission Spectroscopy

Optical emission spectroscopy or OES is an analysis method used to quantify the ionization and recombination of atomic species present in plasma [17]. When energy is introduced to a particle, electrons are able to move to a higher energy level. After some time, the electron loses the energy and moves to a lower energy level. This loss of energy translates to the emission of a photon with a quantized energy equal to the difference in the energy of the higher and lower energy levels. The photons emitted by the plasma may be collected and detected using OES to obtain a spectra showing the intensity and wavelengths of the emitted photons. The spectra may then be used to identify the atoms and their corresponding excited states present in the plasma.

$$\frac{n_{i+1}n_e}{n_i} = \frac{(2\pi m_e k_B T)^{3/2}}{h^2}\frac{2g_{i+1}}{g_i}e^{-\chi/k_B T} \tag{2.3}$$

For gas that is in local thermal equilibrium (LTE), the density of particles in a given energy state may be determined from the Saha ionization equation (Eq. 2.3). Given the density of ions (n_i), and the degeneracy of states in the i-th state (g_i), the energy required to move up an energy state, referred to as the ionization energy (χ), electron density (n_e), and gas temperature (T), the number density of ions in the i+1 state (n_{i+1}) may be determined. Typically for AP plasmas however, the LTE condition is not achieved due various reasons such as temperature variations and a non-Maxwellian electron energy distributions. This equation however may still be used to approximate the energy of a gas composed of a predominantly single atomic species.

2.2.2 Probe Diagnostic Methods

To obtain the bulk characteristics of plasma such as the electron temperature and densities, the use of a Langmuir probe is typically employed [18]. The theory for Langmuir probes has long been established and primarily assumes a non-collisional plasma- that is the Debye

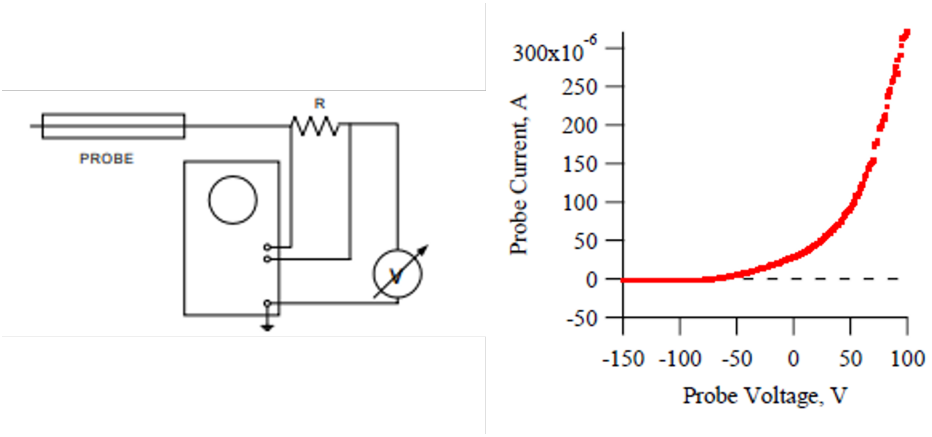

FIGURE 2.6: Schematic diagram of a single Langmuir probe [19] and the corresponding current-voltage trace when coupled to an atmospheric pressure plasmas source [20].

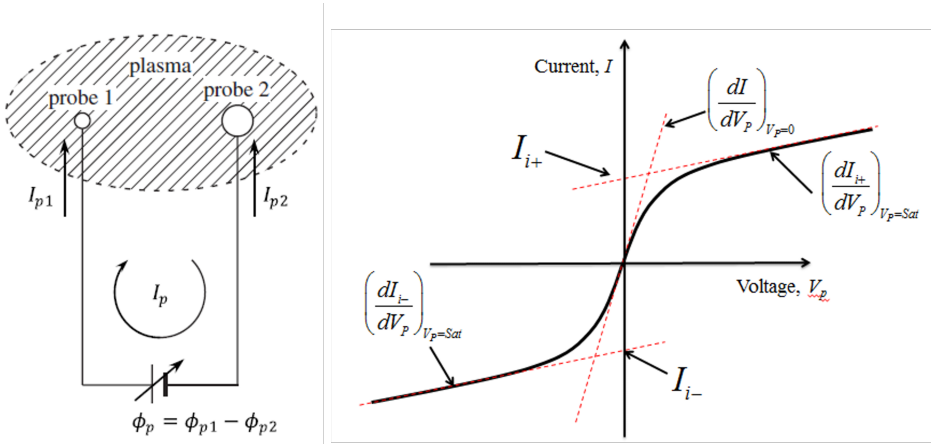

FIGURE 2.7: Schematic diagram of a double probe system [21] and the corresponding typical current-voltage characteristics [22].

length is smaller or comparable to the mean free path such that the electronic interactions between the probe dominate more than the collisional behavior. When a biased probe however is introduced to collisional plasmas such as AP plasma, the result is a current-voltage trace with no distinct electron saturation behavior. The trace similarly overestimates the electron temperature assuming the typical theory for Langmuir probes. This is not to say that Langmuir probes can not be applied to AP plasma. It is needed however in these cases to account for the collisional effects of the plasma with the probe surface.

To overcome the over-estimation of electron temperatures in single Langmuir probes, Double probe methods may be utilized. Double probes have the advantage of being able to measure bulk plasma parameters in collisional plasmas, and in plasmas that have a varying space potential. The theory for double probes assumes a closed loop between two identical probe electrodes and the plasma such that the current at the first probe is measured relative to the potential of the second probe. The result is a symmetric trace about the origin where the electron temperature, and ion densities may be calculated from [21]. This symmetric trace however is

only possible when the measurement system is completely isolated from the plasma source.

A typical double probe trace is shown in Fig. 2.7. The current-voltage trace exhibits three regions- the negative ion saturation region (I_{i-}), the transition region (dI_p/dV_p), and the positive ion saturation region (I_{i+}). Double probes typically realize these saturation regions at much lower applied voltages when compared to the single probe counterparts. The electron temperature and ion density can be calculated from these values using the following equations:

$$T_e(eV) = (I_{iS}/6.16)/(dI_p/dV_p)_{I_p=0} \tag{2.4}$$

$$n_i(m^{-3}) \sim (\frac{I_{iS}R_{p1}\sqrt{m_i\pi}}{A_1 e^{3/2}\lambda_i}) \cdot \frac{g(\tau)}{2\sqrt{\frac{\kappa T_e}{e}}} \tag{2.5}$$

Where, R_{p1} is the probe radius, m_i is the mass of the ion, A_i is the probe surface area, and λ_i is the ion mean free path. The term $(g(\tau)/2\sqrt{\kappa T_e/e})$ is a normalization factor determined from the the electron and ion temperatures of the system. This value is determined from the ratio of the negative and positive ion saturation regions.

2.3 Ion Mobility Spectrometry

Ion mobility spectrometry or IMS is a method used to analyze the ion species present in a given swarm under ambient pressures. The process has found its applications ranging from the detection of explosives and drugs, to air and food quality analysis, up to the analysis of large biomolecules. The process is an electrophoretic method designed to separate ions in a swarm based on their size and charges [23–27].

$$v_d = KE = d/t_a \tag{2.6}$$

$$K = \frac{3q}{8N}(\frac{\pi}{2\mu k_b T_{eff}})^{\frac{1}{2}} \frac{1+\alpha}{\Omega^{(1,1)}(T_{eff})} \tag{2.7}$$

The basis of IMS lies in the analysis of a particle's inherent mobilities, K [cm^2/Vs]. As a particle moves through an inert gas field with a constant electric field, E, they exhibit a drift velocity, v_d, proportional to the applied electric field and their inherent mobility (Eq. 2.6. The mobility (Eq. 2.7) is a generalized term that considers a particle's charge (q), reduced mass (μ), and the density of the gas it moves in (N), the correction factor (α), as well as the collision integral ($\Omega^{(1,1)}(T_{eff})$) which depends on the effective temperature of the system in the center-of-mass frame (T_{eff}). The drift velocity is similarly related to the ratio of drift length of the spectrometer (d) to the time of arrival of the ions at the detector (t_a). [1, 28].

A comparison of the typical IMS systems available in the market are presented in Fig. 2.8. IMS technologies have expanded widely and have varied depending on the applied potentials and geometric configurations of the spectrometer. IMS methods such as Travelling wave IMS

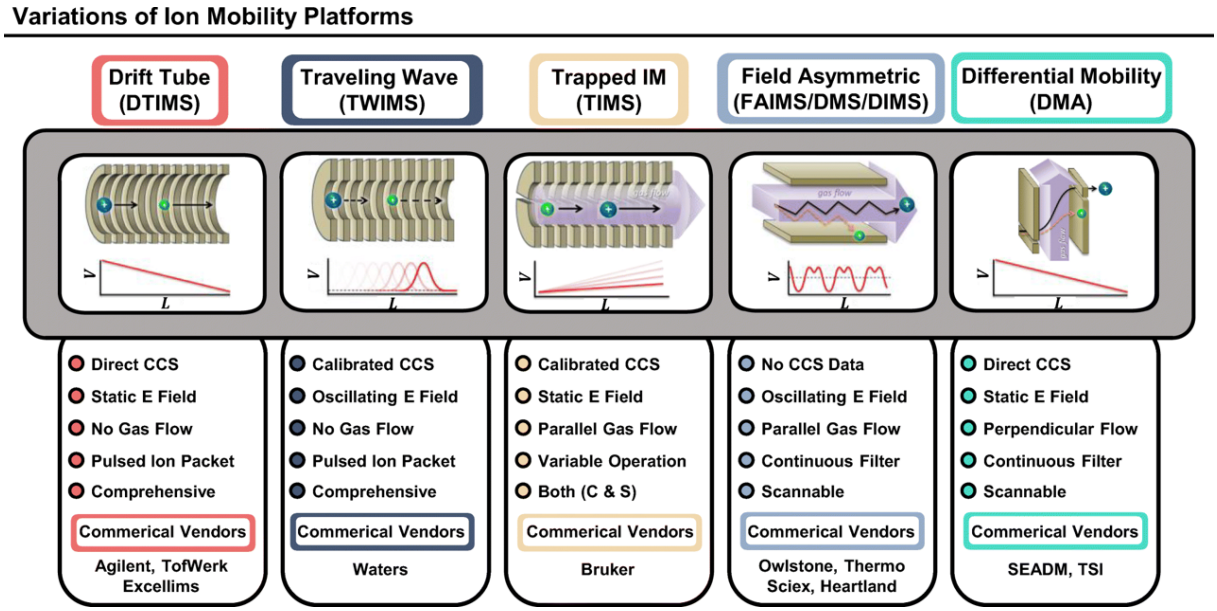

FIGURE 2.8: Variation of available IMS techonologies with their describe applied fields, gas dynamics, and main instrument manufacturers. Figures were obtained from the publication of JN Dodds, and ES Baker [34]

(TWIMS), Trapped IMS (TIMS), and Field Asymmetric IMS (FAIMS) are some of the more recent methods of performing IMS. The classical method of IMS is the use of a drift tube IMS (DTIMS) [29–33].

A typical design of the DTIMS and the corresponding spectra can be seen in Fig. 2.9. This IMS device consists of three major elements to achieve ion species analysis- the separation region, the drift region, and the detection region. Prior to entering the spectrometer, ions are first produced from the analyte using a radioactive substance such as Americium. The produced ions then travel into the separation region where variations in the applied potential between two wire grids allow the passage of a singular charge type of ions to pass through. This region consists of an ion gate to trigger the entrance of ions into the spectrometer. The typical gates mechanism approach are the Bradbury-Nielsen gate (BNG), and the Tyndall gate (TG) methods [35, 36]. Both mechanisms allow the passage of a singular ion type to pass through the gate depending on the produced electric field in between the two wire gates.

After the separation region, ions are accelerated through the drift region by a uniform electric field. Typically the electric in this region in the range of 5-10 kV/cm up to even 100 kV/cm [37]. This high electric field requirement and controlled carrier gas flow makes the design and operation of the DTIMS complicated. As the ions move through the drift region, accelerated by the applied electric field, collisions with the background gas separate the ions into discrete ion packets. The ions are then collected at the detector where a spectra showing the drift time of ions may be obtained. This drift time is related to the drift velocity of the ions where the mobilities may be calculated from.

The theory for ion mobility spectrometry may similarly be expanded towards the measurement of negatively charged species such as electrons. Due to the highly mobile nature

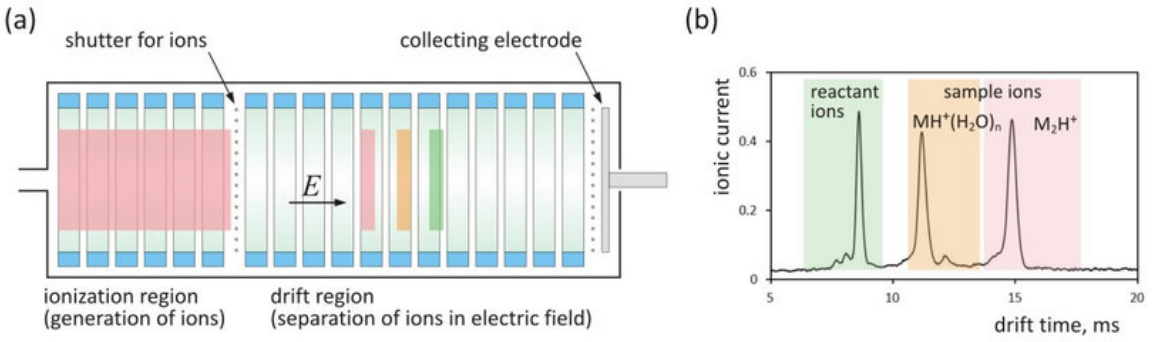

FIGURE 2.9: (a) Schematic diagram of a typical drift tube ion mobility spectrometer (DTIMS) design. (b) Corresponding time spectrum of ions present in the swarm. Figures were obtained from the publication of M. Wisnik, et. al.[38]

of electrons, the mobilities are measured in a positive electric field. Typically, mobilities are measured against the reduced electric field E/N in Townsends [Td] where N is the density of the background gas. For air at atmospheric conditions, this value approximately equal to the Loschmidt Constant (N = 2.686 x 10^{25} m^{-3}). Similarly, the electron mobility μ is expressed in terms of the product of the mobility and N.

Chapter 3

Development of an Atmospheric Pressure Plasma Source

This section of the study is dedicated to the development of an atmospheric pressure (AP) plasma system for ambient ion mobility spectrometry. The chapter first introduces the background of atmospheric pressure plasma- what it is, how it's made, and how to characterize it. Two configurations of the plasma source driven by an RF power source considered in this study are introduced- the inductively coupled plasma (ICP) source, and the capacitively coupled plasma (CCP) source. Based on the analysis results from the OES and double probe analysis, we determine the difference in the produced plasma characteristics between the two sources.

3.1 Inductively Coupled Plasma (ICP) System

The design of the inductively coupled plasma system is based on the research of Soriano [39]. The 8 cm diameter, 6.2 cm long ICP device consists of a 13.56 MHz RF power source connected in series to an inductor and a fabricated capacitor. The 24 mm long inductor consists of a single copper wire of 1.5 mm diameter coiled 12 times around a 5.8 cm long, 7 mm outer diameter, 5.6 mm inner diameter synthetic quartz glass tube where the precursor gas flows. At 3 MHz, the inductor has an inductance of 1.35 μF. The device is mounted onto an acrylic sheet connected to a series of steel L-bars to fix the system in place.

Two configurations of the ICP source were developed depending on the capacitor construction- a double plate type capacitor, and a cylindrical type capacitor (Fig. 3.1). The double plate capacitor construction consists of a metal electrode insulated with a pair of 1 mm thick alumina disks from the ground terminals. Both the base plate of the Faraday shield and the metal electrode fixed to the base plate serve as the ground terminals of the end capacitor. The cylindrical type capacitor consists of a 20 mm long cylindrical electrode insulated by 2.5 mm thick alumina disks from the grounded terminal located at the center of the electrode. At 3 MHz, the double plate capacitor, and the cylindrical type capacitor exhibits a capacitance of 96 pF, and 270 pF respectively. To more effectively realize the breakdown of plasma in the system, the double plate capacitor ICP system utilizes an ignition wire at the center of the quartz glass tube.

Operation of the device starts by igniting the plasma at a forward power of 70 W and a typical reflected power of around 6 W by rapidly inserting a grounded needle tungsten wire into the glass tube. Once ignited, the plasma could be sustained down to a minimum input power of 35 W, and Ar gas flow rate of 0.5 L/min. Typical operating parameters are input powers of 40-70 W, and Ar gas flow rates of 2-5 L/min. Typical power reflection from the ICP sources in both configurations ranges from 5 to 8 % at an input powers of 40-70 W.

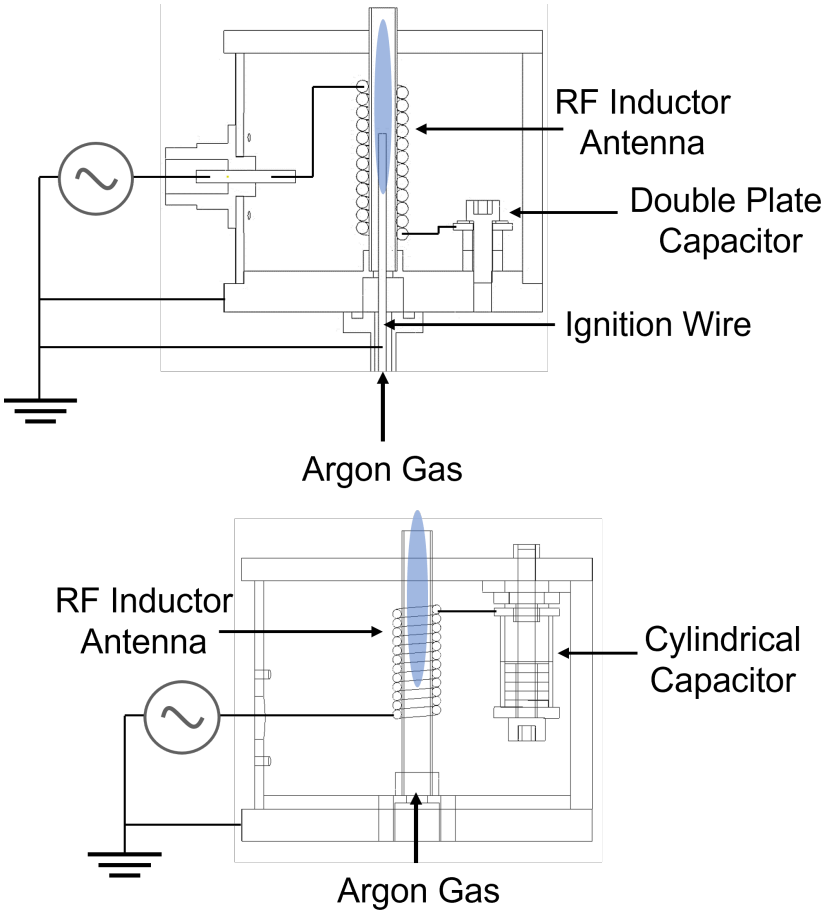

FIGURE 3.1: Schematic diagram of the ICP source with the (Up) double-plate capacitor, and (Down) cylindrical type capacitor.

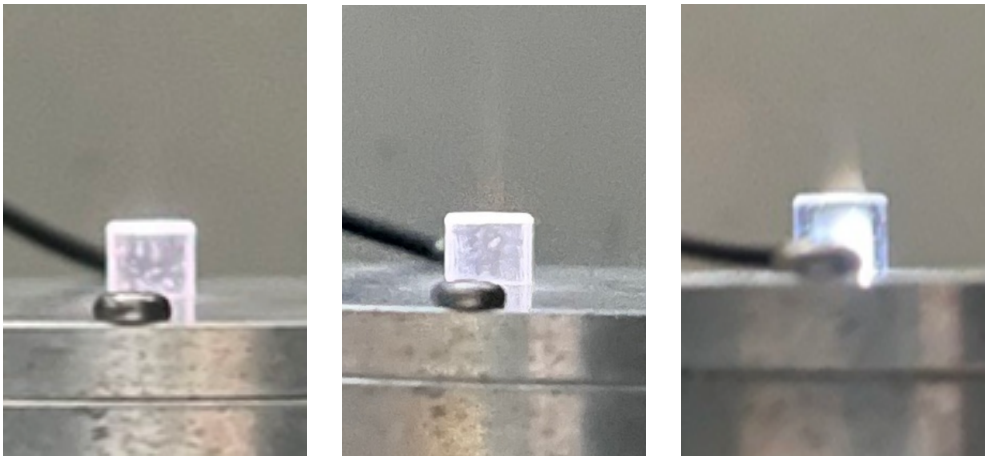

FIGURE 3.2: Images of the plasma plume from the ICP device with the (Left) double-plate capacitor, (Center) cylindrical capacitor, (Right) cylindrical capacitor and front-bias plate termination. The last image is the current configuration of the ICP device.

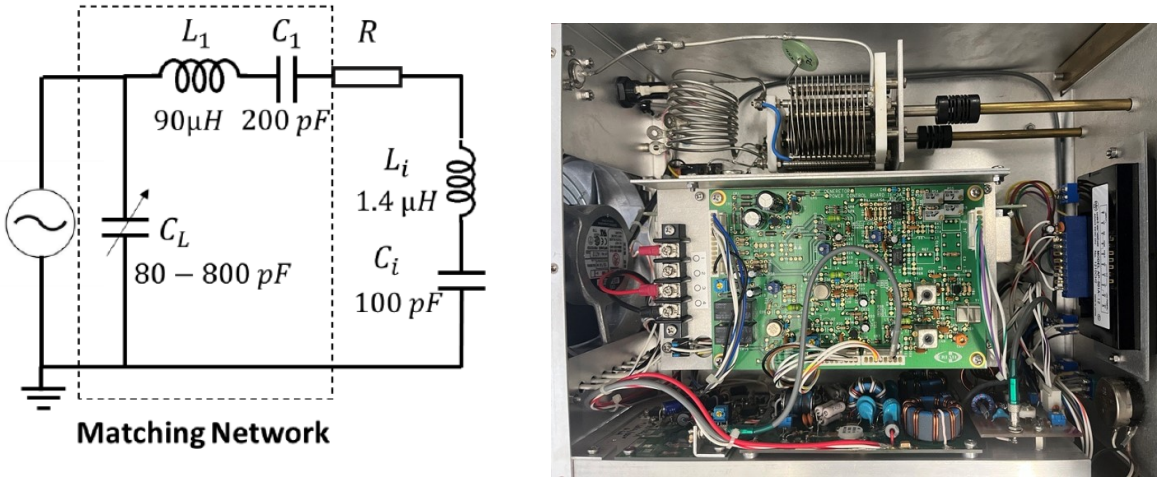

FIGURE 3.3: (Left) Schematic diagram of the matching network of the RF power source connected to the inductively coupled plasma. (Right) Actual image of the matching network [41].

3.1.1 Impedance Matching Network

An important concept when dealing with inductive components in RF powered devices is the impedance matching of the source with that of the plasma device. When dealing with alternating currents, a mismatch of impedances is often present between the source and the load caused by parasitic capacitances and inductances, transmission line effects, and distributed effects of the components [40]. This mismatch of impedances results to power losses in the form of reflected power to the source resulting to signal loss and reduced efficiency of the system. To mitigate this, an impedance matching network is typically employed.

Impedance matching networks are an intermediate network of capacitors and inductors placed in between the source and the load to compensate for the mismatch of impedances. The impedance matching network used for the plasma source discussed in this study is presented in Fig. 3.3. The system consists of an inductor and two variable capacitors, C_1, and C_L connected in parallel relative to each other. By tuning the capacitances of C_1, and C_L, reflected power can be minimized resulting to high current flow and high power absorption to the load.

The initial design of the ICP source using the double plate capacitor design, exhibited the lack of a plasma plume formation at the orifice which is indicative of the lack of ionized species in the area [17]. Modifications to the matching network of the RF power source (Fig. 3.4) and the ICP construction resulted to some insights on the design of the ICP source. Experiments with the variations in the matching network versions show that with the the removal of the matching network inductor (Version 2), and with the removal of the ICP capacitor (Version 3), plasma ignition was not achieved. Increasing the capacitance of the fabricated capacitor (Version 4) however led to the formation of some faint plume. This was indeed the case when the capacitor design was changed to the cylindrical type capacitor where the capacitance of the source is more than double than the previous ICP configuration.

Further improving on the ICP design, the position of the inductor was placed to be closer

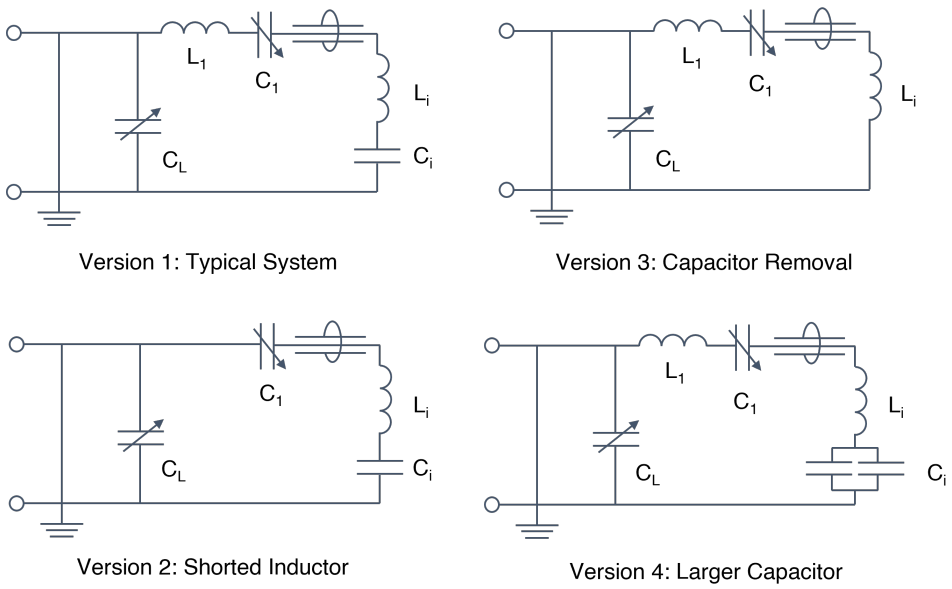

FIGURE 3.4: Matching network configurations tested to improve the ICP source configuration.

to the front-end plate of the device. This design resulted to a much visible plume formation at the orifice and is the current design of the ICP source.

3.2 Capacitively Coupled Plasma (CCP) System

The design of the capacitively coupled plasma source is based upon an earlier work by Lacdan [42]. The 5 cm diameter, 6.2 cm long CCP device consists of an Al RF electrode coupled to the RF power source. The top end of the RF electrode is positioned 1 mm from the inside edge of the grounded Faraday shield to realize the breakdown of the gas inside the quartz glass tube. The dimensions of the tube is similar to that of the ICP source. The device is fixed in a similar manner to the ICP source.

Operation of the device starts by igniting the plasma at a forward power of 45 W and a typical reflected power of around 3 W using a similar procedure with the tungsten wire and the ICP source. The plasma could be sustained down to a minimum input power of 20 W, and Ar gas flow rate of 0.5 L/min. Typical operating parameters are input powers of 30-55 W, and Ar gas flow rates of 2-5 L/min. Typical power reflection from the CCP source ranges from 6 to 9 % at an input powers of 30-55 W.

When compared to the ICP source, the CCP source does need additional components such as inductors or capacitors to realize plasma production allowing for the compact design of the system. This is likely since the built-in RF matching network is similar to the typical CCP matching network described by Godyak [43]. However, this results to the CCP source exhibiting thermal heating over prolonged usage especially at high input powers which may possibly result to thermal degradation of the system (Fig.3.6).

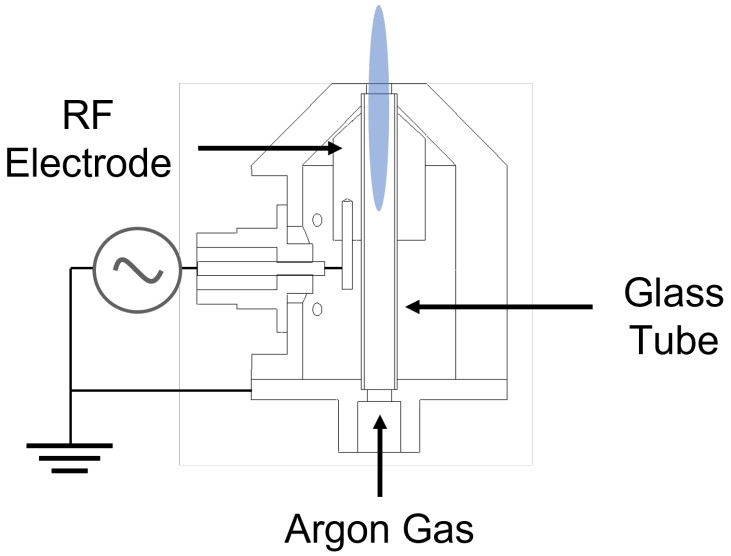

FIGURE 3.5: Schematic diagram of the CCP source.

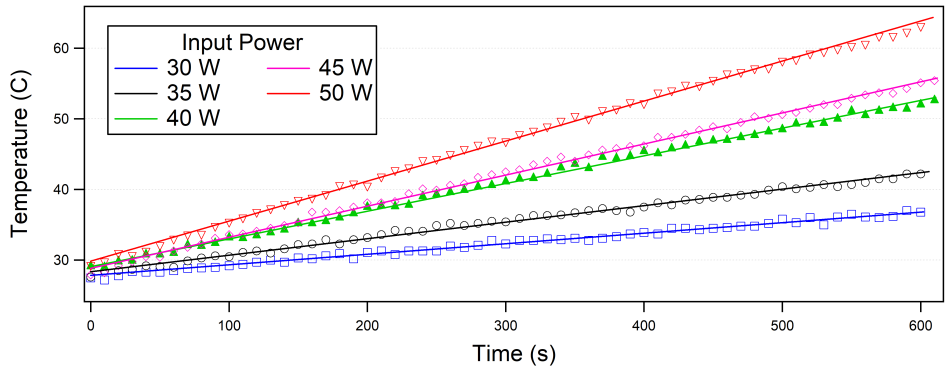

FIGURE 3.6: Surface temperature behavior over a period of 10 min at varying input powers of the CCP RF AP source.

3.3 Comparison of RF Atmospheric Pressure Plasma Sources

3.3.1 OES Analysis

Optical emission spectroscopy is performed by positioning the spectrometer along a line of sight of the plasma source. Optical methods such as beam focusing are also employed to ensure that the majority of the photons emitted by the source is collected at the detector.

Figure 3.7 shows the experimental configuration of the ICP source coupled to the spectrometer. A fiber optic cable attached to the spectrometer is positioned parallel to the direction of the plasma plume. In between the plasma source and the spectrometer, a plano-convex lens with a focal length of 15 cm is placed to focus the light from the source towards the fiber optic cable. The spectrometer, OceanOptics USB 4000 with a resolution of 0.19 nm, and an integration time of 40 ms, was utilized for measurement of the emission characteristics of the plasma. To ensure that the components are fixed along the same line of sight, the entire system is fixed

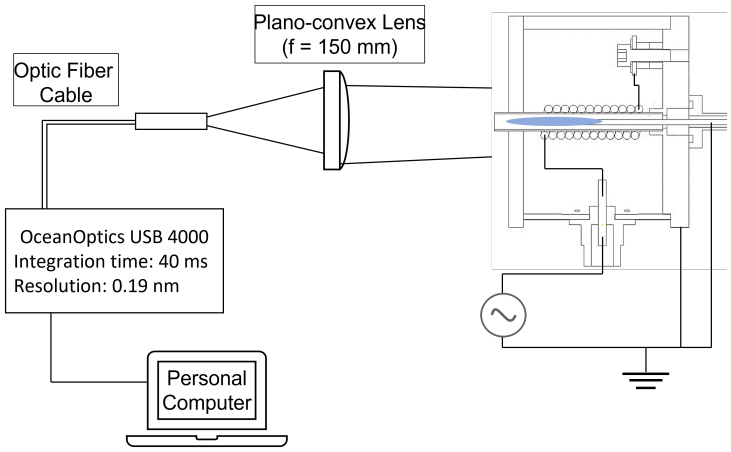

FIGURE 3.7: Schematic diagram of the ICP source coupled to the optical emission spectrometer.

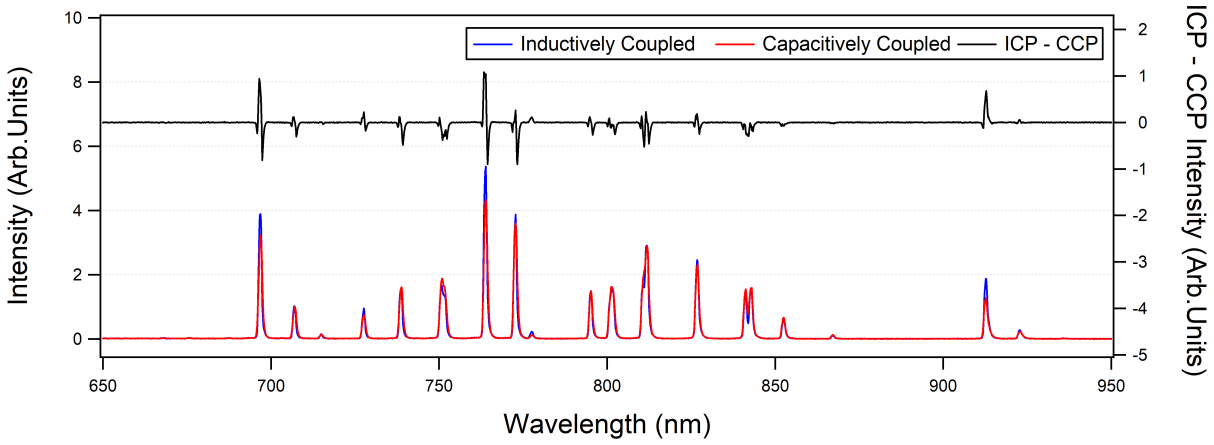

FIGURE 3.8: Optical emission spectra produced by the ICP and CCP sources with an input power of 40 W and an Argon gas flow rate of 2 L/min.

on an optical rail.

The typical spectra for the produced plasma used in this study are shown in Fig. 3.8. The spectra is measured from 345 to 1000 nm. The prominent peaks in the spectra are those attributed to the presence of Ar I while a single peak of O I is found at 777.2 nm [44].

Plasma was discharged from both sources at an input flow rate of 2 L/min and at varying input powers. Observed in the typical normalized traces of Argon plasma in Fig. 3.8 are peaks intensities that are greater in the ICP configuration when compared to the CCP source and vice-versa. When the plasma is operated at an input power of 35- 50 W, the ICP source exhibits higher intensities for the Ar I peaks: 696.5, 763.5, 772.3/772.4, and 912.3 nm, while the CCP source shows higher intensities for the Ar I peaks: 750.4/751.5, 800.6/800.5, 810.4/811.5, and 840.8/842.5 nm.

The peaks shown here share a common lower-energy level for each respective source with the ICP peaks sharing a lower-energy level of 11.55 eV for the 696.5, 763.5, 772.3, and 912.3

λ [nm]	Lower Energy [eV]	Upper Energy [eV]
696.5	11.55	13.33
763.5	11.55	13.17
772.3	11.55	13.15
772.4	11.72	13.32
912.3	11.55	12.91

TABLE 3.1: Lower and upper energy levels of more intense peaks from the optical emission spectra of the ICP produced plasma.

λ [nm]	Lower Energy [eV]	Upper Energy [eV]
750.4	11.83	13.48
751.5	11.62	13.27
800.6	11.62	13.17
801.5	11.55	13.09
810.4	11.62	13.15
811.5	11.55	13.08
840.8	11.83	13.30
842.5	11.62	13.09

TABLE 3.2: Lower and upper energy levels of more intense peaks from the optical emission spectra of the CCP produced plasma.

nm peaks, and the CCP source sharing lower energy levels of 11.55 eV for the 800.5, 811.5 nm peaks, 11.62 eV for the 751.5, 800.6, 810.4, 842.5 nm peaks, and 11.83 eV for the 750.4, 840.8 nm peaks. The presence of varying intensities in both sources may indicate a difference in the ionization mechanism of the two sources

Optical emission spectroscopy can also determine the relative degree of ionization of the species found in the plasma by observing the intensity ratios of varied peaks. The peak ratios of Ar I peaks: 800.6/801.5 nm (13.17/13.09 eV upper-level energy) and 738.4 nm (13.3 eV upper-level energy) nm indicate the ionization efficiency of Argon while the peak ratios of O I at 777.2 nm (10.74 eV upper-level energy) against Ar I at 738.4 nm show the ionization efficiency of Oxygen in the plasma.

Observing the intensity ratios (Fig. 3.9) of the 800.6 nm: 738.4 nm Argon peaks show that both systems observe a relative decreasing trend in the ratio with increasing powers which indicate a higher temperature plasma. On average here, the CCP source exhibits slightly higher rates of ionization of Argon. In the second plot, the ratio of O I at 777.2 nm against Ar I at 738.4 nm show a larger intensity of oxygen for the ICP source when compared to the CCP configuration at all input powers. This indicates the effectiveness of the ICP source when it comes to the ionization of oxygen species.

3.3.2 Double Probe Analysis

The circuit used for double probe measurements in this experiment is presented in Fig. 4.8. The double probe consists of two symmetrical tungsten electrodes with a diameter of 0.5 mm, and an exposed length of 3 mm. The probes are positioned 1 mm away from each other. The probe circuit is contained in an aluminum box and was mounted onto a movable holder

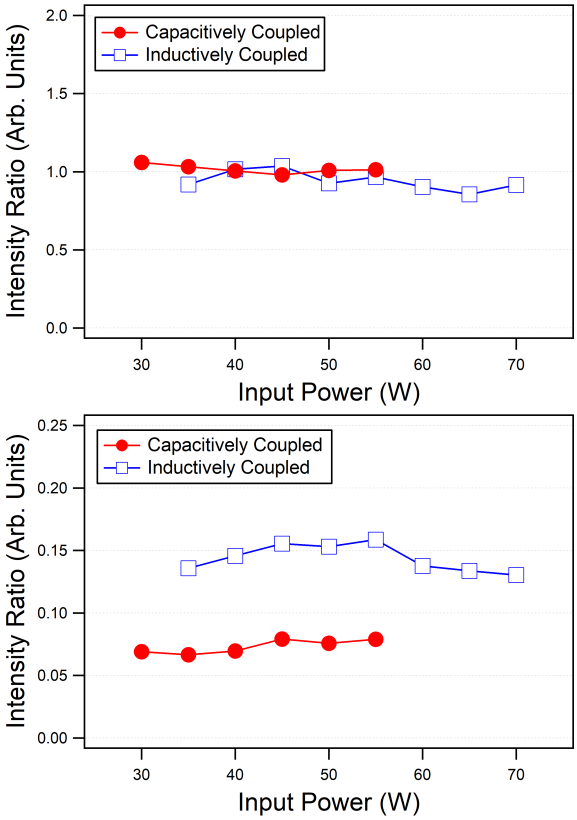

FIGURE 3.9: Intensity ratios of (Up) 800.6 nm: 738.4 nm Argon peaks, and (Down) 777.2 nm O I peak: 738.4 nm Argon peak. Data was normalized to the intensity of the 706.7 nm Ar I peak prior to calculation of intensity ratios.

attached to an optical rail for spatially resolved measurements. For both RF AP sources, the measurement origin was set to be at the front end of the Faraday shield. A voltage sweep of -7.5 V to 7.5 V was applied to one probe while the current was measured with reference to the second probe. The applied voltage and current measurements were done using a Keysight B2901 Source Measurement Unit which was terminated to the internal floating potential of the device. While typically a double probe show both saturation regions, it is not unusual to see that only one, or none of the saturation regions are present in the probe at low applied potentials due to increased plasma density in some regions of the plasma. As such for comparison purposes, the normalization constant is set to 1 in this study.

From the experimental results an asymmetric current-voltage profile was observed evident from a shift of the zero current potential from 0 V (Fig. 3.11). The observed asymmetry of the probe currents is often caused by variations in the effective probe area in contact with the plasma [20]. By changing the geometry of the double probe system, the probe may be shifted off the center origin. These shifts indicate an unequal immersion of the probe with the plasma source. Thus it is typical to assume that the value of $(dI_p/dV_p)_{I_p=0}$ is not the current derivative measured at I_p = 0, but is rather defined as the point at which the current derivative is maximized. Additionally, we define the zero current crossing potential as the floating potential, V_f, such that shifts from 0 V in this value indicate changes on the plasma homogeneity on the

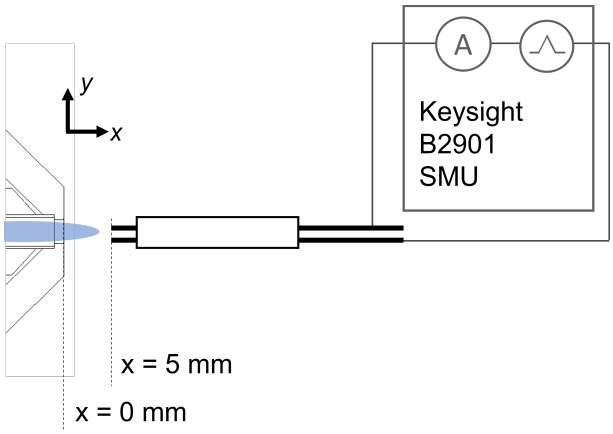

FIGURE 3.10: Schematic diagram of the double probe system coupled to the CCP source.

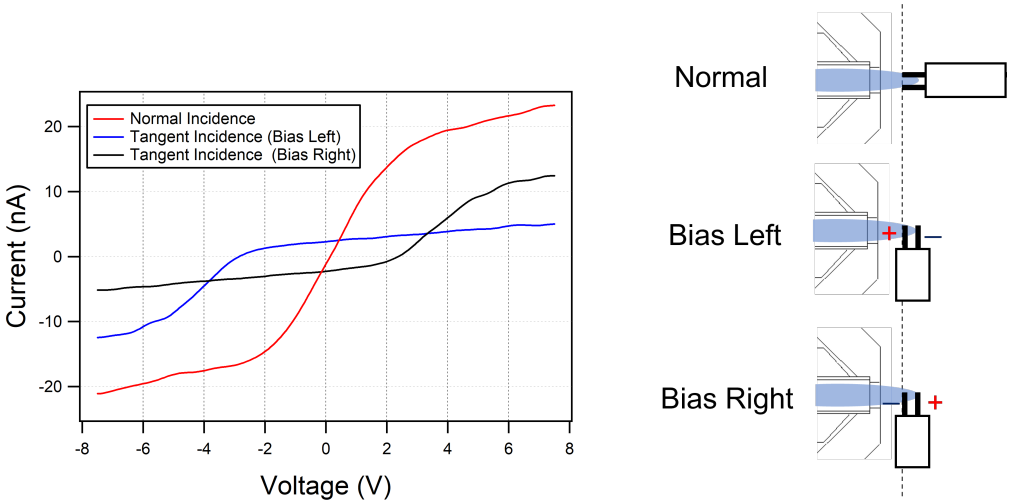

FIGURE 3.11: Exhibited asymmetry of the double probe system at varying probe geometries.

probe surfaces.

Plasma parameters of the RF AP sources are shown in Fig. 3.12, 3.13, 3.14. Typical operating conditions of the plasma sources are at an input power of 40 W, Ar gas flow rate of 5 L/min, and measured at 5 mm away from the ground base plate of the respective plasma system.

Increasing input powers show an increase in the observed temperature, density, and space potential of both sources. with the ICP source reporting a higher rate of change in parameters. The CCP source reports a higher ion density with varying input powers with the density being 1.8 times than that of the ICP source at 40 W, and 1.5 times at 50 W. In contrast, the ICP source reports an overall higher floating potential than the CCP source. Temperature increases significantly for the ICP source starting at 40 W reaching up to 1.2 eV at 50 W input power. This is typical in ICP sources where a change in the confinement mode of the plasma occurs at increasing input powers [45].

Variation in flow rates result to limited changes in the electron temperature and floating

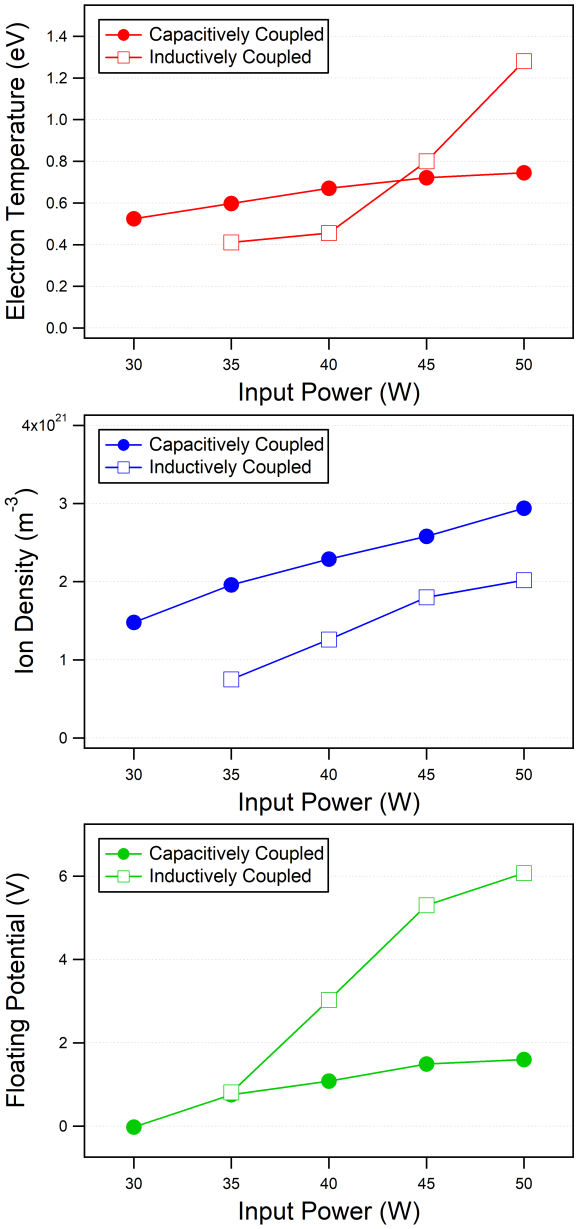

FIGURE 3.12: (Red) Electron temperature, (Blue) ion density, and (Green) floating potentials of the CCP and ICP sources at varying input powers

potential of the plasma with a reported average T_e and V_p values of 0.56 eV and 2.6 V for the ICP source, and 0.66 eV and 0.94 V for the CCP source. Ion density similarly increases with flow rates in both cases with the CCP source reporting what seems to be an exponential increase. Plasma homogeneity does not change for both sources when the gas flow rate is increased from 3-5 L/min.

As the probe moves away from the plasma source, an exponential decrease is observed in the ion densities in the plasma. A similar decreasing trend is observed for T_e and V_f. Normalizing the densities of the plasma at x = 5 mm, and applying an exponential fit to the trace allows us to identify the distance at which the density of ions are reduced by half relative to this position. This distance can be referred to as the survival distance of ions which is an important

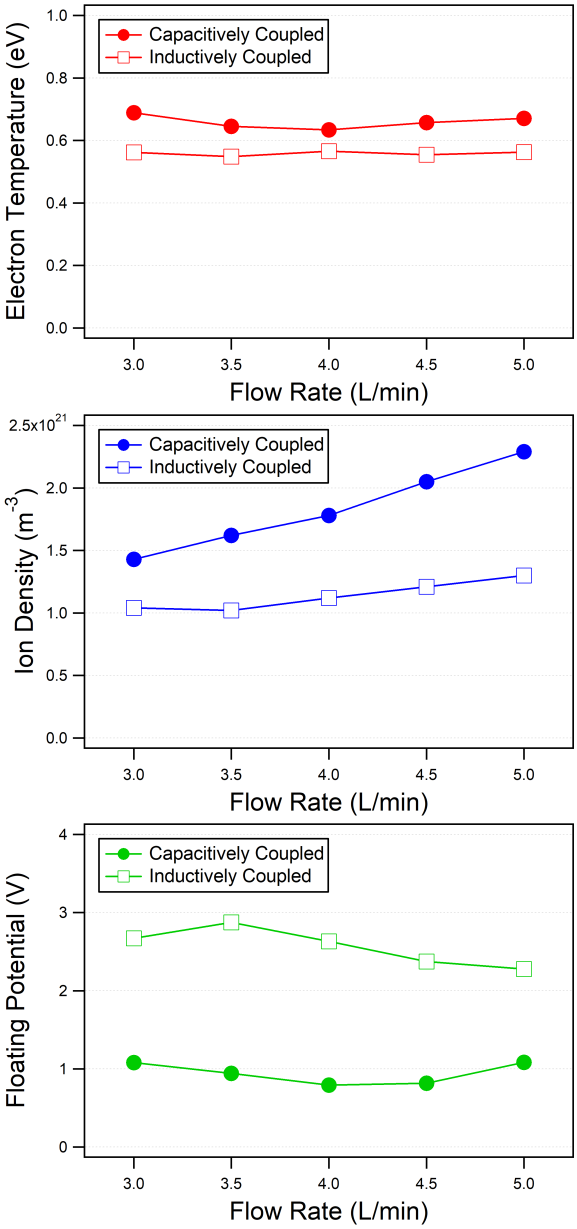

FIGURE 3.13: (Red) Electron temperature, (Blue) ion density, and (Green) floating potentials of the CCP and ICP sources at varying input gas flow rates

parameter to consider when designing the configuration of the spectrometer device. It is observed that this distance is at x = 7 mm for the CCP source, and x = 7.5 mm for the ICP source. While a longer survival distance is preferred for mobility spectrometry such that ion collection is maximized at the detector, the density of the CCP source is still greater by about 1.6 times when compared to the ICP source. At positions greater than x = 8 mm, the temperature and floating potential for both cases converge indicating a more dilute plasma at these regions.

Variations in the homogeneity described by the shifts in the floating potentials of the double probe trace may be attributed to the changes in the observed ion motions in the two sources. Due to the magnetic field present in the ICP source, ions and electrons gyrate around the direction of the induced magnetic field, while in the CCP source the ions and electrons follow the

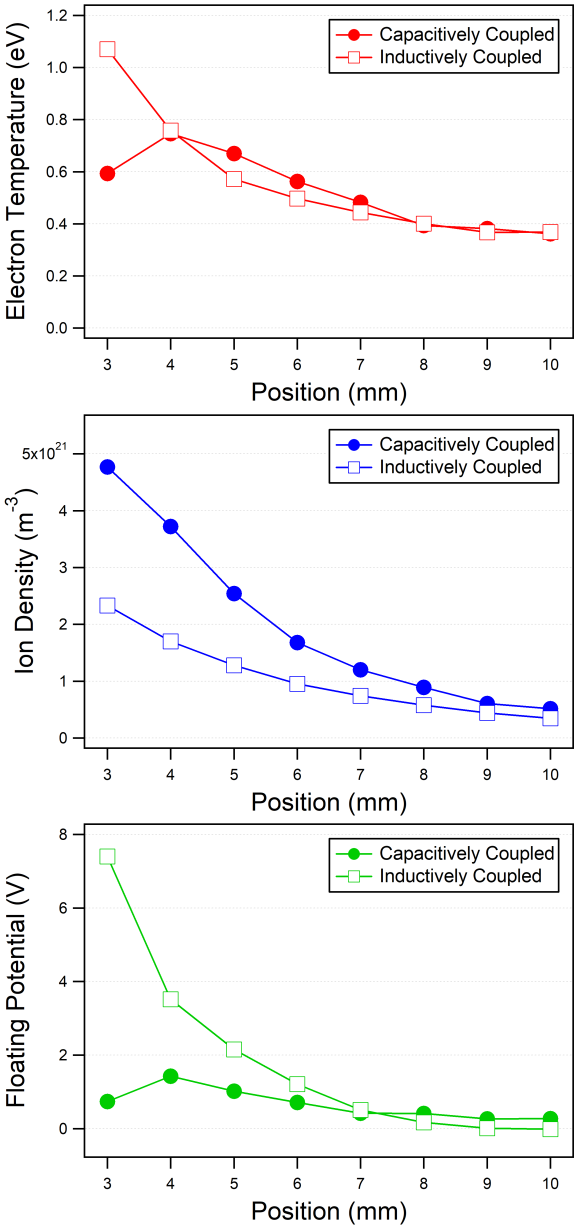

FIGURE 3.14: (Red) Electron temperature, (Blue) ion density, and (Green) floating potentials of the CCP and ICP sources at varying probe positions

direction of the applied electric field. For the ICP source the motion of charged species is in the plane perpendicular to the probe surface, while for the CCP source, the motion is along the direction of the plume, parallel to the probe surface.

3.4 Summary

Two configurations of RF AP sources, a capacitively coupled plasma (CCP) source, and an inductively coupled plasma (ICP) source, were developed and characterized for further applications towards ambient ion mobility spectrometry. Optical emission results show that a

distinct spectra is observed for both systems indicating a difference in the ionization mechanism in both sources. the ICP source prefers the ionization of lower energy level electrons particularly those at 11.55 eV as compared to a broader spread for the case of the CCP source at a lower energy level of 11.55, 11.62, and 11.83 eV. Analysis of the peak ratio of 777.2 nm O I peak: 738.4 nm Argon peak shows that the ICP configuration reports better ionization levels of oxygen species across varying input powers

Double probe measurements in the effluent or plume region of the plasma sources shows that in all cases, the CCP source exhibits a higher density than the ICP source by 70 %. Increasing power results to increasing electron temperature, ion density, and floating potential in both cases with the CCP exhibiting a higher temperature at $P < 40$ W, while the ICP exhibiting a higher temperature at $P > 45$ W. Changes in flow rates result to minimal changes in temperature, while a similar electron temperature and floating potential is observed at positions greater than 8 mm away from the ground plate of the plasma sources. Due to variations in the motion of ions and electrons in both sources, a more homogenous plasma is observed for the CCP source as opposed to the ICP source. The application of both systems for ion mobility spectrometry will be discussed in the next chapter within the context of the designed spectrometer.

Chapter 4

Development of the Ambient Mobility Spectrometer

This section describes the design, and operation modes of the ambient mobility spectrometer. The spectrometer is a compact device able to obtain a unique current signal at low electric field intensities where charge species mobilities may be calculated from. The first part of this chapter presents a background on ion mobility spectrometry and the typical methods it employs to obtain swarm parameters of charged species. Next we describe the design of the ambient mobility spectrometer and how the mesh addition results to an observed current asymmetry in the detector behavior. Finally, we try to explain the observed phenomena by analyzing the near mesh plasma parameters at varying mesh biases and sizes. Parts of these sections were discussed in a prior publication of the author [46].

4.1 Development of the Ambient Mobility Spectrometer

Figure 4.2 illustrates the compact design of the ambient mobility spectrometer. The RF AP sources described in the previous chapter serves as the ion/electron sources for the spectrometer. The aperture of the device is placed directly in front of the plasma source such that the Faraday shields of both devices are in contact. The 44 mm diameter, 53 mm long ambient mobility spectrometer consists of three main components- the bipolar gated shutter, the drift region, and the detector.

The bipolar gated shutter consists of an Al electrode positioned 6 mm away from the spectrometer aperture. A potential is applied to the shutter via a BNC terminal. A sheet of Ni wire mesh with mesh sizes of 30, 100, and 200 corresponding to wire diameters of 0.15, 0.1, and 0.05 mm and aperture sizes of 600, 150, and 75 μm is placed at the plasma facing side of the shutter. The presence of this mesh allows the detection of a phase-locked signal at the detector during the time a square wave voltage is applied to the shutter. A more detailed description of the area around the shutter region is described in Fig. 4.3.

The 10 mm diameter, 30 mm long drift region 10 Cu electrodes spaced 2 mm apart. The primary electrode is positioned 2 mm from the rear side of the shutter electrode is connected to a separate BNC terminal . The electrodes are separated by a 1MΩ resistor such that a voltage drop of 10 % is observed for each succeeding electrode. This produces a constant electric field at the center of the spectrometer with a magnitude $E = V_{Bias}/$ 3 cm, where V_{Bias} is the applied potential to the first bias electrode. The detector consists of a 10 mm diameter copper electrode positioned at the end of the drift tube region. The detector is connected to an isolation amplifier to amplify the detected signal before being observed using an oscilloscope.

Typical operation of the device utilizes a function generator (EZ Digital Co. Ltd. DGF-6003) coupled to an amplifier (Turtle Industries Co. Ltd T-HVA01) to drive the voltage of the

FIGURE 4.1: (Left) Image of the actual mobility spectrometer, and (Right) the spectrometer device without the outer ground chassis.

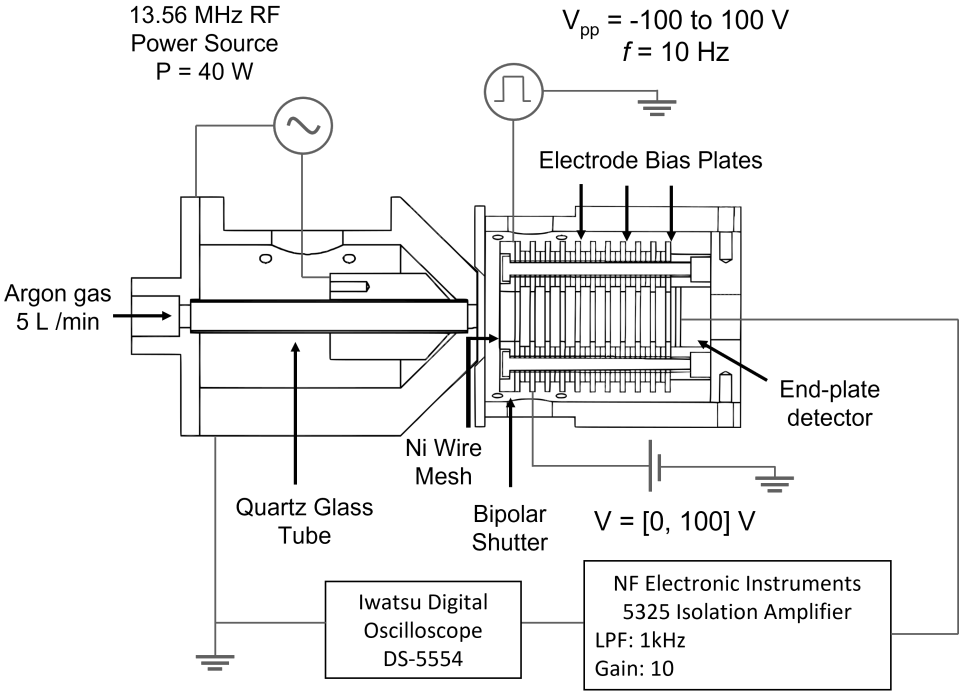

FIGURE 4.2: Schematic diagram of the RF AP CCP source coupled to the ambient mobiity spectrometer

shutter electrode with respect to the Faraday shield of the RF plasma source biased at ground potential. The shutter is driven by a square waveform with alternating polarity of $\pm$ 100 V at a frequency of 10 Hz. The primary bias plate is connected to a DC voltage source (TEXIO PSW-360H800) to apply a bias up to a magnitude of 100 V. Lastly the detector is connected to an isolation amplifier (NF Electronic Instruments 5325) with a low pass filter of 1 kHz and a gain of 10. The signal from the amplifier is detected at the oscilloscope (IWATSU DS-5554 Digital Oscilloscope) where the trace is recorded at an average of 32 samples at a sampling rate of 5 MS/s. The measurements taken with the IMS are at a pressure of 1 atm and an average room temperature of 300 K.

When applied to the mobility spectrometer in a positive electric field at the typical operating parameters of the RF AP plasma sources- an input power of 40 W, and a gas flow rate of 5

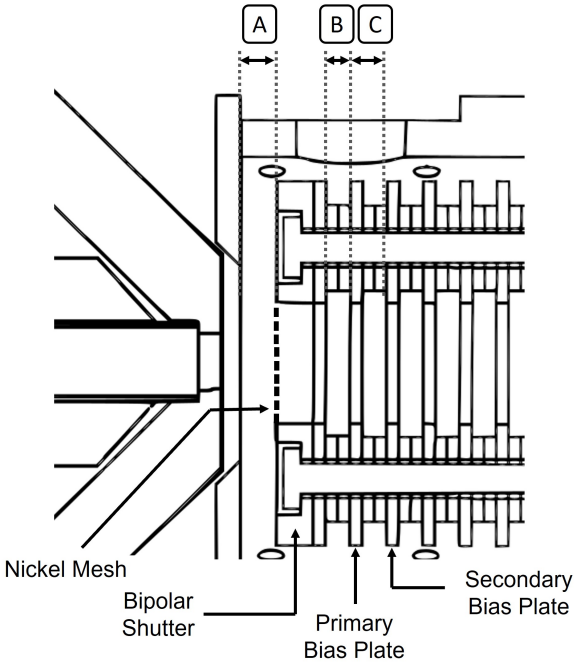

FIGURE 4.3: Schematic diagram of the shutter region of the spectrometer. The following regions correspond to a series of potential variations to realize charge transport to the detector: (A) d = 5 mm, V_i = 0 V, V_f = 100 V, (B) d = 2 mm, V_i = 100V, $V_f = V_{Bias}$, (C) d = 3 mm, $V_i = V_{Bias}$, V_f = 0.9 (V_{Bias}), where d is the length of the region, V_i is the initial potential, and V_f is the final potential.

L/min, the signal from the CCP source exhibits a distinct asymmetric profile while the ICP does not. This may be due to the confinement of charged species in the inductor resulting to a reduced density of ions in the effluent region. At input powers of 45-50 W, the ICP source exhibits arcing with the mesh making the ICP source incompatible with the IMS source for mobility spectrometry.

4.1.1 Mesh-Gated Shutter Signal

The initial iteration of the spectrometer configuration includes the use of a Cu 100 mesh size applied to the shutter (Fig. 4.5). Using this configuration, the detector current was taken at varying frequencies and shutter voltages in a zero electric field drift region to quantify the effects of the mesh addition. The plasma source used for this experiment is the CCP device operating at an input gas flow rate of 3 L/min at an input power of 40 W.

The observed signal at varying shutter frequencies are reported in Fig.4.6. The shutter was driven with a square wave voltage with $V_{Shutter}$ = [-50, 50] V at f = 1-100 Hz. We define two distinct regions of the signal- the negative and positive phases. The negative phase is the time region of the signal where the shutter is at a lower negative potential, while the positive phase is the time wherein the shutter is biased at a higher positive potential.

Normalizing the graphs to their respective periods, it can be observed that at all input frequencies, there exists an asymmetric behavior between the currents observed in the negative

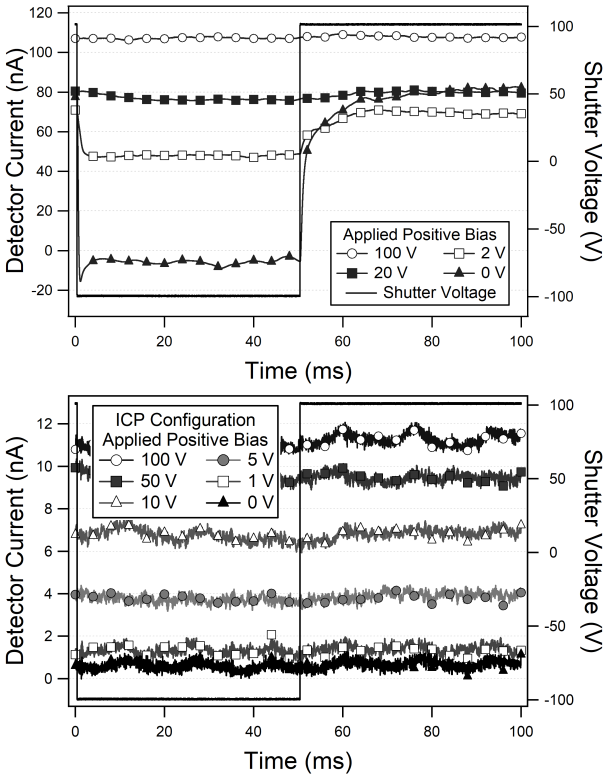

FIGURE 4.4: Detector currents observed when the (Top) CCP source, and the (Bottom) ICP source are coupled to the spectrometer. Operating parameters of both sources are at a gas flow rate of 5 L/min, and an input power of 40 W.

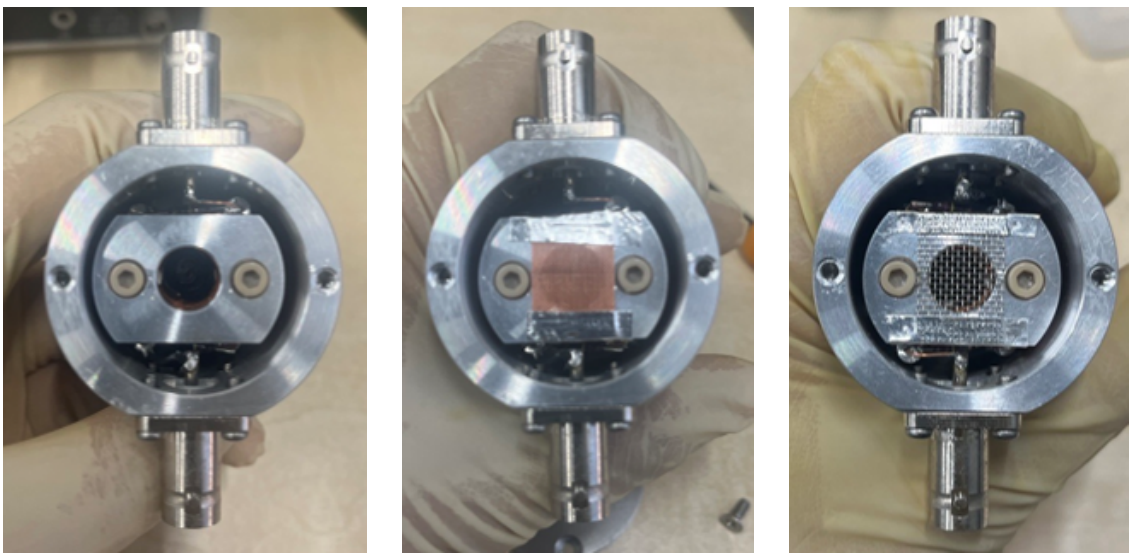

FIGURE 4.5: Images of the IMS shutter (Left) when no mesh is present (0 mesh), (Center) when a Cu 100 mesh is secured, and (Right) when a Ni 30 mesh is secured. The mesh is attached to shutter using conducting adhesive tape.

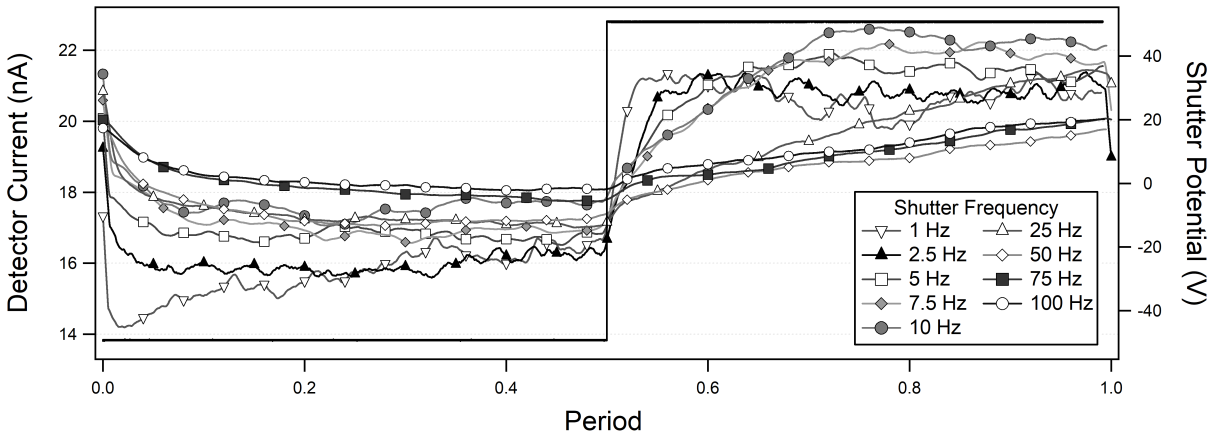

FIGURE 4.6: Effect of varying shutter frequencies on the observed detector current in a zero field drift region.

and positive phases. The negative phase currents become more positive with increasing frequencies, while the positive phase currents typically become more negative past 10 Hz. This results to a decrease in the asymmetry in the two phases as frequency is increased. The transition time, or the time it takes for the signal to saturate relative to the onset of the positive phase, is maximized for the case of 10 Hz frequency.

The signal when the applied shutter voltage in the negative, and positive phases respectively are varied are shown in Fig.4.7. To isolate the effects of the shutter potential, a constant lower or upper potential corresponding to the negative and positive phases were realized while varying the opposite phase potential.The applied voltage is driven at a frequency of 10 Hz.

During the time the upper potential is held constant at 100 V in the positive phase, a more negative lower shutter potential results to a more negative current observed during the negative phase of the signal. The currents in the positive phase similarly shifts downwards as well. The transition time in the negative phase increases with a more negative lower shutter potential negative phase, while the transition time in the positive phase seems to remain constant.

In contrast, during the time the lower potential in the negative phase is held constant at -100 V, a more positive shutter potential results to an increase in positive phase currents. In the negative phase, the current also increases with a more positive shutter potential.

A previous study with the CCP source applied to a Gerdien Condenser for analysis of ion mobilities reported a change in the observed signal depending on the detector material type [47]. They reported that the nickel electrode realizes higher ion density collection. Thus the change of mesh type material was realized. Experiments on the comparison of material types show however that the change from using a Cu mesh to that of Ni mesh resulted to a about 10 % change in the observed signal.

4.2 Near Mesh Plasma Behavior

Experimentally, the presence of a mesh-gated shutter results in an asymmetric behavior in the observed detector signal of the system. To better understand the phenomena, the local

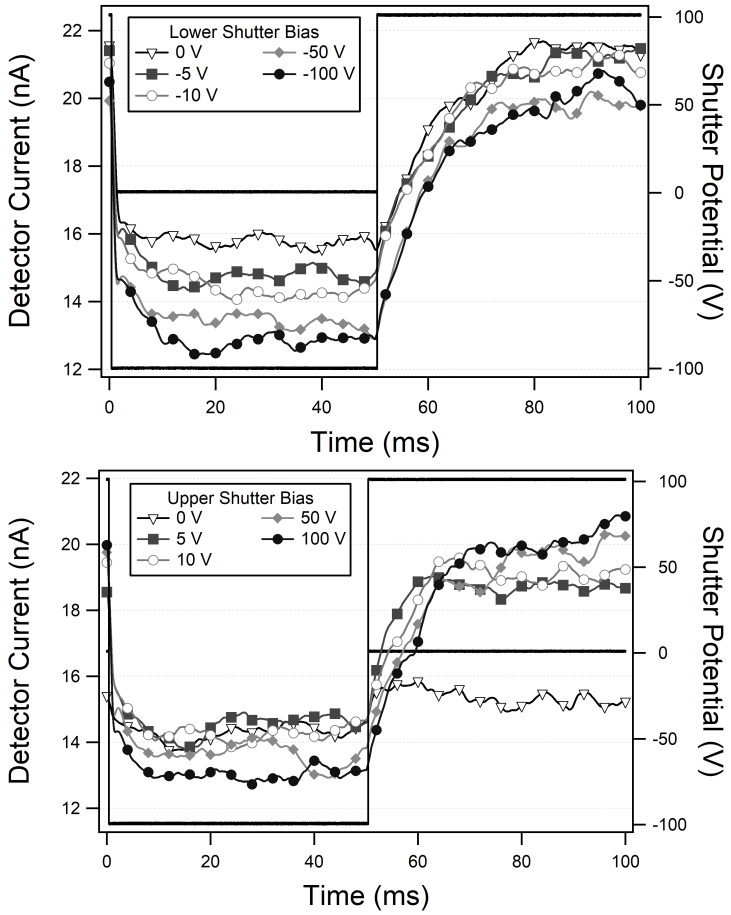

FIGURE 4.7: Effect of varying (Top) lower, and (Bottom) upper shutter potentials on the observed detector current in a zero field drift region.

plasma parameters during the time a biased mesh is in contact with the plasma source must be obtained. Due to the compact nature of the spectrometer it is difficult to directly analyze the near-mesh plasma parameters of the system. As such a simulated experiment is performed by placing a biased mesh in front of the plasma source such that spatially resolved probe measurements can be conducted by positioning the probe perpendicular to the direction of the plasma plume.

The experimental configuration is presented in Fig. 4.8. The plasma source used for this experiment is the ICP device operating at an input gas flow rate of 5 L/min, and an input power of 40 W. A biased aluminum electrode with an aperture of 16 mm diameter is placed 7 mm from the ground plate of the plasma source. The aluminum electrode is fixed using a series of bolts connected to an L-bar placed above the plasma source. A 30 mesh size Ni mesh is placed on the plasma-facing side of an aluminum sheet.

Two probe circuits are used to measure the plasma characteristics near a mesh surface. Double probe experiments were used to measure the electron temperature and ion density of the plasma, while a single floating probe was used to measure the plasma potential. Spatially resolved probe measurements are performed by moving the probe along the direction of the plasma plume. Due to the geometrical constraints of the system it is difficult to move the probe

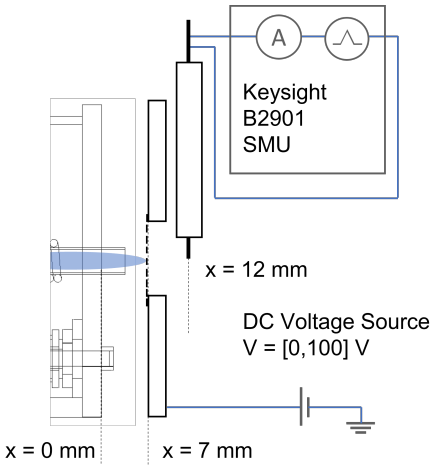

FIGURE 4.8: Schematic diagram of the double probe configuration for measurement of near-mesh plasma parameters.

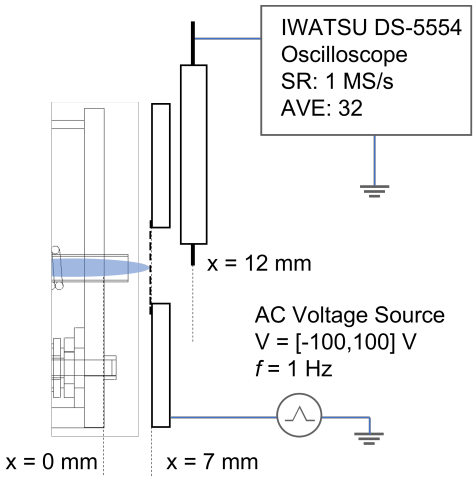

FIGURE 4.9: Schematic diagram of the floating probe configuration for measurement of near-mesh plasma parameters.

along the entire axis of the plume. As such, measurements were taken at x = 6 mm and 12-17 mm relative to the ground plate of the plasma source. With the values obtained at x = 6 mm representative of the parameters observed between the source and the mesh surface, and the values obtained past x = 12 mm representative of the parameters observed past the mesh surface. While it is typical that symmetric traces are the result of double probe measurements, it is difficult to ascertain certain parameters when this is not the case. As such when a peak maximum in the first derivative is not present, the electron temperature can not be calculate.

Changing the applied bias from -100 V to 100 V, the results of the double probe measurements taken past the mesh at x = 12 mm are presented in Fig. 4.10. An increase in the electron temperature of the plasma is seen with increasing mesh biases in both cases with the 30 mesh case reporting a lower temperature up to an applied bias of 30 V where the temperature rapidly

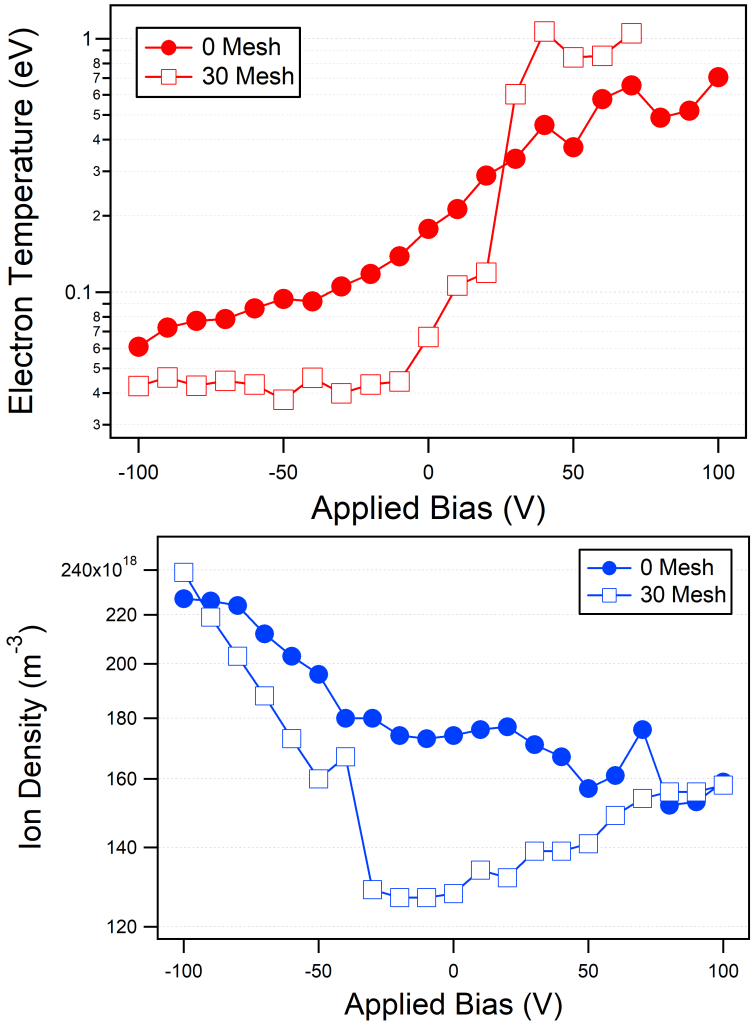

FIGURE 4.10: Observed (Red) electron temperature, and (Blue) ion densities at varying applied mesh biases. The mesh size considered here are the 0, and 30 mesh sizes.

increases surpassing that of the 0 mesh case at higher applied biases. Looking at the ion densities in this case, a decreasing trend for the density of ions with increasing applied bias is observed for the 0 mesh case while the density is minimized near at an applied bias of 0 V for the 30 mesh case. At an applied mesh bias of -90 V to 80 V the 0 mesh case reports a higher density compared to the 30 mesh case.

Applying a sweeping potential from -100 V to 100 V to the aluminum electrode, the floating probe measurements of the plasma potential at a similar probe position is presented in Fig. 4.11. An increasing mesh bias results to an increase in the space potential for the 0 and 30 mesh cases. At negative applied biases, attraction of ions at the mesh surface results to a more negative space charge past the mesh while at a positive applied bias, the attraction of electrons at the mesh results to a more positive space charge. This phenomena can be observed more clearly in the 30 mesh case when compared to the case without a mesh.

The results of the spatially resolved probe experiments considering the case when the mesh is biased at 100 V, -100 V, and 0 V are presented in Fig. 4.14, 4.12, 4.13. In these cases, a DC

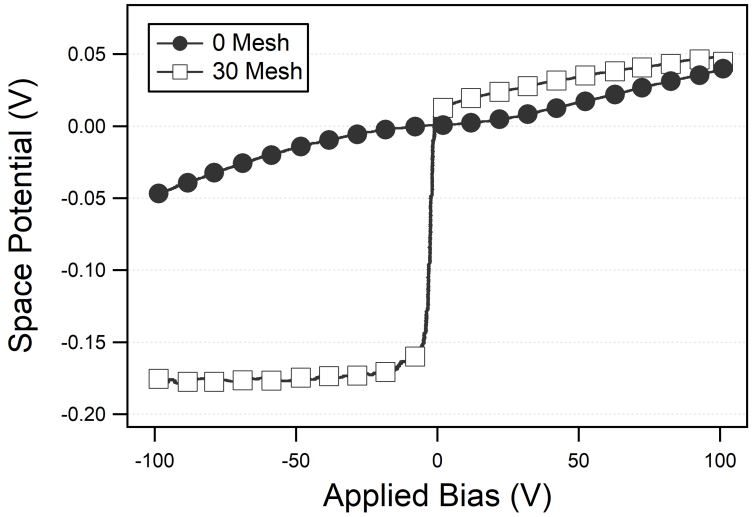

FIGURE 4.11: Observed plasma potential at varying applied mesh biases for the 0, and 30 mesh sizes

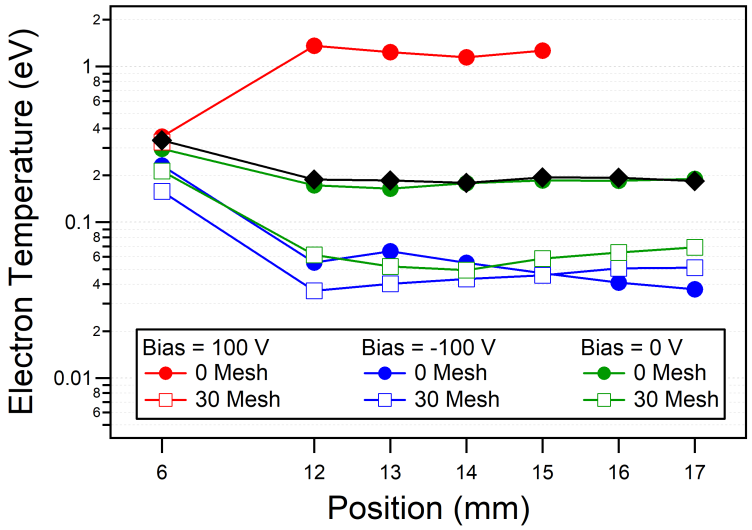

FIGURE 4.12: Effect of varying mesh sizes, and applied mesh biases on the spatial distribution of the electron temperature near the vicinity of the mesh

power supply was used to apply a constant voltage to the aluminum electrode. The black line in all cases indicate the values obtained from the measurements when the aluminum electrode is removed.

Observing the electron temperature of the plasma in the area prior to the mesh, a similar range of temperatures may be observed regardless of the mesh aperture or applied bias. Past the mesh, the temperature decreases when the mesh is present at an applied bias of 0 V. This indicates the physical effects of mesh transparency. Decreasing the applied bias to -100 V results to a decrease in the energy for the 0 mesh case, and a slight decrease for the 30 mesh case. The decrease in energy may be due to the repulsion and retardation of electrons as they approach the mesh. When the bias is increased to 100 V, the energy increases due to the acceleration of

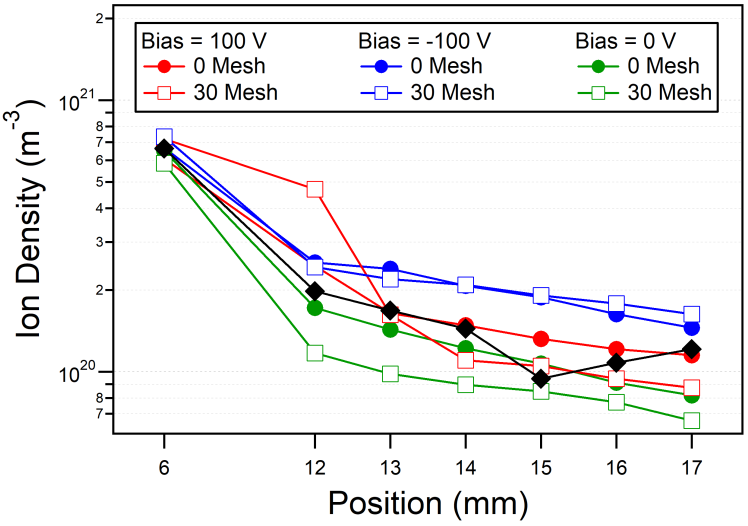

FIGURE 4.13: Effect of varying mesh sizes, and applied mesh biases on the spatial distribution of the ion density near the vicinity of the mesh

electrons past the mesh aperture, for the 30 mesh case however no distinct transition region was observed.

Analyzing the density of ions with reference to the applied mesh biases shows a possible exponential decrease in the ion density as the probe is moved further away from the source. In the area prior to the mesh, the ion density is similar in all cases as well. Past the mesh, physical effects of mesh transparency during the time the mesh was biased at ground potential was observed when comparing the densities of the 0 mesh and 30 mesh cases. At a bias of -100 V, Similar densities are observed for both the 30 and 0 mesh. Both mesh cases exhibit an increase in ion density when compared to the case when the mesh was biased at ground potential, indicating an increased ion density due to ion acceleration past the mesh. At a bias of 100 V, a higher density past the mesh was observed for the 30 mesh case which decreases as you move further away. The decrease in density may be attributed to ion retardation or repulsion due to the highly positive applied bias.

From the single probe experiments, localized space potential measurements were obtained at varying applied mesh bias. In the area before the mesh, the space potential fluctuates relative to the applied mesh potential with the 0 mesh case being more susceptible to such fluctuations. Past the mesh, a more uniform space potential distribution is observed at varying probe positions. At a bias of 100 V, a positive space charge is observed due to the attraction of electrons to the mesh, while at a bias of -100 V a negative space charge is observed, ions are attracted to the mesh leading to a more negative space charge. The magnitude for the 30 mesh case, here is larger than that of the 0 mesh case which may indicate a better ion collection mechanism for the 30 mesh case.

Overall, the presence of a mesh itself reduces the density, temperature, and space potential of the plasma. For the 30 mesh case, during the time the shutter is biased negatively an influx of slow moving charged species (0.04 eV) enters the spectrometer. During the time the spectrometer switches to a positive field the presence of energetic ions ($\geq$ 1 eV) are present near the

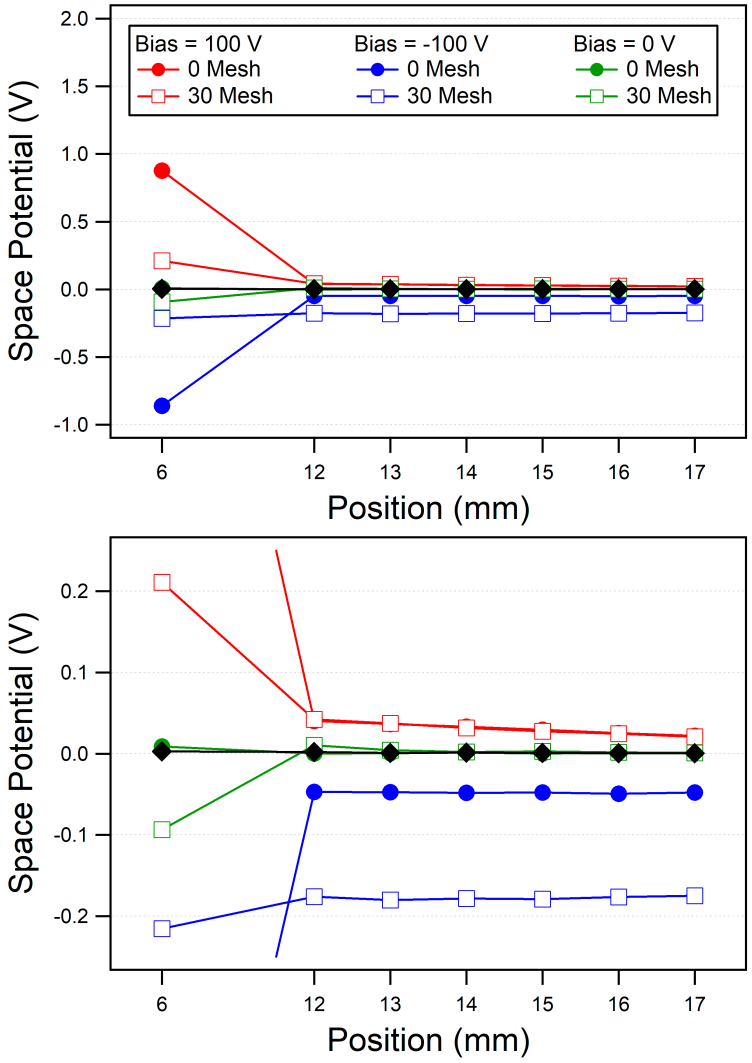

FIGURE 4.14: Effect of varying mesh sizes, and applied mesh biases on the spatial distribution of the plasma potential near the vicinity of the mesh.

mesh at a density half than what is observed during the time the mesh is biased negatively.

As such the shutter allows the passage of more ions when a negative potential is present. In contrast, the shutter acts as a high pass filter when a positive potential is applied allowing only highly energetic particles to pass through the area. Additionally, the presence of a mesh acts as a diffusive filter limiting the amount of particles passing through the mesh.

4.3 Summary

A compact design of an ambient drift tube mobility spectrometer is developed for ion mobility analysis. The design includes a bipolar mesh-gated shutter, a drift region, and an electronic detector to obtain a distinct current signal at electric fields of up to 33.3 V/cm. Comparing the ion sources intended for mobility spectrometry, only the CCP source was able to realize an asymmetric signal from which mobilities may be calculated from. The results show that the presence of a mesh at the plasma facing side of the spectrometer results to an observed

phase-locked signal at the detector. A time varying voltage at the shutter is enough to produce this type of signal at the detector even in a zero electric field drift region.

Analysis of the near mesh plasma parameters show that the area between the mesh and the plasma source show limited change to the electron temperature and ion density when the a bias is applied to the mesh. A uniform electron temperature, and a decreasing ion density that varies with the applied mesh bias is observed past the mesh. In contrast, the space potential in the area between the mesh and the plasma source greatly increases or decreases in accordance with the applied bias. Past the mesh, a more uniform behavior across all applied voltages is observed.

The mesh thus acts as a high-pass filter allowing only highly energetic particles to pass when biased positively. If biased negatively, the mesh allows more ions to enter at resulting to a lower observed electron energy. It is likely that the highly energetic particles are what causes the DC offset current observed during the positive and negative phases of the spectrometer signal.

Chapter 5

POSITIVE FIELD MOBILITY SPECTROMETRY

This section aims to address the process of obtaining ion mobilities from the spectrometer signal. We begin by introducing the typical trace observed during the positive field transport, highlighting the prominent features of the graph, their underlying causes, and their significance. Next, we delve into the impact of altering specific parameters within the device, such as the applied electric field and the mesh aperture used for the shutter, on the behavior of the trace. Finally, we focus on the positive phase behavior of the signal, where the ion arrival time could be extrapolated from the signal itself. This allows us to determine the mobilities of ions, providing valuable insights into their characteristics and behavior. The data presented in this chapter correspond to the work done by the author described in a previous publication [46].

5.1 Positive Field Signal

The shutter region inside the spectrometer is the area that simultaneously allows and limits the transport of charged species into the spectrometer. When biased negatively, it accumulates positive species which are then expelled from the area when during the subsequent positive phase. If a positive electric field due to a positive applied V_{Bias} is present, then the spectrometer configuration in this case results to a signal where the mobility of positive ions may be calculated from.

In this scenario, a distinct current can be observed during the time a positive field is present inside the spectrometer. The typical current behavior, and the corresponding first and second derivatives are presented in Fig. 6.1. We define the positive and negative phases as the time when shutter is at a positive, and negative potentials respectively. Further classifying the observed regions of the signal, we define four regions- R1, R2, R3, R4. The regions R1, and R3 correspond to the transition regions, while R2, and R4 correspond to the steady-state current regions. The transition regions are characterized by a time varying signal, while the steady-state regions correspond to the area with an observed constant current. Typical time domains for these regions are R1 (0-20 ms), R2 (20-40 ms), R3 (50-80 ms), and R4 (80-95 ms).

The average value of the steady state currents are referred to as I_{SS-} and I_{SS+} located in R2, and R4 respectively. The subscripts for this case refer to the negative or positive phases where the currents are located. In R1, we define the arrival time t_{a-} as the time at which the first derivative of the trace is minimized, and the time constant τ_{D-} as the point at which the first and second derivative reach zero. Similarly, in R4, the arrival time t_{a+} is the point at which the first derivative is maximized, and the time constant τ_{D+} is the point at which the first and second derivatives reach zero. All arrival times and time constants are measured relative to the onset of the changing shutter potential which occurs at t = 0 ms for the negative phase, and t = 50 ms for the positive phase.

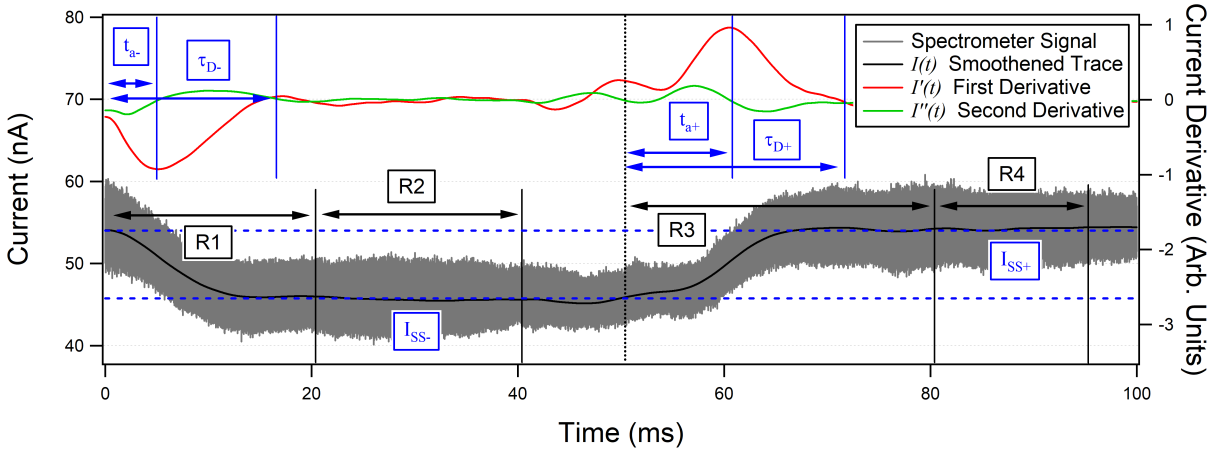

FIGURE 5.1: Charge transport in a 30 mesh shutter with V_{Bias} = 10 V. At t = 50 ms, as denoted by the dashed black line, the shutter potential ($V_{Shutter}$) transitions from -100 V to 100 V. Prior to analyzing the first and second derivatives of the signal, the spectrometer undergoes a smoothing process.

5.2 Mesh Dependent Current Behavior

The addition of a mesh in the spectrometer results to an asymmetric behavior in the observed current. The study investigates the effect of varying mesh size on the positive field detector current by analyzing the changes in the behaviors of I_{SS}, t_a, and τ_D. The experimental setup utilizes mesh sizes of 0, 30, 100, and 200 mesh sizes which correspond to an aperture size of 10^4, 600, 150, and 75 μm respectively. The ions used in this study are generated utilizing the CCP source with an input power of 40 W, and a gas flow rate of 5 L/min.

The detector current measured for all mesh sizes are shown in Fig. 6.2. The dashed line at t= 50 ms corresponds to the time at which the potential switches. The applied bias from 1 - 100 V corresponds to an electric field of 0.33 - 33.33 V/cm in the drift region. Data was taken at a sampling rate of 5 MS/s with an oscilloscope average of 32. For the case of the 0 mesh condition, the detector current solely increases with V_{Bias} with no observable difference between the positive and negative phase I_{SS}. The addition of a mesh, observed in the cases for the 30, 100, and 200 mesh conditions, shows a distinct change in I_{SS} relative to the shutter potential up to V_{Bias} = 10 V. The presence of two steady state behaviors for the case of the 30 mesh condition was observed up to V_{Bias} = 5 V.

5.2.1 Steady State Current

The observed changes in I_{SS} during the positive and negative phases across the mesh sizes are shown in Fig. 5.3. The values presented are measured against the steady-state current at V_{Bias} = 0 V. Increasing mesh transparency resulted to the increased observed current at the detector. This observed increase however, does not show a linear correlation with V_{Bias} in both the negative and positive phases. This suggests that the ion flux reaching the detector is not due solely to the increase in velocity due to the increasing electric field. It is also likely that this

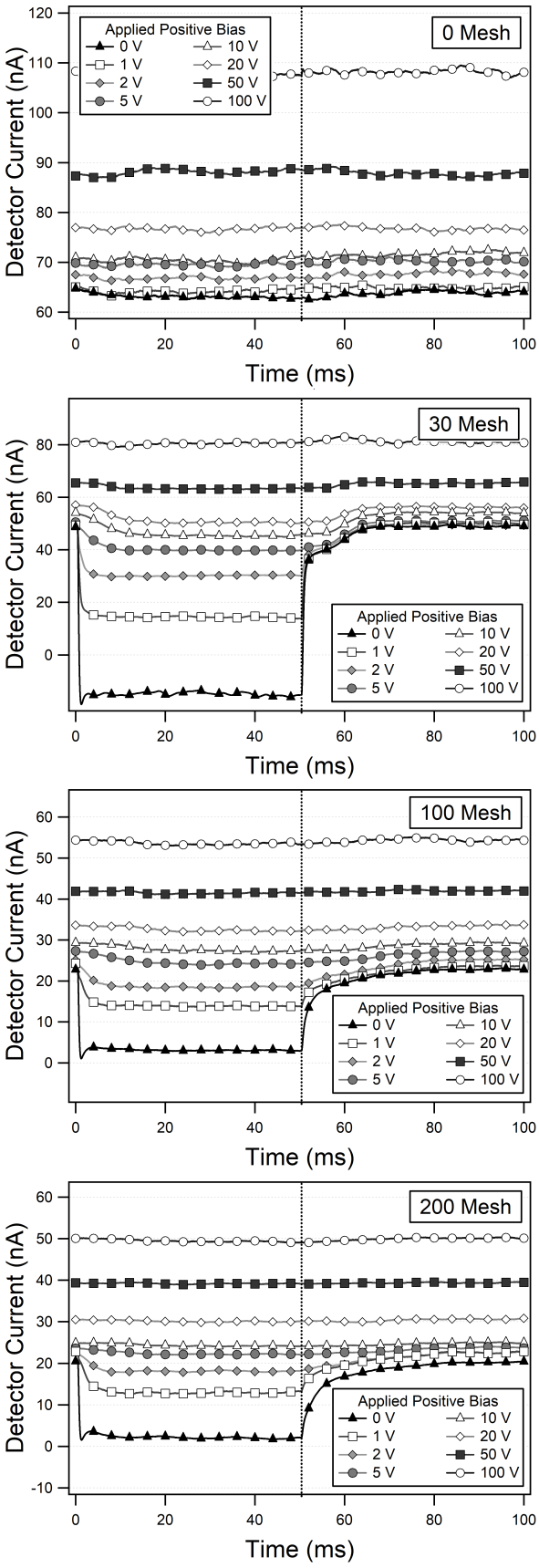

FIGURE 5.2: Observed detector signal in a positive field through 0, 30, 100, and 200 mesh sizes.

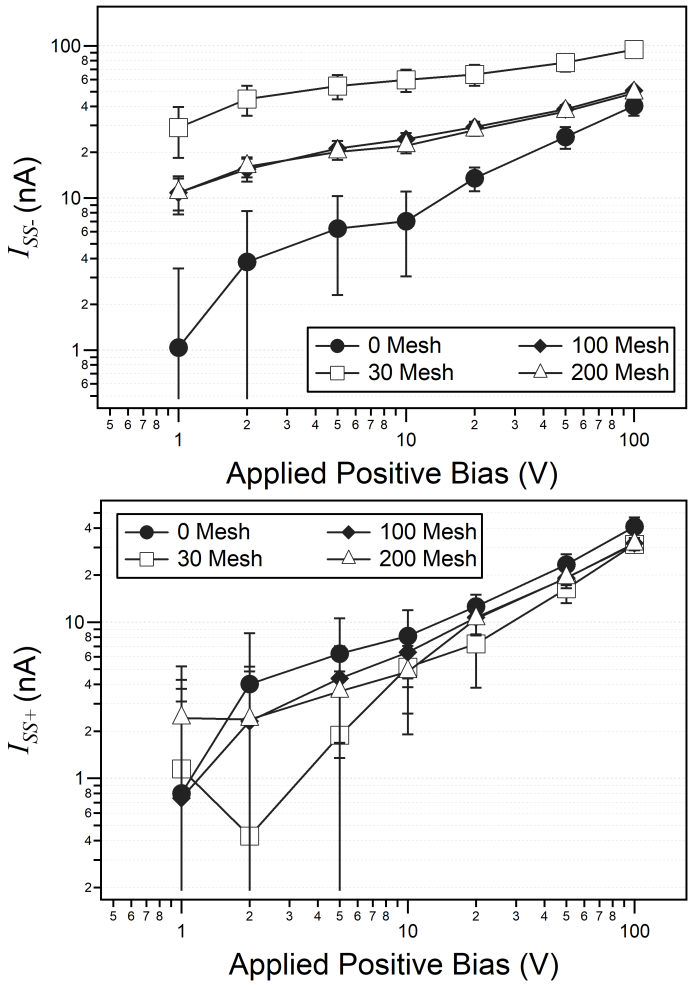

FIGURE 5.3: The effect of increasing electric fields on I_{SS} observed during the (Top) negative phase, and (Bottom) positive phase across varying mesh sizes. The current is measured relative to the baseline steady state current at V_{Bias} = 0 V. Error bars show the standard deviation over three experiments.

is a result of the non-linear behavior of the electric field due to the large shutter potential when compared to V_{Bias}.

By subtracting the negative phase from the positive phase I_{SS}, we can gain insight into the observed asymmetric behavior (Fig. 5.9). Across all cases, the asymmetric behavior becomes more pronounced at lower V_{Bias} values, exhibiting a linear trend from V_{Bias} = 1 V to 50 V when the mesh is present. However, the degree of asymmetry diminishes at V_{Bias} = 100 V. A similar asymmetric behavior is observed for the 100 and 200 mesh cases, with the 100 Mesh configuration displaying a greater degree of asymmetry from V_{Bias} = 2 V to 50 V. Although the zero mesh case exhibits the highest observed I_{SS} during the positive phase, it demonstrates no asymmetric behavior at all applied potentials.

5.2.2 Transient Current Analysis

The arrival time, t_a, , and the time response of the signal, τ_D, of ions during the positive and negative phases with the mesh addition are presented in Fig. 5.6, and Fig. 5.7 respectively.

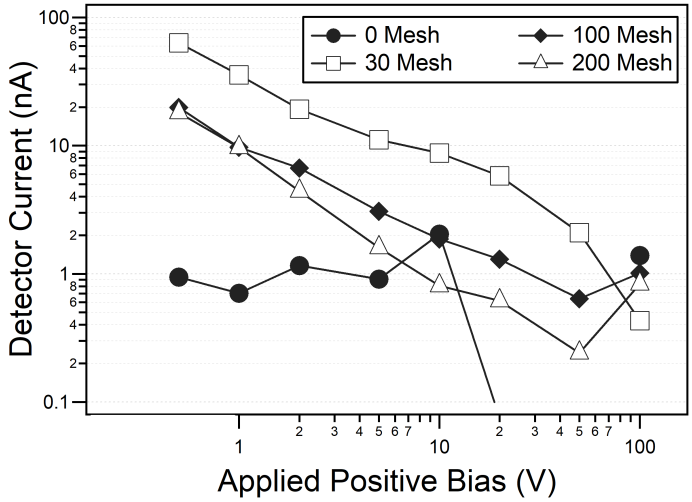

FIGURE 5.4: Observed asymmetric current between the positive and negative phase I_{SS} with increasing electric fields. The average standard deviations for each mesh type are 4.7, 2.7, 2.3, and 2.4 nA for the case of 0, 30, 100, and 200 mesh sizes respectively.

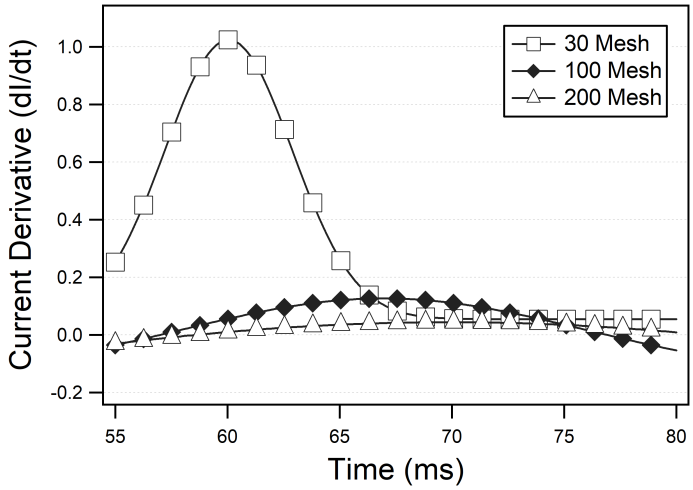

FIGURE 5.5: First time derivative of the detector current at a V_{Bias} = 10 V. The derivative trace was then fitted to a Gaussian convolution to elucidate the presence of peaks in the given time domain

From the spectrometer signal, t_a can be calculated from the time value of the maximum and minimum peak values found in the first derivative during the positive, and negative phases respectively. Following t_a, τ_D could be defined as the point where a stable current is present and thus can be expressed as the time at which the second derivative is 0 after the local minima and maxima where t_a is located at.

A comparison of the first derivative across varying mesh sizes during the positive phase cans be seen in Fig. 5.5. To calculate the higher order derivatives from the initial spectrometer signal, a moving average smoothing algorithm with a length of 3% of the maximum number of points was applied first. This is followed by applying a Savitsky-Golay filter to the signal

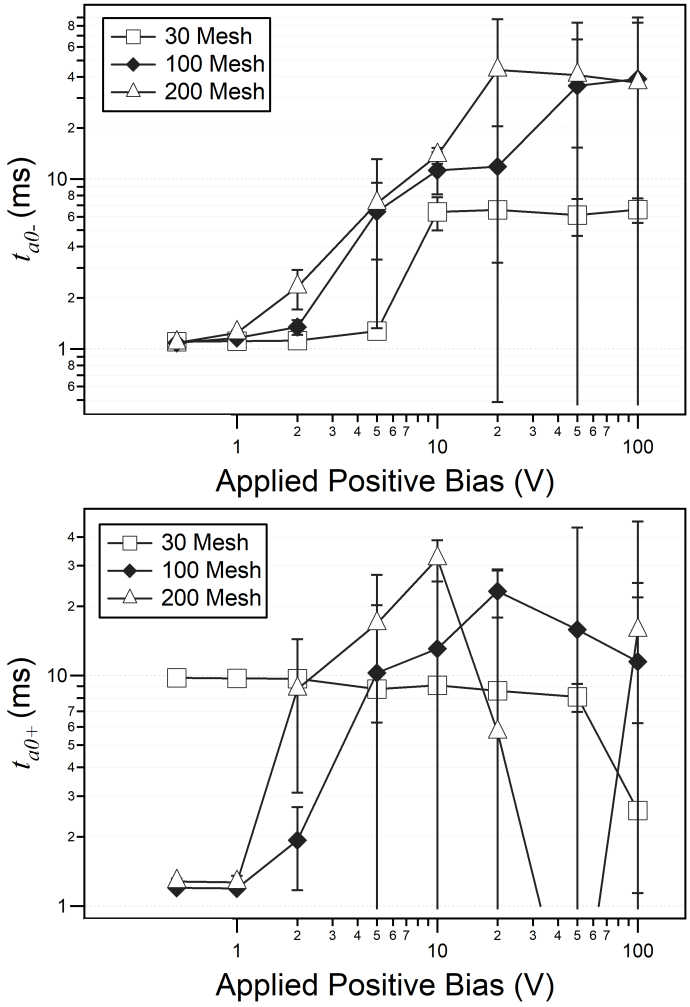

FIGURE 5.6: Effect of increasing V_{Bias} on the ion arrival time, t_a, during the (Top) negative phase, and (Bottom) positive phase. Derivatives were calculated using the center-difference method in IgorPro after successive smoothing of the original spectrometer signal.

with a length of 1% four times in succession. Applying these processes allow the numerical calculation of higher order derivatives with minimal resultant noise [48]. Since the arrival time of ions are obtained by analyzing the derivatives of the spectrometer signal, when minimal asymmetric behavior is present the resulting values present a large degree of error.

During the negative phase, a distinct t_a is observed at an applied bias lower than 20 V. A general trend of increasing t_a is observed as the bias is increased with the case of the 100, and 200 mesh sizes showing a higher magnitude than the 30 mesh case. This behavior is possibly a result of electrons being retarded in the spectrometer at higher electric fields. Observing τ_D, it can be seen that the constant current behavior increases as well with applied biases which suggests that the retardation of electrons is a steady-state phenomenon in this scenario. Neither t_a, nor τ_D however in this scenario shows a linear dependence on the applied bias in all mesh cases.

During the positive phase, an increasing behavior of t_a, and τ_D is observed at V_{Bias} = 1

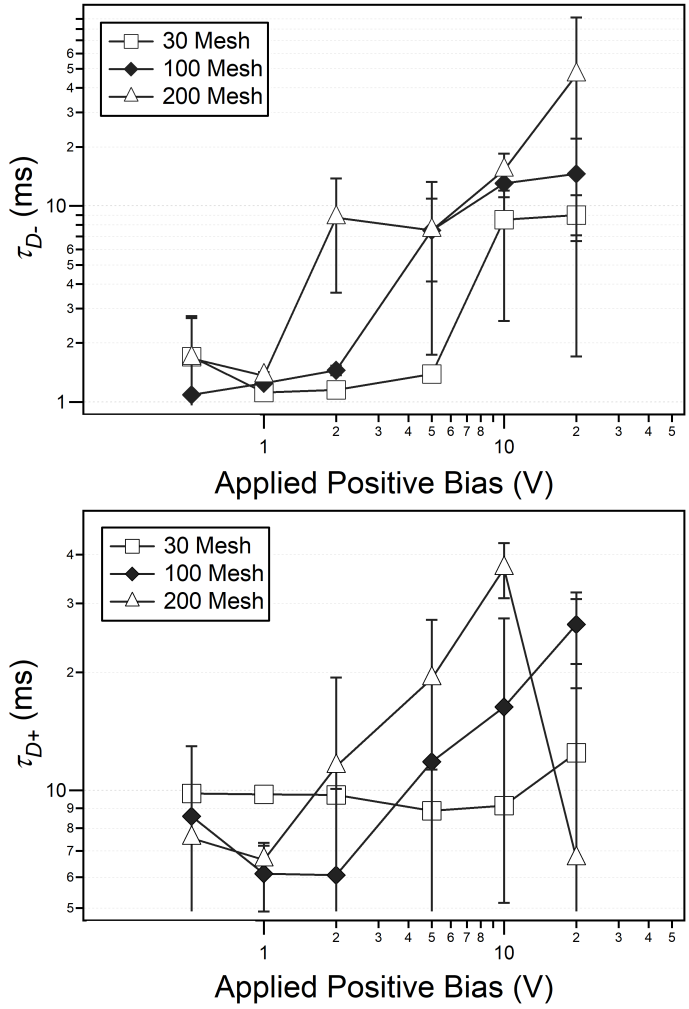

FIGURE 5.7: Effect of increasing V_{Bias} on the detector time constant, τ_D, during the (Top) negative phase, and (Bottom) positive phase.

to 20 V for the case of the 100 and 200 mesh sizes. For the case of the 30 mesh, a decreasing trend could be observed. Typically with increasing applied electric fields, it should be that the ions would travel faster through the spectrometer resulting to faster arrival times. However this is not the case for the 100, and 200 mesh sizes. It is possible that this behavior could be related to the increased presence of electrons during the negative phase which contributes to recombination effects inside the system.

Overall, due to the inconsistency of the 100 and 200 mesh cases for the analysis of the arrival time of ions when compared to the expected typical physics phenomena observed for ion mobility spectrometry, it is not possible to use these mesh sizes for measurements of such mobilities. In contrast, the 30 mesh case exhibits the expected phenomenon where such mobilities may be calculated from.

Ar-N_2 Mixture Ar%	Mobility ($cm^2 \cdot V^{-1} \cdot s^{-1}$)
1%	2.35±0.02
3%	2.29±0.02
5%	2.23±0.03
10%	2.20±0.01
20%	2.22±0.02
30%	2.18±0.03
40%	2.19±0.02
50%	2.18±0.03
60%	2.18±0.02
70%	2.16±0.03
80%	2.15±0.02
90%	2.12±0.04
95%	2.09±0.03
97%	2.06±0.01
99%	2.02±0.01

TABLE 5.1: Mobility of the ions observed for the Ar-N_2 mixture ratios studied. Data was obtained for E/N of 15 Td, at 8 Torr and 293 K. Data was obtained from the study of Santos, et. al. [49].

Reduced Electric Field [Td]	Mobility [$cm^2 \cdot V^{-1} \cdot s^{-1}$]
5	2.48
6	2.48
8	2.49
10	2.49
12	2.49
15	2.49
20	2.49
25	2.49
30	2.49
35	2.49
40	2.49
50	2.50
60	2.50
70	2.51
80	2.52
100	2.56

TABLE 5.2: Reduced mobility coefficients of O_2^+ ions in air. Data was obtained at a gas temperature of 300 K. [50].

5.3 Measurement of Ion Mobilities

The typical case for measuring ion mobilities can be shown during the time $V_{Bias} = V_{Shutter}$. This configuration allows the formation of a uniform electric field from the shutter towards the detector. The typical operation case is shown in Fig. 5.8. Measurement of ion mobilities in this

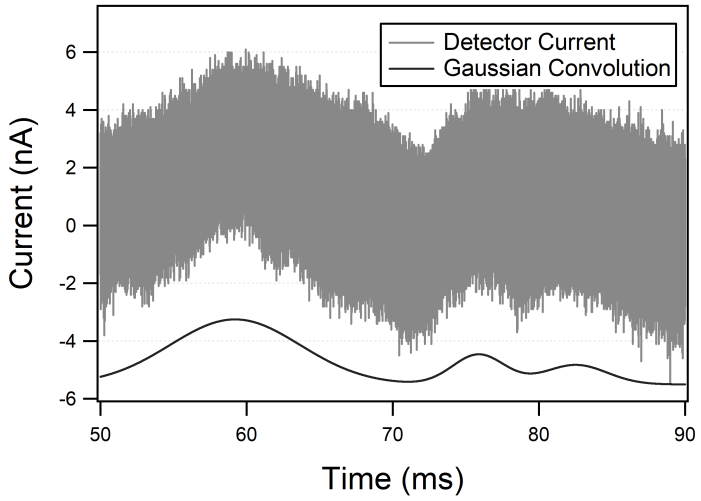

FIGURE 5.8: Observed positive phase detector at V_{Bias} = 100 V. Gaussian peak fitting of the detector current was performed using the MultiPeak function in IgorPro V6.04

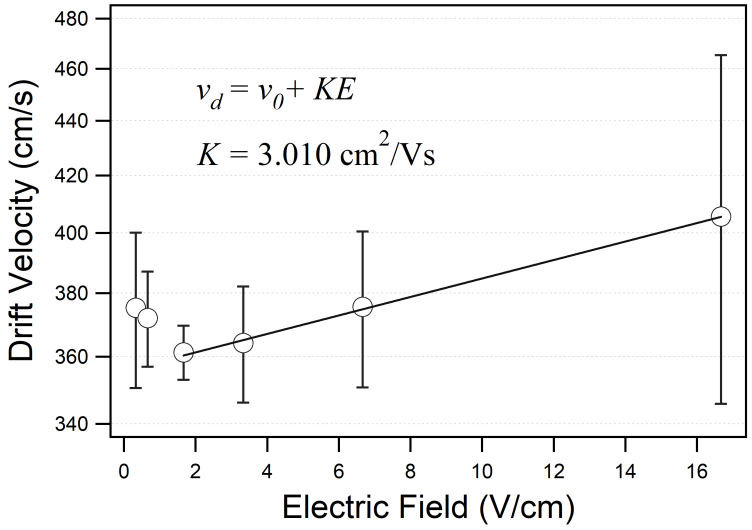

FIGURE 5.9: Linear regression of the drift velocities corresponding to the current-time derivative peak of the observed spectrometer signal in a 30 mesh transport at low electric fields from t = 55 - 80 ms. Error bars indicate the standard deviation of the drift velocities over three experimental trials. V_{Bias} = 5 - 50 V corresponds to an average electric field of 1.67 to 16.67 V/cm.

case would use the peaks observed from the detector signal to correspond to the time of flight of ions in the spectrometer. In particular for this case, the peaks observed correspond to the mobilities K = 12, 4.1, 3.3 cm^2/Vs for the peaks observed at t_a = 59.21, 75.87, and 82.52 ms, respectively

We present here a theory for ion transport inside the mobility spectrometer for the 30 mesh case shutter at low applied electric fields. During R2, due to the negative shutter bias ions are collected at the mesh such that when the shutter switches to a positive potential, the ions are expelled from the shutter towards the detector. The weak electric field inside the spectrometer

however can not accelerate the ions significantly such that we account for the velocity of the ions upon being expelled from the shutter. This can be done by adding an initial velocity component to the original drift equation such that, $v_d = v_0 + KE$. Applying a linear regression to the spectrometer signal observed at t = 55-80 ms, and V_{Bias} = 5-50 V, reports a slope showing a mobility value of K = 3.0 cm^2/Vs, and an initial velocity v_0 = 350 cm/s. This velocity is close to the ion acoustic velocity. The mobility data are compared with the reported reduced mobilities normalized to 1 atm and 273 K to determine the ion species.

The third peak in the typical case, and the observed mobility in the low electric field configuration correspond to the reduced mobilities of K_0 = 3.0 and 2.7 cm^2/Vs, respectively. These peaks can be attributed to possibly the presence of oxygen in the source plasma as was shown by optical emission spectroscopy in the earlier chapters (Table 5.2). It is also likely that other ions such as Ar^+ (Table 5.1), N_2^+, CO^+, H_2O^+, and O_2^+ can be attributed to the aforementioned peaks since they share a similar range of mobility. The presence of molecular species in the source plasma however has yet to be confirmed.

5.4 Summary

The principle for low-electric field ion mobility spectrometry for positively charged species has been studied for diagnostics of an atmospheric pressure plasma source. With the addition of a wire mesh at the shutter electrode, a phase dependant signal was observed at low electric field intensities. Results show that a decreasing arrival time due to increasing electric fields were observed for the case of the 30 mesh, that was not exhibited in higher mesh sizes. Analysis of the ion transport in the drift field shows the presence of peaks in the time-of-flight spectrum during the positive phase corresponding to the reduced mobilities of 3.0 cm^2/Vs, and 2.7 cm^2/Vs measured at an applied bias of 100, and 5-50 V respectively. The peak could possibly be attributed to the drift of O^+ ions inside the spectrometer.

Chapter 6

NEGATIVE FIELD MOBILITY SPECTROMETRY

In contrast to the previous chapter, this section aims to measure the mobilities of negatively charged particles, primarily electrons, from the spectrometer signal utilizing a negative electric field in the drift region. In a similar manner, we introduce the typical trace observed during the negative field transport. Then we examine the effect of modifying the shutter mesh aperture, and the applied electric field on the observed detector signal. Finally we try to explain the phenomena that occurs during the negative field transport based on the experimental data.

6.1 Negative Field Signal

The negative field signal is much more distinct compared to its positive field counter-part due to the clearly observed peaks during the phase onsets. To more effectively discuss the behavior of the observed signal, parameters will be introduced in a similar manner with the previous chapter.

A typical trace of the negative field transport can be found in Fig. 6.1. The dashed line at t= 50 ms corresponds to the time at which the potential switches. The applied bias,V_{Bias}, from -1 to -100 V corresponds to an electric field of -0.33 to -33.33 V/cm in the drift region. Data was taken at a sampling rate of 5 MS/s with an oscilloscope average of 32. The regions of the signal can be described into the steady state and transition regions as was the case in the positive field signal discussion. In this case the four regions have the time domains of R1 (0-20 ms), R2 (20-40 ms), R3 (50-70 ms), and R4 (80-90 ms).

The initial oscilloscope trace is smoothened using a moving average algorithm with a length of 0.2 % of the maximum number of points. A 4th order Savitsky-Golay algorithm is applied to the trace four times prior to the numerical calculation of the first derivative using a central difference approximation with a length of 0.5 % of the maximum number of points. The second derivative was calculated using a similar method but applied to the first derivative trace instead.

The steady state regions, R2, and R4 both contain information on the steady state current values of the signal. In particular, the average current value in R2 is the negative phase steady state current, I_{SS-}, while the mean current value in R4 is the positive phase steady state current, I_{SS+},. The values of the steady state currents were calculated from the initial oscilloscope trace and not from the smoothened traces.

In R1, a strong initial negative peak is observed which then saturates in the succeeding region. To characterize the behavior of this peak the following constants, t_{a0-}. τ_{D-}. and PI_-, are defined. The peak time of arrival, t_{a0-}, is defined as the time at which the peak minimum obtained from the original oscilloscope trace occurs relative to the onset of the negative phase. From this definition, $I(t_{a0-})$ is the peak minimum current and is typically measured relative to the steady state current, I_{SS-}. The time constant, τ_{D-}, can be defined as the point at which

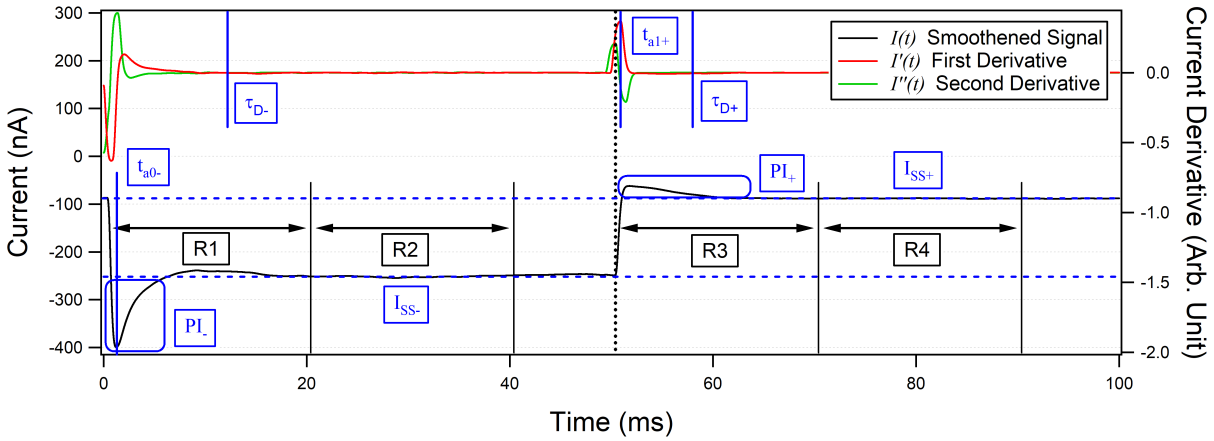

FIGURE 6.1: Charge transport in a 100 mesh shutter with V_{Bias} = -50 V. At t = 50 ms, as denoted by the dashed black line, the shutter potential ($V_{Shutter}$) transitions from -100 V to 100 V. Indicated areas of the correspond to to the parameters measured in this section.

first and second derivative of the signal reaches zero relative to the onset of the negative phase. We introduce a new parameter, PI_{-} [nA ms], which is defined to be the integral of the peak. The integral is the summation of currents below the steady state current value. Since current is proportional to the flux of charged species on a surface, this parameter can describe the relative charge contribution attributed to the peak only.

Following the negative phase, an increase in the current is observed in the R4 region of the positive phase. For all V_{Bias} cases, the transition from a lower current to a higher one is always apparent when a mesh is present. The increasing current behavior in this region can be described in terms of the parameters: t_{a1+}, τ_{D+}, and PI_{+}. The peak arrival time of the first derivative, t_{a1+}, is the time at which the first derivative is maximized relative to the onset of the positive phase. The corresponding maximum value of the peak is defined to be $I'(t_{a1+})$. In this case, we consider the first derivative instead of the case of the original trace since the presence of a peak is not present for all V_{Bias} cases but a maximum value of the first derivative does. The time constant, τ_{D+}, and the peak integral PI_{+} are defined similarly to their counterparts in R1 but are measured relative to the onset of the positive phase, and I_{SS+} respectively.

6.2 Mesh Dependent Current Characteristics

The current signal obtained from the spectrometer during the time a negative electric field is applied to the drift region are presented in Fig. 6.2. The signal was obtained at with a Ni shutter mesh with sizes of 0, 30. 100. and 200 mesh sizes. Like in the positive phase signal experiments, the shutter oscillates with a square wave voltage at a frequency of 10 Hz, and V_{pp} = 200 V. The applied bias to the primary plate ranges from V_{Bias} = 0 to -100 V, corresponds to an electric field of $\sim$ 0 to -33.3 V/cm in the drift tube region of the spectrometer. The experiment was repeated 3 times and the values presented in the succeeding parts of this section describe the average values and the standard deviation of these experiments.

During the time no mesh is present, or 0 mesh condition, no significant change was observed in the current relative to the shutter potential at $V_{Bias} \leq 20$ V. Further increasing the applied bias to 50 V and 100 V, the observed current becomes more negative and the presence of a phase-locked behavior becomes apparent. When the mesh is added to the spectrometer shutter, this phase-locked behavior becomes present in all V_{Bias}.

Characteristic of this behavior in these systems is the increase in current observed when the shutter switches from a negative to a positive potentials. For the case of the 30, 100, and 200 mesh sizes, a distinct initial peak is present when the shutter switches to a negative potential at all applied V_{Bias} . During the time $V_{Bias} \geq 20$ V, the presence of a distinct peak when the shutter switches to a positive potential similarly becomes apparent in these mesh conditions.

6.2.1 Steady State Current

The observed values for the steady state currents, I_{SS-}, and I_{SS+} are presented in Fig. 6.3. An increasingly negative electric field reports an increasing trend in the observed negative current during both the negative and positive phases relative to the current observed during the time V_{Bias} = 0 V. During the negative phase, the current rises steadily for the mesh cases but increases abruptly at V_{Bias} = -50 V for the 0 mesh condition. The positive phase behavior reports a decrease of the observed currents at -20 V for the 100, and 200 mesh cases, and at -50 V for the 30 mesh case.

Observing the asymmetric behavior of the spectrometer signal shows a saturation of the signal at $V_{Bias} \geq$ -10 V for the mesh cases reporting a mean asymmetric current of 811.3, 180.6, and 91.4 nA for the 30, 100, and 200 mesh cases respectively. The asymmetric behavior steadily increases in the same V_{Bias} range for the case of the 0 mesh.

6.2.2 Time Response of the Detector Signal

The observed time constants for the positive and negative phases during a negative field transport are reported in Fig. 6.5. Since the time response is a result of the asymmetric behavior of the observed current, the following graphs report the data for the mesh cases only. For the 0 mesh case, the observed time constants during the negative, and positive are 8.5 and 8.1 ms, and 9.6 and 9.2 ms corresponding to V_{Bias} = -50 V, and -100 V respectively.

It can be seen that during the negative phase, time constant behaviors increases up to a maximum at -10 V and decreases afterwards for all mesh cases. Across the mesh cases, the 30 mesh case reaches the constant current behavior the slowest up to an applied bias of -10 V where it then speeds up having the highest τ_D at an applied bias of -50, and -100 V. The opposite case occurs with the 200 mesh case where it initially has the fastest response up to -10 V but ends up reporting the slowest response at -100 V.

The positive phase reports a decrease in the observed time response of the signal with increasing negative applied bias. When comparing the 30 mesh case to the other mesh cases, the contrast of the behavior in the negative phase is seen. The 30 mesh case at reports having a similar behavior with the negative phase such that at low applied biases this case has the fastest τ_D while at an applied bias of 100 V it reports having the slowest time constant. The 200

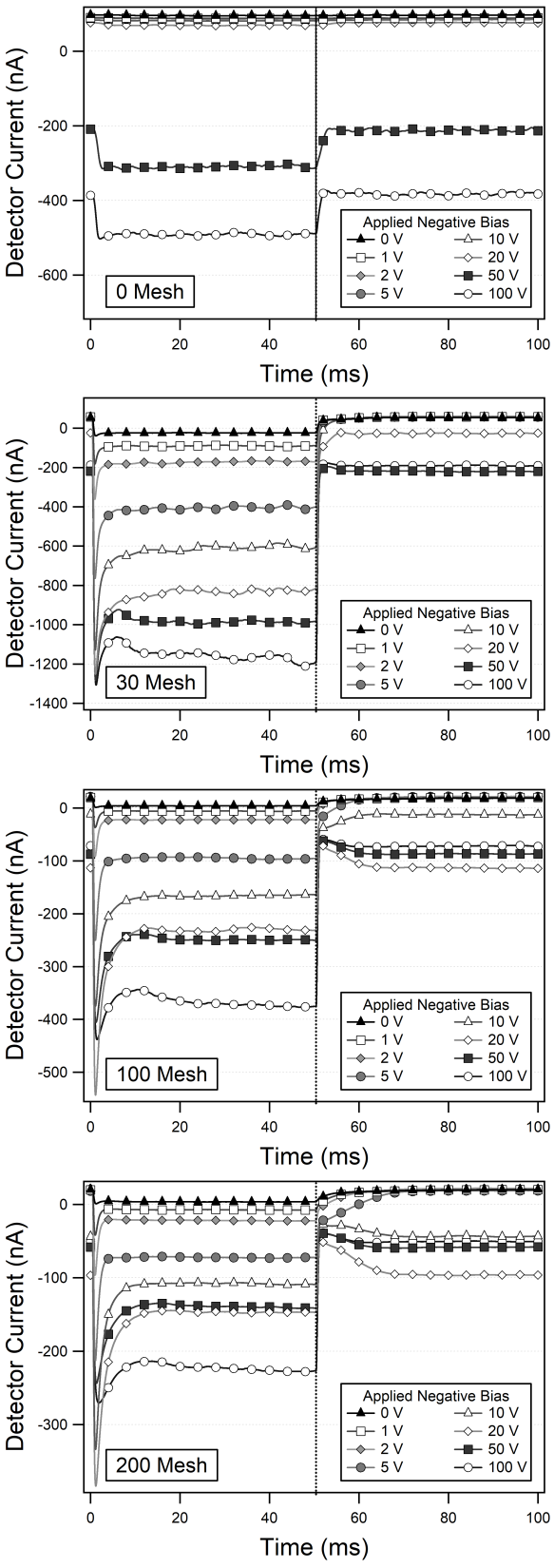

FIGURE 6.2: Observed detector signal in a negative field through 0, 30, 100, and 200 mesh sizes. The dashed line at t= 50 ms corresponds to the time at which the potential switches. Data was taken at a sampling rate of 5 MS/s with an oscilloscope average of 32.

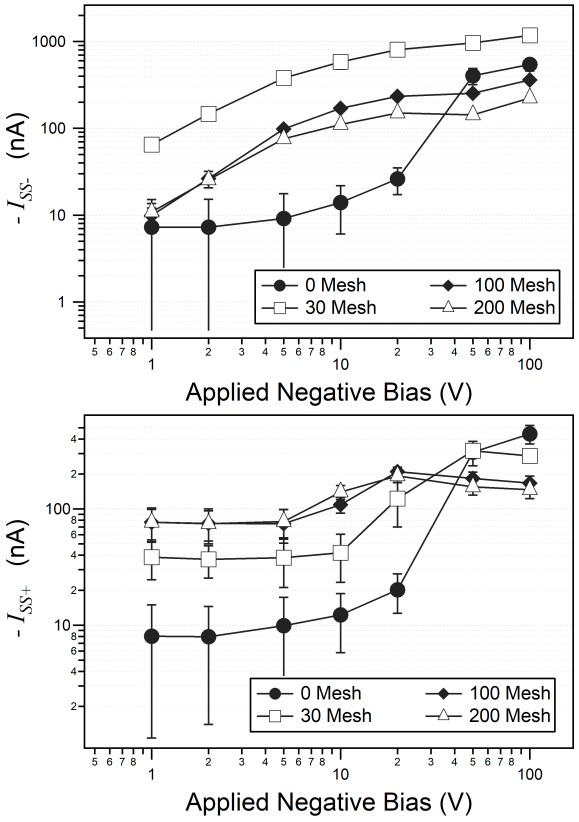

FIGURE 6.3: Observed steady state currents in the (Top) negative phase, and (Bottom) positive phase through 0, 30, 100, and 200 mesh sizes

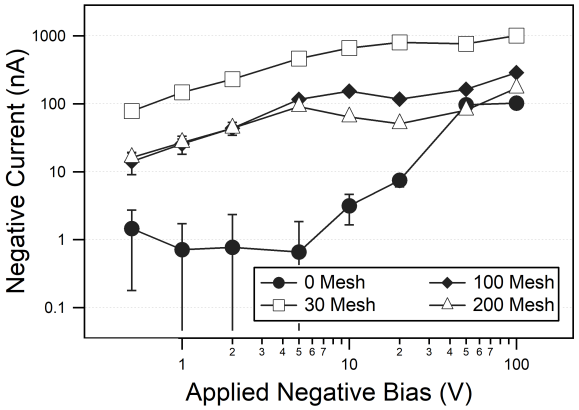

FIGURE 6.4: Asymmetric current behavior across the mesh sizes during a negative field transport.

mesh case seems to follow this contrast while the 100 mesh case reporting a behavior that is the mean of both cases.

6.2.3 Analysis of Visible Peaks

The arrival times, peak values, and integral measurements are reported in Fig. 6.6, 6.7, 6.8. Analyzing the negative peak behavior, the arrival time, t_{a0-} increases with a more negative

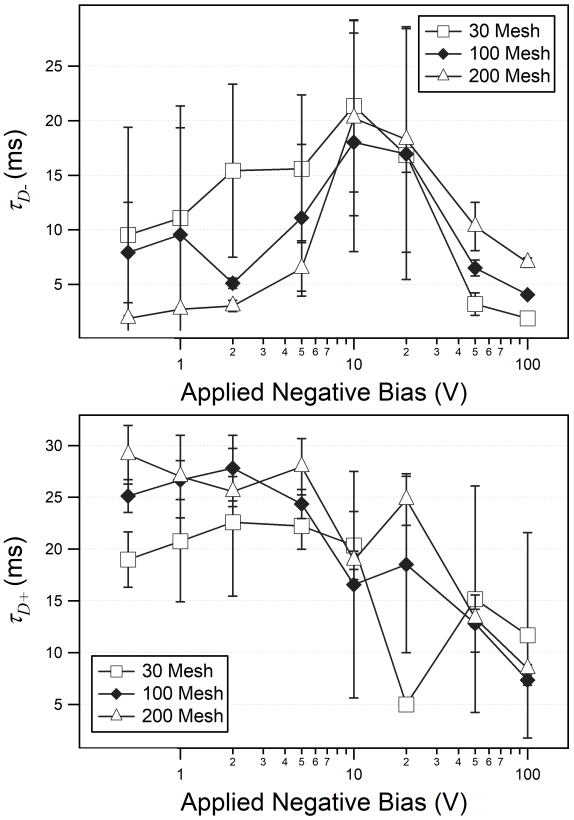

FIGURE 6.5: Time response of the detector signal during the (Top) negative phase, and (Bottom) positive phases.

applied bias. The analysis reports that the 200 mesh case allows for the slowest arrival time while the 30 mesh case allows the fastest peak arrival time.

The behavior of the peak current, I(tao-) measured against I_{SS-} shows a similar behavior with that of the peak integral PI_{-}. The increasing trend in the current can be correlated to increasing mesh transparency that is the 30 mesh exhibits the highest current while the 200 mesh condition exhibits the lowest. Characteristic across all mesh sizes is a maximum charge transfer occurring at an applied bias of -10 to -20 V as seen in the peak current magnitude and the peak integral. The values for the peak integral are similar for the 100 and 200 mesh cases at all applied biases.

During the positive phase, the time at which the first derivative is maximized, t_{a1+}, decreases up to V_{Bias} = 20 V for the case of the 30 and 100 mesh sizes but increases for the case of the 200 mesh size. Further increasing the bias results to an increase in t_{a1+} for all mesh cases with the values being comparable to each other. The 30 mesh case reports the most abrupt change in current over time when compared to the 100 and 200 mesh cases. A similar trend across the mesh sizes however is present. Analysis of the positive peak shows that the presence of the peak for the case of the 30, 100, and 200 mesh sizes start at V_{Bias} = 50, 20, and 10 V respectively. The larges observed peak area can be attributed for the case of the 200 mesh. The values of the peak area at an applied bias of -50, and -100 V become comparable across mesh sizes.

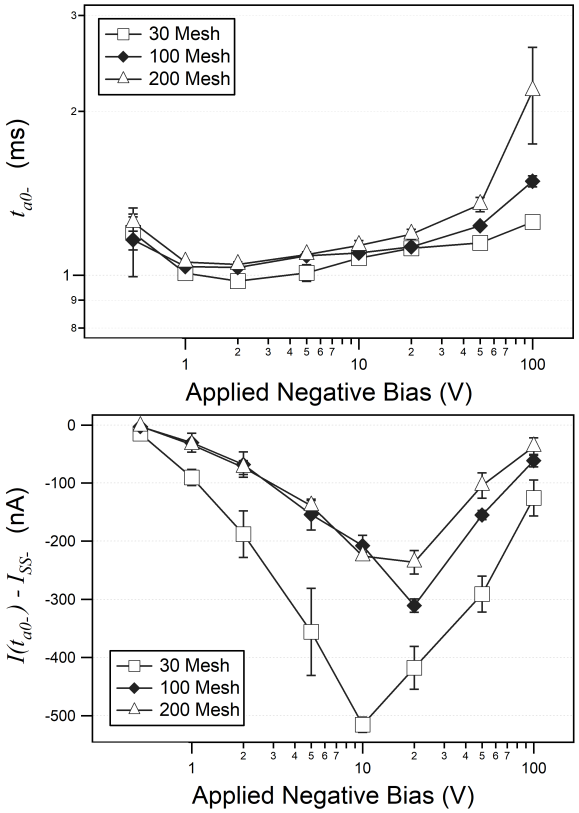

FIGURE 6.6: (Top) arrival time and (Bottom) peak maximum current of the initial negative phase peak.

6.3 Measurement of Electron Mobilities

Typically, during the positive phase electrons are collected near the shutter such that when the succeeding negative phase occurs, electrons are expelled from the area to move towards the detector. The applied negative electric field in the drift tube area should accelerate the electrons collected in the shutter region to move towards the detector. Thereby decreasing the arrival time at higher electric fields as is the case with the measurement of ion mobilities. The results however of t_{a0-} report otherwise wherein a more negative electric fields results to the electrons arriving at a later time.

Due to the highly mobile nature of electrons, some random flux of electrons moving from the plasma source towards the spectrometer is always present. During R2, these electrons are accelerated towards the detector in which a current signal may be obtained from. Evidence of an increasing electron flux towards the detector can be observed from the increasing negative current of I_{SS-}, and I_{SS+} when the electric field is becomes more negative.

In the subsequent time region where upon the onset of the positive potential in R3, electrons from both the plasma and inside the spectrometer experience a strong force of attraction towards the shutter. The electrons inside the spectrometer thus move in a positive electric field with the same magnitude of the negative electric field such that in a more negative electric field, electrons move slower towards the shutter electrode. The asymmetric signal here is thus

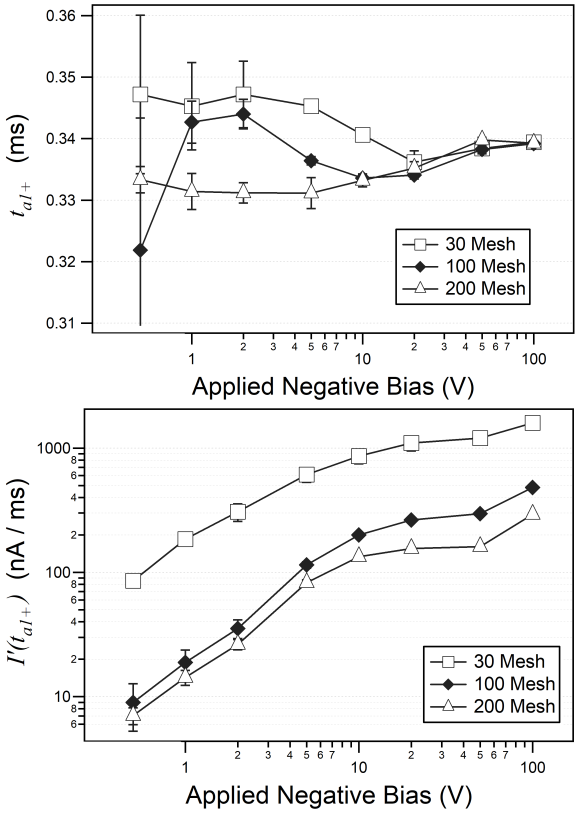

FIGURE 6.7: (Top) arrival time and (Bottom) peak maximum current derivative of the first derivative signal in the positive phase.

a measure of electron retardation in a positive electric field.

Calculating the mobilities using the arrival time values of t_{a1+} and expressing them in terms of the reduced electric field, the results are presented in Fig. 6.9. Since the electrons are highly mobile species and small changes in the applied electric field result to extremely high changes in the velocity of the particle, the original equation for mobilities $v = KE$ remains unchanged. The calculated data reports a mean electron mobility of 81.7, 82.6, and 85 cm^2/Vs corresponding to the 30, 100, and 200 mesh sizes respectively measured at E = 0.33- 33.33 V/cm. The resulting experimental results show a good relation with the values of electron mobilities presented in the LXCat Database.

Using the same values from the LXCat Database, the group of Tejero-del-Caz, developed a simulation tool for the calculation of the two-term electron Boltzmann equation for low-temperature plasmas. The study presents a model for the mobilities of electrons in dry air as a function of the reduced electric field (Fig. 6.10). At a gas temperature of 300 K, the mobilities for the case where rotational excitations/de-excitations involving N_2 and O_2 is shown in the solid black line in the figure here. The case where these rotational/de-excitations are not included is shown in the dashed line here. Observing the trend of the black line with decreasing reduced electric field shows that further decreasing the electric field would result to an exponential increase in the electron mobilities similar to what has been observed in our experimental results.

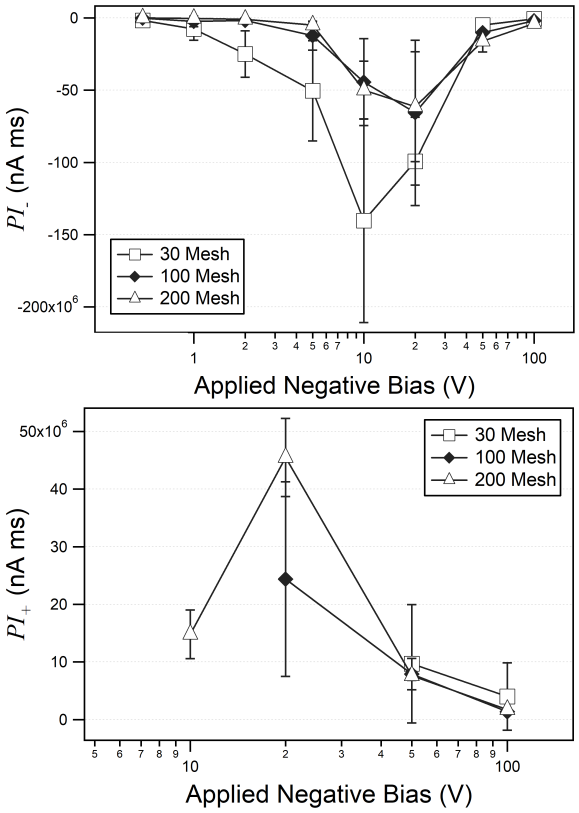

FIGURE 6.8: Peak integral values of the (Top) negative phase peak, and (Bottom) positive phase peak.

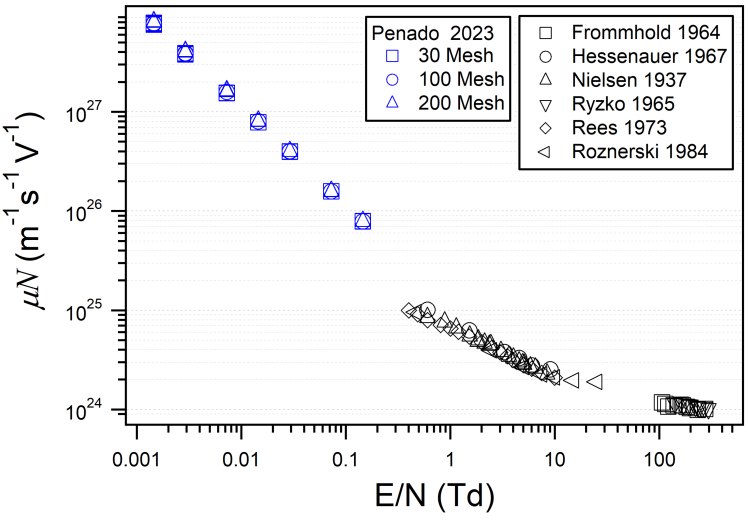

FIGURE 6.9: Calculated reduced mobility values from the positive phase peak first derivative data in terms of the reduced electric field. The mobilities were normalized to 2.55 x 10^{25} m^{-3}, the density of air at STP. Experimental values of electron mobility are compared to the data presented in the LXCat Database. [51]

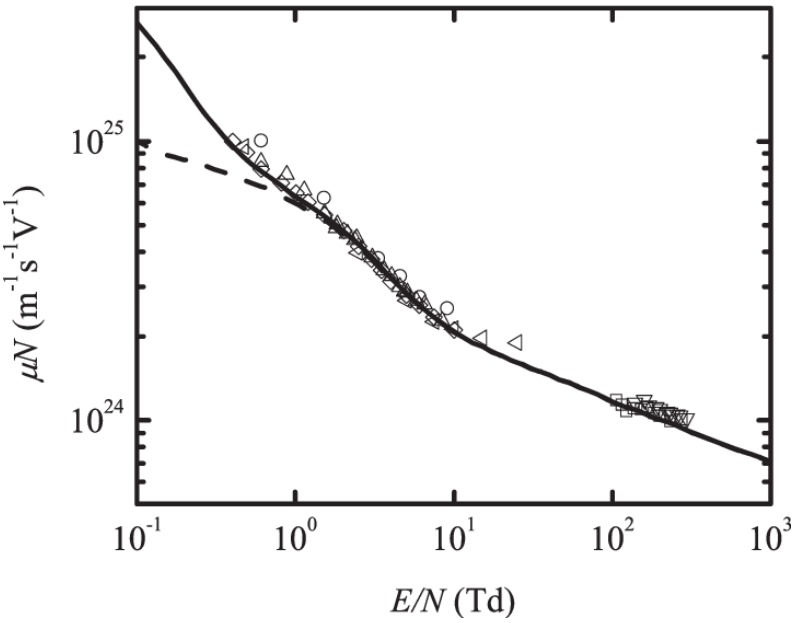

FIGURE 6.10: Reduced electron mobility in dry air in terms of the reduced electric field. Figure was obtained from the publication of A Tejero, et. al. [52].

6.4 Summary

The principle for low-electric field mobility spectrometry for electrons has been studied for diagnostics of an atmospheric pressure plasma source. At negative field intensities of 0.33 V/cm -33.3 V/cm the presence of a phase dependant signal relative to the shutter potential is observed. Results show that during the positive phase, the time at which the first derivative of the signal is maximized is a good measure of the electron mobility of the system. The increasing arrival time in relation to the increasing electric field suggests that a more negative electric field results to electrons moving towards the shutter at a slower velocity. The average electron mobilities measured in this study report electron mobilities of 81.7, 82.6, and 85 cm^2/Vs corresponding to the 30, 100, and 200 mesh sizes respectively measured at E = 0.33- 33.33 V/cm. The values are in accordance with the data presented in the LXCat Database, and simulation results of low-temperature plasmas from the group of Tejero-del-Caz.

Chapter 7

NUMERICAL SIMULATIONS OF CHARGE DENSITY

Experimental results has shown that the phase-resolved behavior of the mobility spectrometer could be used to measure the mobility of ions under atmospheric pressure. To clarify that these results are consistent with first principles assumptions, numerical simulation will be utilized. In the first section of this chapter, we introduce how the Particle-in-Cell (PIC) model could be used to observe the behavior of a swarm as it moves through the spectrometer by approximating the collective swarm behavior with the motion of singular ions interacting with the system. In the second section, we introduce a more practical approach of simulating the ionized swarm by solving the equations of state using the Finite Difference Method applied to the 1D fluid model.

7.1 Single Particle Motion of Plasma

As ions enter the IMS device various forces act upon the particle which include ion transport due to the applied electric field, ion-neutral collisions resulting from the presence of the buffer gas, and ion-ion diffusive, coulombic and collisional interactions from the swarm itself [53]. If we assume that the density of ions is much smaller than the neutral density of the surrounding gas, it can be assumed that the ion-ion interactions are not dominant in the system. Thus, the trajectory of ions can be limited to the effect of coulombic and collisional interactions from the swarm itself.

The force, F, experienced by an ion in the presence of a potential gradient is proportional to the charge of the ion, q, and the surrounding electric field, E, produced due to the distribution of potentials, Φ. The magnitude of the local electric field is equal to the negative gradient of the surrounding potential.

$$\mathbf{a} = \mathbf{E}q/m \tag{7.1}$$

$$\Delta\mathbf{v} = \mathbf{a}\Delta t \tag{7.2}$$

$$\Delta\mathbf{d} = 0.5\,\mathbf{a}\Delta t^2 \tag{7.3}$$

This force due to the electric field is also equal to the product of the mass of the ion, m, and the acceleration it experiences, a, such that for any given distribution of potentials, the local acceleration experienced by an ion is expressed in Eq.7.1. Given a time step, Δt, the change in velocity, Δv, and displacement, Δd, are presented in Eq.7.2, 7.3.

The collision model adapted in this study is detailed in the article by Xu, and Whitten [53]. The results of their study are incorporated into SIMION 7.0, an ion optics simulation program.

The collisions between ions and gas particles are simulated using the hard-sphere collision model and the Monte Carlo method. The probability, P, that a collision will occur is dependent on the ion mean free path, ℓ, the differential velocity, v_{diff}, and the time step, Δt. The mean free path of the ions were calculated using a method presented by Ding, et. al. [54].

$$P = 1 - e^{-|v_{Diff}|\Delta t/\ell} \tag{7.4}$$

$$\ell = \frac{k_b T}{\pi d^2 P\sqrt{2}} \tag{7.5}$$

$$v_{rel} = \sqrt{v_i^2 + \bar{v}_{gas}^2} \tag{7.6}$$

The mean free path is a function of the ion velocity, relative velocity, v_{rel}, the gas density, n, and the ion-particle collision cross cross section, Ω. The relative velocity is calculated using Eq.7.6, where v_i is the ion velocity, and $\bar{v}_{gas}$ is the mean velocity of gas both of which are measure in the laboratory frame of reference. The ion-particle cross section is calculated using the ion radius, r_i, and the gas radius, r_{gas}. A relation between the atomic radius, and particle mass is given in Eq.7.8 [55] assuming a constant volume density.

$$\Omega = \pi(r_i + r_{gas})^2 \tag{7.7}$$

$$d[nm] = 0.120415405\ (m_{ion}[amu])^{(1/3)} \tag{7.8}$$

The resultant probability, P, based on Eqs. 7.4-7.8 determines when a collision will occur; such that if a random number between 0, and 1 is less than P, a collision will occur. The collision model described in this simulation are based upon the findings of Mason and McDaniel [56]. They describe that the collision between an ion and gas particle is similar to that of rigid spheres such that when a collision occurs, there is an equal likelihood that the ion will be scattered in any direction in the center-of mass system.

The velocity of an ion in the laboratory frame of reference, v_{lab}, is given as the sum of the velocity of the ion in the center-of-mass system, v_{cm}, and the velocity of the ion before collision, v [57]. The transformations among these quantities are expressed in terms of the relative mass ratio, r, as shown in the relations below; where m is the mass of the ion, and M is the mass of the gas particles.

$$v_{lab} = v + v_{cm} \tag{7.9}$$

$$v = v_{lab}(1 - r) \tag{7.10}$$

$$v_{lab} = v_{cm}(r) \tag{7.11}$$

$$r = m/(m+M) \tag{7.12}$$

When a collision occurs, the velocity of the ion in the laboratory frame is first transformed the velocity of the ion before collision in the center-of-mass frame (Eq.7.10). The velocity transformations that occur in this frame are expressed in Eqs. 7.13-7.16, from which these are transformed back into the laboratory frame of reference using the relation in Eq.7.11.

$$v_{x,cm} = \sqrt{|v|^2 - (|v|cos\theta)^2}\, cos\phi \tag{7.13}$$

$$v_{y,cm} = \sqrt{|v|^2 - (|v|cos\theta)^2}\, sin\phi \tag{7.14}$$

$$v_{z,cm} = |v|\, cos\phi \tag{7.15}$$

$$cos\theta = 2\, Rand() - 1 \tag{7.16}$$

$$\phi = 2\pi\, Rand() \tag{7.17}$$

The angles θ, and ϕ refer to the azimuthal and polar angles respectively. The $Rand()$ variable in Eq.7.16, 7.17 refers to a random number generated in each algorithm step of the code. The random numbers obtained here must agree with the assumption of the collisional model such that there must be equal instances of ion scattering in any direction.

7.1.1 Particle-in-Cell Simulation of Ion Motion

The particle-in-cell or PIC model is a method used to calculate the motion of the ion as it moves through an external field. PIC assumes four concepts in succession such that given a particle in space with a certain velocity, the particle contributes some charge to the defined grid cell. The additional charge contribution results to a change in the background potential corresponding to a change in the electric field. The particle is accelerated by the resultant electric field and the cycle starts anew. PIC typically use the concept of super particles or ions with the same mass and charge but with amplified space charge contribution to the unit mesh cell in order to minimize the amount of calculations required. Here we define A as the space charge amplification factor such that when A is equal to 0, no space charge was considered in the simulation.

To solve the transport of an ion through the spectrometer, the potential field of the device was first calculated using the AMaze software. For this experiment, the solution space was set to an electrical permittivity of 1.004 for air. The potential of the primary plate was set to 1000 kV to which a voltage drop of 100 V was set for each succeeding ring. This resulted to an electric field of 300 V/cm along the x-axis.

The schematic diagram of the cell model description is shown in Fig. 7.2. The potential field matrix spans the values of x = [-2 mm, 30 mm], y = [-6 mm, 6 mm], and z = [-6 mm, 6 mm] with

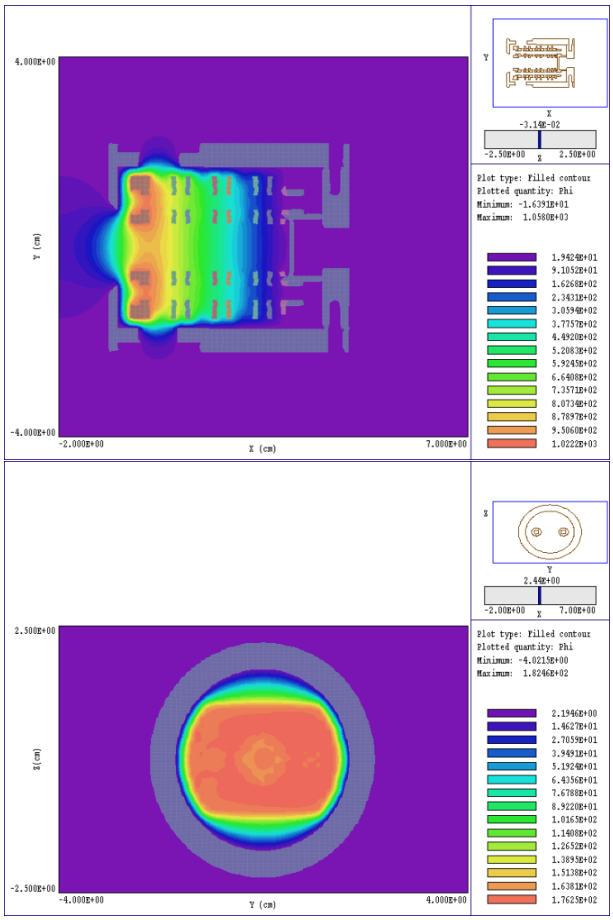

FIGURE 7.1: Potential field distribution along the (Top) z = 0, and (Bottom) x = 10 plane. The potential distribution was calculated using the AMaze software at a $V_{Shutter}$ = 1000 V, and a V_{Bias} = 900 V.

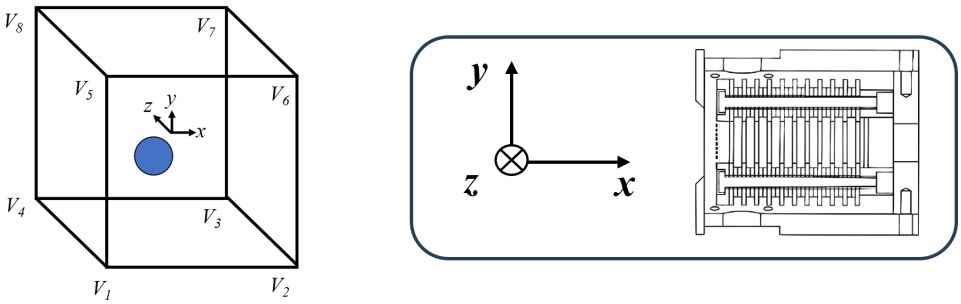

FIGURE 7.2: Schematic diagram of the cell model and the assumed directional planes for the PIC simulation relative to the spectrometer model.

dr = dx = dy = dz = 2 mm. This results to the formation of a cubic grid type potential mesh. The electric field at any given point is equal to the negative gradient of the potential (Eq.7.18). If an ion is located inside a cubic potential mesh unit, the ion will driven by the electric field equal to the average electric fields moving in the said direction as described in Eq.7.19.

To approximate the space charge contribution of each particle to the 8 points that comprise

the cubic potential mesh unit where the particle is located in, the background potential is increased by some voltage as described in Eq.7.20. Here k is Coulomb's constant, q is the charge of the particle, and r is the distance of the particle from the corner of the mesh unit. The space charge is typically amplified with the factor A. This is a simplified approach of approximating the space charge contribution in the spectrometer since the current model is unable to solve the actual space charge according to first principles (Gauss's law).

$$\mathbf{E} = -\Delta V \tag{7.18}$$

$$\mathbf{E_r} = \frac{\Sigma_{r=1}^{4} dV_r}{4dr}\hat{r} \tag{7.19}$$

$$V = A(kq/r) \tag{7.20}$$

The ion trajectory was calculated using the theoretical assumptions presented in the previous section and the 0 mesh case spectrometer design. A flow chart describing the algorithm used for the PIC simulation is shown in Fig. 7.2.

Parameters	Settings
Shutter voltage	1000
Electric field	300 V/cm
Drift length region	30 mm
Time step	3 ns
Beam diameter	0.5 mm

TABLE 7.1: Typical simulation parameters for the PIC code to calculate the trajectory of Ar^+ ions.

The parameters of the experiment are presented in Table 7.1. The simulation calculates the trajectory of a swarm of 10 000 Ar^+ ions starting at the rear of the shutter electrode. The ions are distributed over a radial area with a diameter of 5 mm. The ions are then made to move through the potential field in accordance with the theory presented in the previous section until they are collected at the detector. We consider when A = 0, 10^0, 10^1, 10^2, and 10^3 to observe the effect of increasing ion density in the system. The time step considered in this simulation is 3 ns.

Calculations were done using Visual Studio 2019 in C#. The algorithm was made such that for each time step, the values for time and position were recorded in an external csv file, velocity changes were made first with regards to the potential field followed by the collisional changes, before finally updating the values for position and velocity which will be used in the succeeding iteration. The calculation terminates when the ion reaches the detector.

The spatial distribution of 100 randomly selected ions at varying time intervals are presented in Fig. 7.5 while Fig. 7.4 shows the potential contribution of the entire swarm to the background potential field at similar time intervals. For the case when A is equal to 0, minimal difference can be seen in the shape of the ion potential as time passes. As A is increased to 100, dispersion along the x axis is realized. Observing the spatial distribution of particles for both

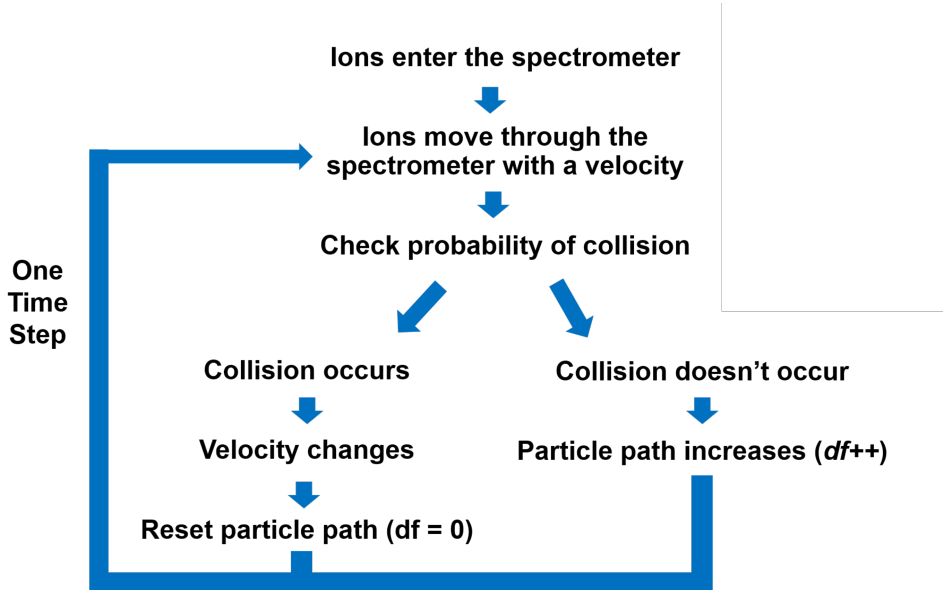

FIGURE 7.3: Algorithm flow chart describing the steps utilized in the particle-in-cell method for calculation of ion densities.

cases at t = 20 μs, an increased dispersion of particles along the x and z axis is realized when space charge effects are considered.

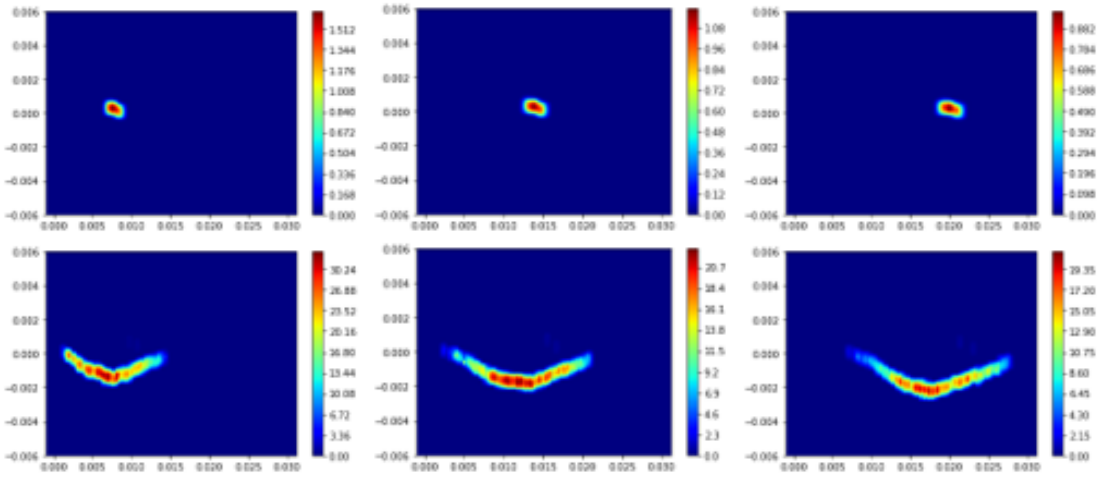

FIGURE 7.4: Observed charge contribution of the ion swarm at t = 10, 20, and 30 μs. The figures above show when A = 0, while the figures below show the behavior when A = 100.

Ion trajectories of randomly selected 100 ions along the xy and xz planes are shown in Fig.7.6, 7.6. The trajectories show a radial beam profile in the xy and xz axis when A = 0 which is a result of independent ions interacting with the electric field. While compression in the y axis and dispersion in the z axis is realized when A = 100. The behavior of the system imitate that of a random walk behavior with a preferential direction moving towards the detector.

A time of flight spectra was constructed by creating a histogram of the arrival times with a width of 0.1 μs from the results of the simulation model (Fig. 7.8). When space charge is

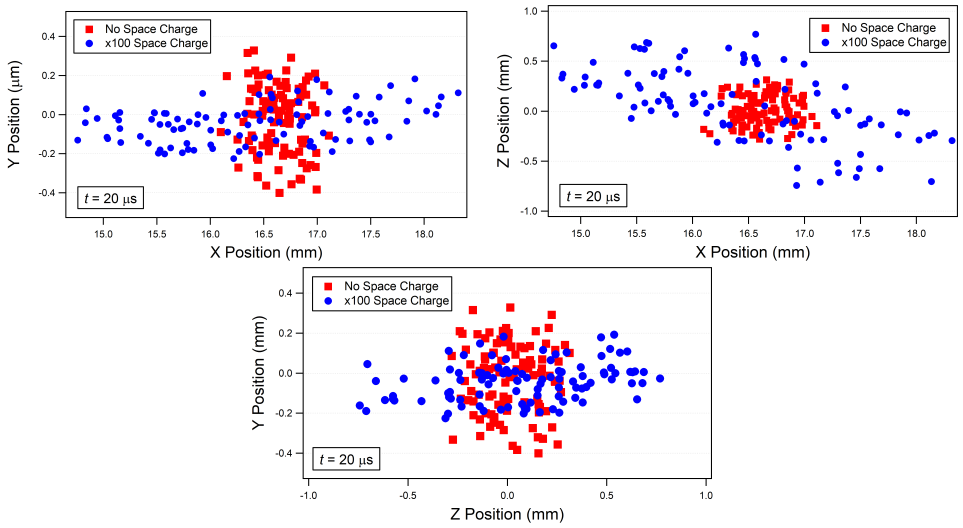

FIGURE 7.5: Ion distribution of 100 random particles at $t = 20$ μs along varying planes. The figures show when $A = 0$, and 100.

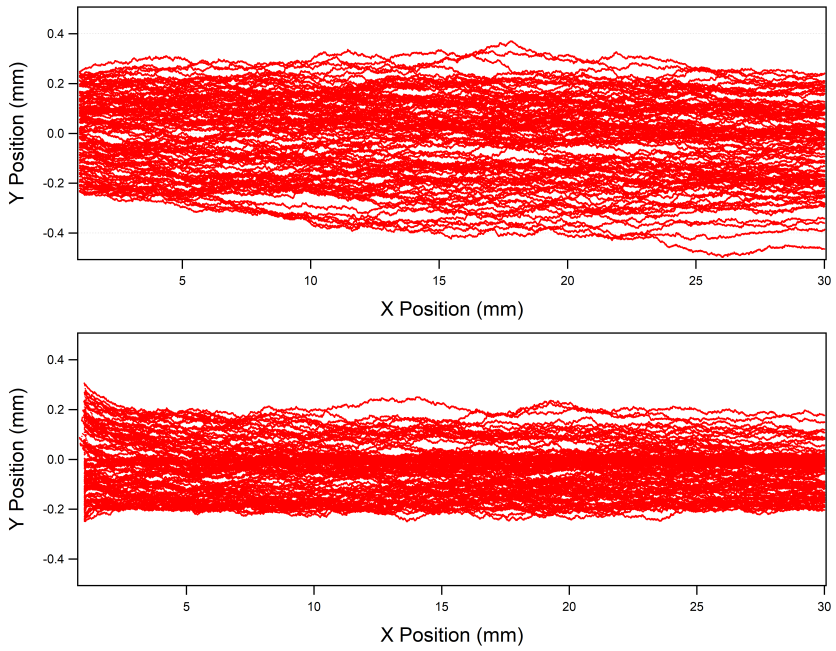

FIGURE 7.6: Ion trajectories of 100 randomly selected Ar^+ ions from the swarm along the xy plane when (Up) $A = 0$, and (Down) $A = 100$.

considered, the number of particles collected at the detector is greatly reduced. Compared to the case when no space charge is considered, the number of particles detected is decreased by 1.3% when the $A = 10^2$, and is further decreased to 56.1% when the space charge when $A = 10^3$. The main loss mechanism in these cases is the loss of charges towards the spectrometer walls as the space charge increases.

Considering space charge also results to an observed shift in the peak arrival time of the ion swarm at the detector, and a broadening of the peak distribution. In particular, for the case

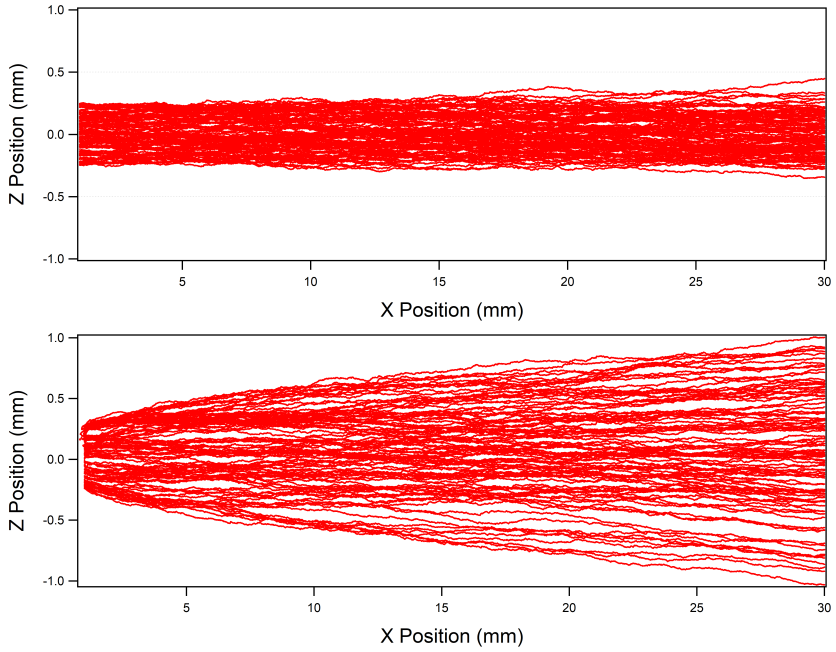

FIGURE 7.7: Ion trajectories of 100 randomly selected Ar^+ ions from the swarm along the xz plane when (Up) $A = 0$, and (Down) $A = 100$.

when $A = 0$, 10^0, 10^1, and 10^2 the arrival times are 51.60, 51.59, 51.45, and 50.75 μs respectively. The corresponding FWHM of the peaks are 0.61, 0.70, 2.79, and 4.46 μs. Results show that the space charge contribution is crucial when considering the motion of ions inside the spectrometer since it changes the time of flight distribution behavior of particles considerably at high densities. Additionally, the broadening of the ion swarm observed here is similar to what can be observed in diffusive effects of ions.

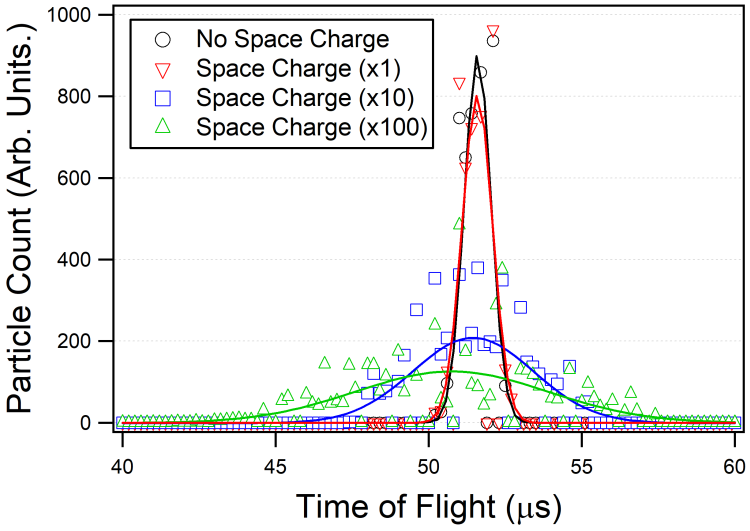

FIGURE 7.8: Time of flight signal of 10,000 Ar+ ions at varying space charge contribution factors. The spectral resolution of the signal is 0.1 μs. A Gaussian convolution was applied to the data values to obtain the peak position and FWHM values of the detector current.

While the PIC method is indeed an effective tool in simulating the behavior of ions as they interact with the ion swarm and the surrounding potential field, the method is computationally expensive especially in low electric fields. As such, a different approach considering the equations of state while building up on the diffusive ion behavior observed from single particle trajectories here is presented in the succeeding section.

7.2 Fluid Behavior of Plasma

Suppose we assume a swarm of ions present in atmosphere moving at a velocity, u, and in the presence of an electric field, E. The flux of plasma through any area could be described by Eq.7.21, where Γ, is the flux, N, is the density, D, is the diffusion coefficient, and, μ, is the mobility coefficient. The first term in the equation is the drift velocity of the charge due to the applied electric field, and other velocity components such as the flow velocity of the neutral gas. The second term is the diffusive component of motion due to the change in the spatial of particles.

$$\Gamma = N(\mu E + u) - D\nabla N \tag{7.21}$$

Under atmospheric pressure, the values of diffusion and mobility coefficients are within 1-2 orders of magnitude in difference making the values comparable. Similarly, results of the PIC code incorporating the space charge contribution resulted to the broadening of the detected peak which is indicative of diffusive effects in the system.

$$\frac{\partial N}{\partial t} + \nabla \cdot \Gamma = q \tag{7.22}$$

$$\frac{\partial N}{\partial t} = -(\mu E + u)\frac{\partial N}{\partial x} + D\frac{\partial^2 N}{\partial x^2} + q \tag{7.23}$$

Applying the flux equation to the continuity equation (Eq.7.22), where q is the bulk sources of creation or loss of particles, the result is a variation of the Fokker-Planck equation in the form of the fluid model. In one dimension, the equation is expressed in Eq.7.23. Although there exists an analytical solution to the equation, given non-linear densities and electric fields, it is difficult to come up to an exact solution to the experimental results.

7.2.1 Finite Difference Analysis of Charge Particle Density

We consider the case of particle densities at center of the spectrometer, and assume the case where no particle recombination or creation occurs ($q = 0$). Solving the 1D Fluid model equation is possible by first discretizing the terms into individual time and position steps (dt, dx). By separating the terms into the densities that occurs at one time step ahead on one side of the equation, and the present densities on the other side, a recursive equation is produced (7.24). The recursive equation can be expanded to the entire spatial domain by rewriting the series of equations as a matrix, where $\boldsymbol{A}$ and $\boldsymbol{B}$ correspond to the coefficient matrix for the densities in the future and current time steps respectively.

$$N_i^{j+1} - \alpha(N_{i+1}^{j+1} - 2N_i^{j+1} + N_{i-1}^{j+1}) + \beta(N_{i+1}^{j+1} - N_{i-1}^{j+1}) = N_i^j - \alpha(N_{i+1}^j - 2N_i^j + N_{i-1}^j) + \beta(N_{i+1}^j - N_{i-1}^j) \tag{7.24}$$

$$\alpha = \frac{D\Delta t}{2(\Delta x)^2} \quad \beta = \frac{-(\mu E + u)\Delta t}{4(\Delta x)} \tag{7.25}$$

Since the present values of densities are known, it is possible to solve for the densities after one time step by taking the inverse of the coefficient matrix, $\boldsymbol{A}$, and multiplying it to the current density values (Eq.7.26), where j, and x are the time, and position indices respectively.

$$N_x^{j+1} = \boldsymbol{A}^{-1}(\boldsymbol{B}N_x^j) \tag{7.26}$$

An advantage of using Finite difference instead of PIC is the faster run time due to the decrease of numerical operations. Finite difference allows the use of a continuous initial density in the spectrometer with no changes in computation time. However, since this method utilize the equation of states to simulate the behavior, then certain molecular phenomena are difficult to include such as the space charge contribution without changing the solution matrices.

7.2.2 Positive Field Density Behavior

Utilizing the AMaze software, the potential field distribution inside the spectrometer was calculated. The simulation defines the shutter at x = 5 mm, and the detector at x = 40 mm. The 2D potential distribution at V_{Bias} = 20, 100 V for the case of the 0 mesh and 30 mesh are presented in Fig. 7.9, 7.9. The 1D electric field at the center of the spectrometer for the same mesh cases are presented in Fig. 7.11, 7.12. While minimal change in the electric field magnitude is observed with the addition of the mesh, a rapid increase in the electric field is observed near the shutter upon the addition of the mesh. The addition of the wire mesh similarly changes the position of the maximum and minimum electric field during the positive and negative phases respectively, from 10 to 12 mm corresponding to the case of the 0, and 30 mesh sizes.

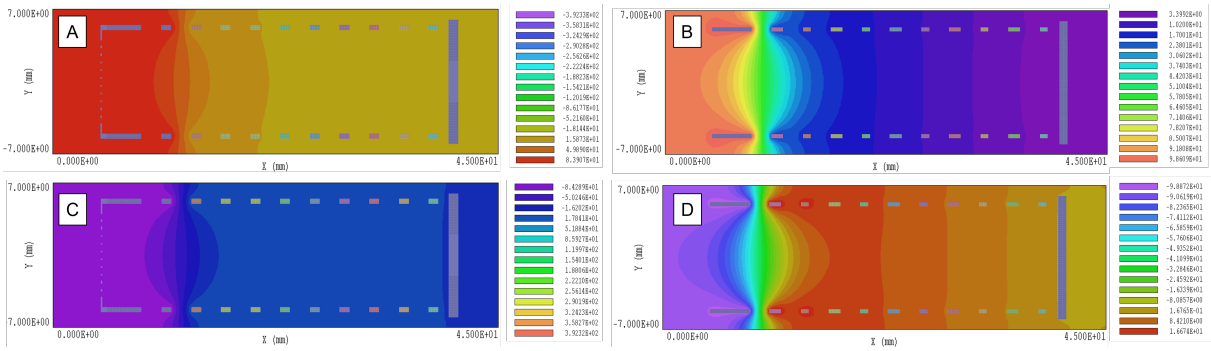

FIGURE 7.9: Potential field distribution inside the spectrometer at V_{Bias} = 20 V. The figures correspond to variations in the shutter potential and applied mesh sizes such that (A) $V_{Shutter}$ = 100 V, 30 mesh size, (B) $V_{Shutter}$ = 100 V, 0 mesh size, (C) $V_{Shutter}$ = -100 V, 30 mesh size, and (D)$V_{Shutter}$ = -100 V, 0 mesh size.

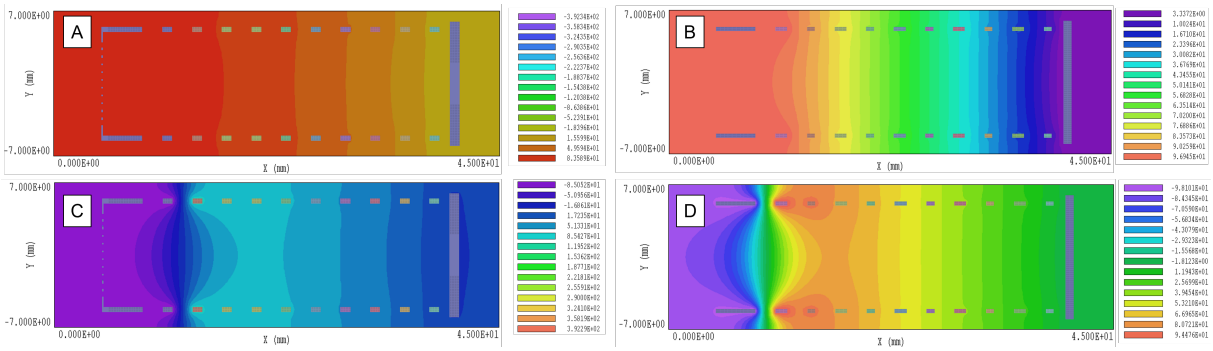

FIGURE 7.10: Potential field distribution inside the spectrometer at V_{Bias} = 100 V. The figures correspond to variations in the shutter potential and applied mesh sizes such that (A) $V_{Shutter}$ = 100 V, 30 mesh size, (B) $V_{Shutter}$ = 100 V, 0 mesh size, (C) $V_{Shutter}$ = -100 V, 30 mesh size, and (D)$V_{Shutter}$ = -100 V, 0 mesh size.

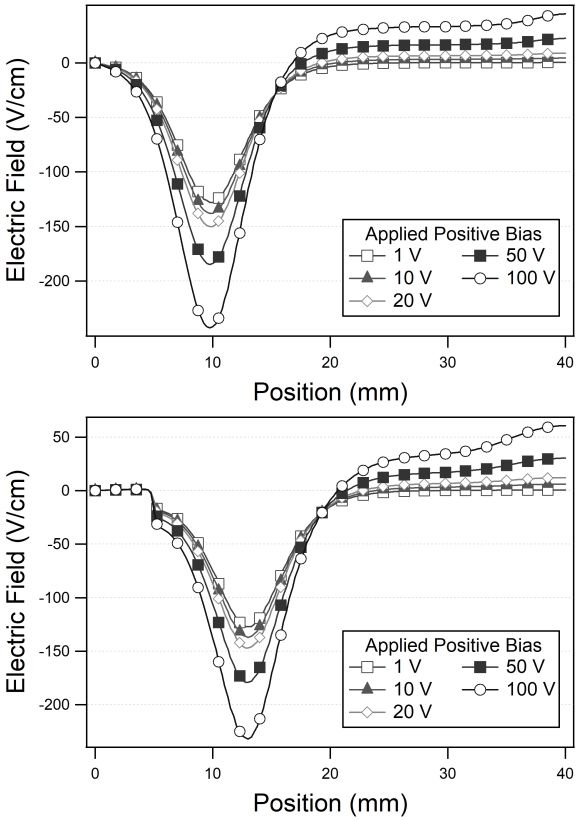

FIGURE 7.11: Apparent electric field at the center of the spectrometer at $V_{Shutter}$ = -100 V for the (Top) 0 Mesh case, and (Bottom) 30 Mesh case.

A flow chart describing the algorithm used for the PIC simulation is shown in Fig. **??**. To simulate the motion of ions in the spectrometer, a constant flow of 1e4 argon ions were made to start at 2.5 mm away from the shutter. The ions are made to move with a velocity v = 0-500 cm/s directed towards the detector, and to interact with the applied electric field. The potential field inside the spectrometer is similar to that done in the experimental work such that the simulation starts first with the negative phase potential map at t = 0 to (50-dt) ms, followed by switching the phase to the positive phase potential map at t = 50 ms to (100-dt) ms. The detector current is defined to be the number of particles at x = 40 mm at any given

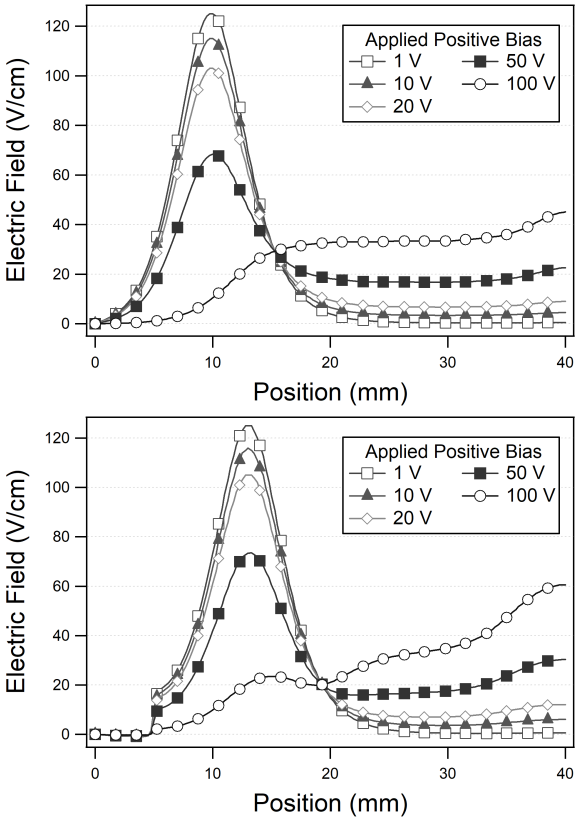

FIGURE 7.12: Apparent electric field at the center of the spectrometer at $V_{Shutter}$ = 100 V for the (Top) 0 Mesh case, and (Bottom) 30 Mesh case.

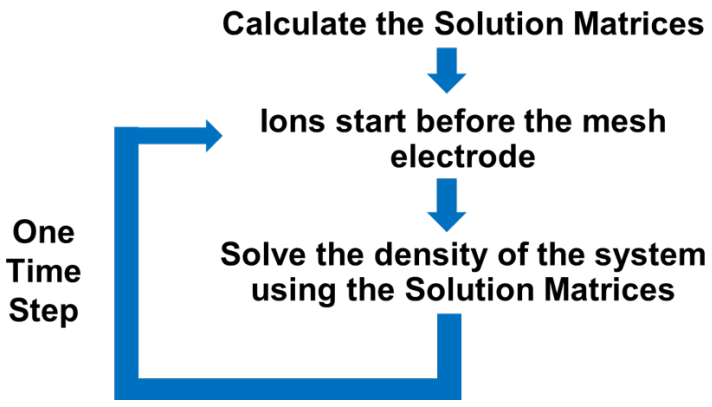

FIGURE 7.13: Algorithm flow chart describing the steps utilized in the finite difference method for calculation of ion densities.

time. The simulation utilizes a dx = 5.625 μm , and a dt = 1 μ. This corresponds to a solution matrix with a size of 8000 x 8000. The process of switching electric potentials is repeated twice to realize a steady state behavior of the electric current at the detector.

The particle densities inside the spectrometer at t = 150 ms is presented in Fig. 7.14. During the negative phase, the presence of a mesh results to a more effective collection of low velocity ions at the mesh surface for all ion velocities during the time V_{Bias} = 20 V. At higher initial velocities, some ions are able to pass through the mesh and can go directly to the detector while

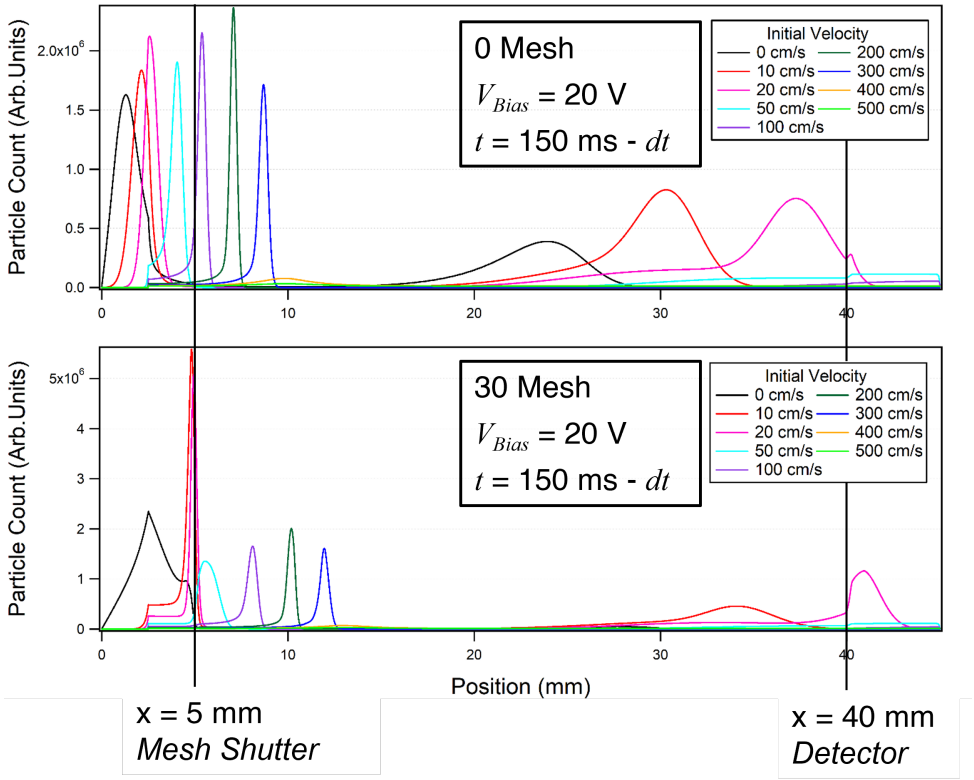

FIGURE 7.14: Distribution of particle densities along the center of the spectrometer at t = 150 ms for the 0, and 30 mesh cases.

those closer to the mesh are electronically collected near the mesh vicinity. These behaviors are more prominent when a mesh is present as compared to the 0 mesh case.

Show in Fig. 7.15, 7.16 are the behavior of particles with $v \geq 100$ cm/s, and $v \leq 100$ cm/s across the two mesh sizes during the second period at t = 100-200 ms. There is no significant effect due to the mesh aperture size for particles with velocities greater than 100 cm/s. In both mesh cases, a peak that maximizes at v = 300 cm/s and decreases in intensity for the 400, and 500 cm/s cases can be observed. For particles moving at a velocity greater than 400 cm/s, a continuous DC offset current is observed. For ions moving at a velocity less than 100 cm/s, the presence of a mesh increases their velocity resulting to the swarm arriving at the detector earlier. This behavior is noticeable for the case of the ions moving at a velocity of 10, and 20 cm/s.

Taking the sum of the signals produced from all velocities for both mesh cases, the number of particles that reach the detector are shown in Fig. 7.17. The results show that the presence of a mesh does not only accelerate the behavior of low velocity ions, but also high velocity ions but to a lesser extent. The earlier arrival times exhibit by the low velocity ions in the spectra allows the elucidation of high energy ions at t = 150-200 ms. This behavior is consistent in low electric fields as seen in the case when V_{Bias} = 1 V, but is not as apparent at higher electric fields as seen in the case when V_{Bias} = 100 V. This behavior supports the idea that the mesh acts as a high pass filter such that it allows the passage of high energy particles but attenuates the passage of low energy species.

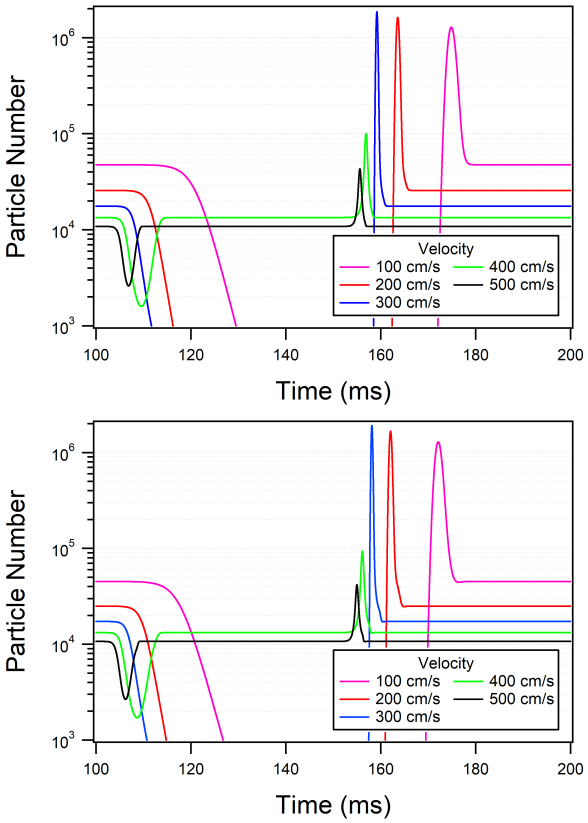

FIGURE 7.15: Observed spectrometer signal for the (Top) 0 mesh case, and (Bottom) 30 mesh case for Argon ions moving at a velocity $v \geq 100$ cm/s.

Simulation results of the electron current at these parameters shows that no electron signal reaches the detector when solving the differential equations. This is likely due to the numerical constraints of the simulation such as the time step, and number of position divisions that limits the observation of such behavior. While it is likely that some random continual flux of electrons reaches the detector, the current simulation is not able to account for these factors.

7.3 Summary

Numerical calculations of the ion transport inside the ambient mobility spectrometer has been conducted using an approximation of the single particle motion of ions, and a collective fluid behavior of the system to simulate the swarm behavior of ion species inside the ambient spectrometer. Utilizing the PIC method, it is shown that the motion of ions as they move across the spectrometer can be likened to that of a random-walk behavior. Additionally, the incorporation of space charge effects inside the spectrometer results to a lower collected signal at the detector, and significant broadening of the signal peak. Both of which are evidences of a diffusive like behavior of the ion swarm as it moves through the spectrometer.

Using the Finite Difference method applied to the 1D Fluid Model allows us to consider both electronic and diffusive behavior of the swarm with lesser calculations when compared to the PIC model. The motion of a continuous ion swarm following the electric field in the typical positive field operation mode of the mobility spectrometer shows that the presence of a mesh

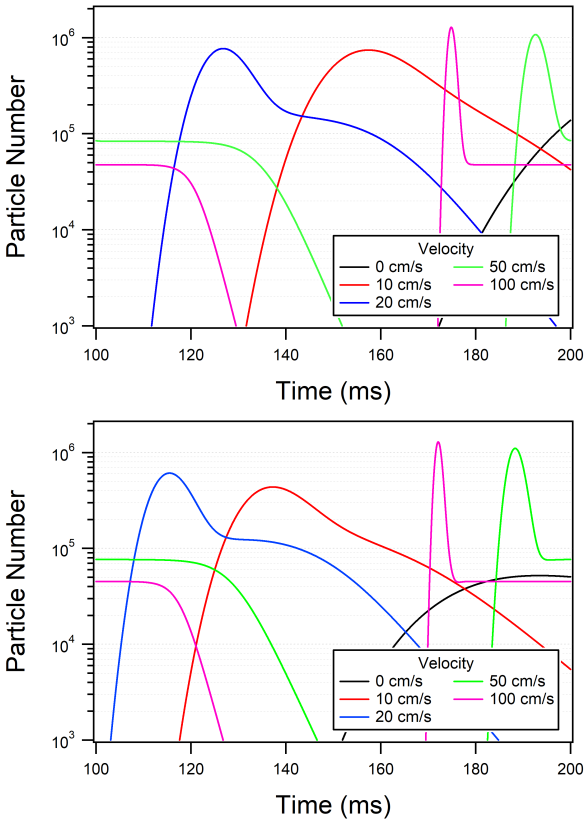

FIGURE 7.16: Observed spectrometer signal for the (Top) 0 mesh case, and (Bottom) 30 mesh case for Argon ions moving at a velocity $v \leq 100$ cm/s.

accelerates the ion swarm at all velocities resulting to shifts in the observed peak behavior. Additionally, the presence of a mesh further accelerates the low velocity ions allowing for better elucidation of the high velocity ion swarm signal. The current model however not account for the transverse diffusion and mobility effects, sources of ionization and recombination sources, and the electron signal.

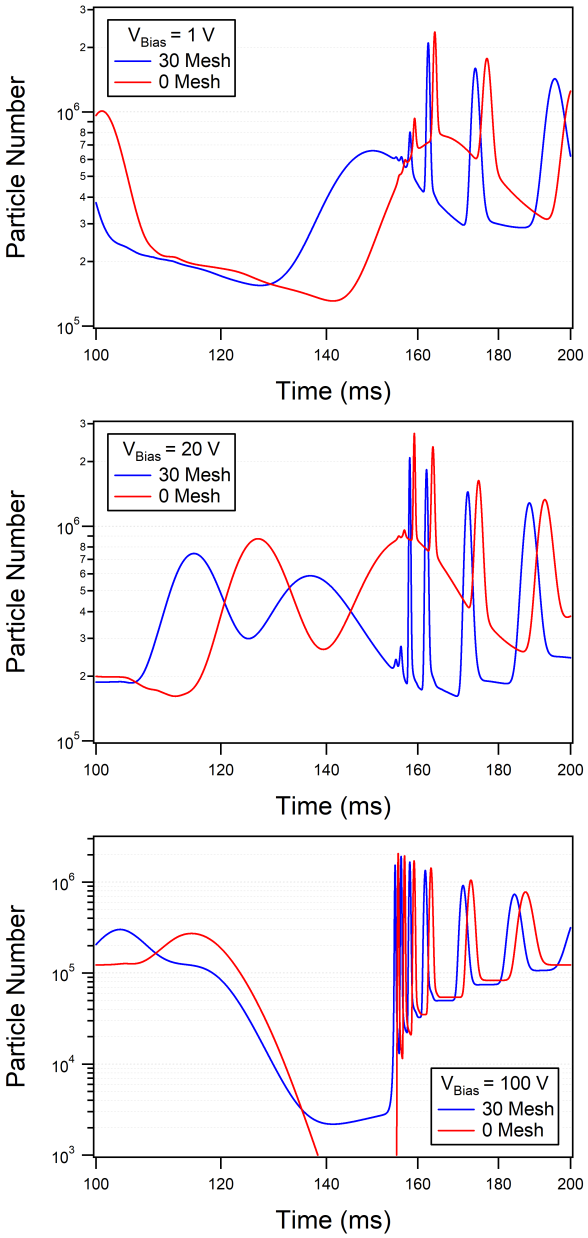

FIGURE 7.17: Observed detector current for a collection of Argon ions moving at initial velocities of v = 0-500 cm/s at V_{Bias} = 1, 20 and 100 V.

Chapter 8

CONCLUSION

The dissertation was able to demonstrate the diagnostics of a capacitively coupled RF AP source using the low-voltage ambient mobility spectrometer. The spectrometer is shown to be capable of identifying a range of mobilities corresponding to ion species and electrons found in the plasma swarm produced by the 13.56 MHz CCP RF source. Upon obtaining a time-resolved signal relative to the applied shutter potential, theories as to the motion of ions and electrons in a positive, and negative electric field respectively were made. These theories were clarified using spectrometer experiments, and numerical simulations. The detailed summary of the results presented in this dissertation are discussed in the remainder of the chapter. Future prospects on the further applications and development of this method are also presented.

8.1 Atmospheric Pressure Plasma Sources

Two configurations of RF AP sources, a capacitively coupled plasma (CCP) source, and an inductively coupled plasma (ICP) source, were developed and characterized for further applications towards ambient ion mobility spectrometry. Double probe analysis, and optical emission spectroscopy was performed on both sources to quantify the behavior of the sources. Both sources show the presence of ionized oxygen in the swarm with the ICP source more effectively ionizing oxygen. Double probe analysis show that the CCP source reports an 70 % increase in n_i when compared the ICP source. Asymmetric behavior in the double probe trace indicate inhomogeneity in the plasma possibly caused in the variations in the motion of ions and electrons in both sources.

Upon coupling to the IMS, only the CCP source was able to present an asymmetric detector signal. While it is likely this effect is due to changes in the localized electric field that makes it difficult for the ICP source plasma to propagate through the mesh, higher input powers in the ICP source results to arcing with the spectrometer mesh. The introduction of an analyte is also difficult with the current plasma sources available since the CCP source does not have enough power to fully ionize the analyte, and the ICP source can not be coupled to the IMS in its current state.

8.2 Ambient Mobility Device

The presence of a mesh at the plasma facing side of the spectrometer results to an observed phase-locked signal at the detector. Even in the absence of an electric field, the time varying voltage at the shutter is enough to produce this type of signal at the detector. Near mesh plasma parameter analysis show that the area between the mesh and the plasma source show limited changes to ion density and electron temperature when a bias is applied to the mesh. Past the

mesh, these parameters vary with the applied mesh bias. The mesh acts as a high-pass filter such that it easily allows highly energetic particles to pass through the area.

While the current system utilizes a square wave at 10 Hz as the typical driving frequency of the system, other frequencies and peak voltages may result to the detection of unique signals where other swarm parameters may be calculated from.

8.3 Analysis of Ion and Electron Mobilities

The principle for low-electric field ion mobility spectrometry for positively charged species has also been studied for diagnostics of an atmospheric pressure plasma source. Analysis of the ion transport in the drift field shows the presence of peaks in the time-of-flight spectrum during the positive phase corresponding to the reduced mobilities of 3.0 cm^2/Vs, and 2.7 cm^2/Vs measured at an applied bias of 100, and 5-50 V respectively. The peak could possibly be attributed to the drift of O^+, and Ar^+ ions inside the spectrometer. Similarly, the principle for low-electric field mobility spectrometry of electrons has been studied for diagnostics of an atmospheric pressure plasma source. At negative field intensities of 0.33 V/cm -33.3 V/cm the presence of a phase dependant signal relative to the shutter potential is observed. The average electron mobilities measured in this study report mobilities of 81.7, 82.6, and 85 cm^2/Vs corresponding to the 30, 100, and 200 mesh sizes respectively measured at E = 0.33- 33.33 V/cm.

The basis of obtaining mobilities of charges species from the asymmetric detector signal is introduced in this study. It is likely that the data analysis technique used here is not the optimal method but one where it is still possible to obtain the mobilities presented in the system. As such optimization of the signal analysis method, and calculations may lead us to understand more about the phenomena of the current observed system.

8.4 Numerical Simulations of Ion Densities

Numerical calculations of the ion transport inside the ambient mobility spectrometer has been conducted using an approximation of the single particle motion of ions, and a collective fluid behavior of the system to simulate the swarm behavior of ion species inside the ambient spectrometer. Evidences of a diffusive like behavior of the ion swarm is shown with the PIC code while the Finite Difference method applied to the 1D Fluid equation supports the high-pass filter characteristics of the mesh at low electric fields.

The current simulation is able to calculate the behavior of the species along the center of the spectrometer, being able to calculate the transverse behavior of particles as well as simulating the near mesh characteristics of the plasma would give us a clearer understanding of the mobility phenomena. This however would require intensive computing power since these calculations should be obtained from first principle assumptions.

8.5 Further Work

The study is one of the first that discusses measurements of ion and electron mobilities at very low electric fields in the absence of a neutral gas. The proof of concept that this method could be applied at this scale opens up the possibility of expanding the theory even further such that we are able to realize the analysis of trace substances even faster than before. Aside from the aforementioned recommendations the author presented in the earlier sections of this chapter- analysis on the resolving power of the system should be the next step, and the improvement on the design of the plasma source such that an analyte substance may be introduced for analysis using the developed mobility spectrometer.

BIBLIOGRAPHY

[1] L. A. Viehland and E. Mason, "Gaseous lon mobility in electric fields of arbitrary strength," *Annals of Physics*, vol. 91, 499–533, 1975.

[2] F. F. Chen, *Introduction to plasma physics*. Springer Science & Business Media, 2012.

[3] M. I. Boulos, P. L. Fauchais, and E. Pfender, "The plasma state," in *Handbook of Thermal Plasmas*, Springer, 2023, 3–55.

[4] A. Schutze, J. Y. Jeong, S. E. Babayan, J. Park, G. S. Selwyn, and R. F. Hicks, "The atmospheric-pressure plasma jet: A review and comparison to other plasma sources," *IEEE transactions on plasma science*, vol. 26, 1685–1694, 1998.

[5] C. Tendero, C. Tixier, P. Tristant, J. Desmaison, and P. Leprince, "Atmospheric pressure plasmas: A review," *Spectrochimica Acta - Part B Atomic Spectroscopy*, vol. 61, 2–30, 2006.

[6] X Lu, G. V. Naidis, M. Laroussi, S. Reuter, D. B. Graves, and K. Ostrikov, "Reactive species in non-equilibrium atmospheric-pressure plasmas: Generation, transport, and biological effects," *Physics Reports*, vol. 630, 1–84, 2016.

[7] F. Massines, C. Sarra-Bournet, F. Fanelli, N. Naudé, and N. Gherardi, "Atmospheric pressure low temperature direct plasma technology: Status and challenges for thin film deposition," *Plasma Processes and Polymers*, vol. 9, 1041–1073, 2012.

[8] P. J. Bruggeman, F. Iza, and R. Brandenburg, "Foundations of atmospheric pressure non-equilibrium plasmas," *Plasma Sources Science and Technology*, vol. 26, 123002, 2017.

[9] Y. Seo, H. W. Lee, H. Kwon, J Choi, S. Lee, K. Woo, K. Kim, and J. Lee, "A study on characterization of atmospheric pressure plasma jets according to the driving frequency for biomedical applications," *Thin Solid Films*, vol. 519, 7071–7078, 2011.

[10] M. Domonkos, P. Tichá, J. Trejbal, and P. Demo, "Applications of cold atmospheric pressure plasma technology in medicine, agriculture and food industry," *Applied Sciences*, vol. 11, 4809, 2021.

[11] P. Dimitrakellis, E. Delikonstantis, G. D. Stefanidis, and D. G. Vlachos, "Plasma technology for lignocellulosic biomass conversion toward an electrified biorefinery," *Green Chemistry*, vol. 24, 2680–2721, 2022.

[12] U. Kogelschatz, "Dielectric-barrier discharges: Their history, discharge physics, and industrial applications," *Plasma chemistry and plasma processing*, vol. 23, 1–46, 2003.

[13] J Hopwood, C. Guarnieri, S. Whitehair, and J. Cuomo, "Electromagnetic fields in a radio-frequency induction plasma," *Journal Of Vacuum Science & Technology A: Vacuum, Surfaces, and Films*, vol. 11, 147–151, 1993.

[14] F. F. Chen, "Radiofrequency plasma sources for semiconductor processing," *Advanced Plasma Technology*, 99–115, 2007.

[15] C. Pattyn, E. Kovacevic, T. Strunskus, T. Lecas, and J. Berndt, "Formation and behavior of negative ions in low pressure aniline-containing rf plasmas," *Scientific Reports*, vol. 9, 10886, 2019.

[16] X. Guo, S. Alavi, and J. Mostaghimi, "Analytical performance of the conical torch in axially viewed inductively coupled plasma optical emission spectroscopy," *Journal of Analytical Atomic Spectrometry*, vol. 34, 2126–2135, 2019.

[17] T. Fujimoto, *Plasma Spectroscopy* (International Series of Monographs on Physics). Clarendon Press, 2004.

[18] I. Langmuir, "The effect of space charge and residual gases on thermionic currents in high vacuum," *Physical Review*, vol. 2, 450, 1913.

[19] F. F. Chen, "Lecture notes on langmuir probe diagnostics," in *Mini-Course on Plasma Diagnostics, IEEE-ICOPS meeting, Korea*, vol. 2, 2003.

[20] L. S. Blair and K. G. Xu, "Langmuir probe diagnostics of an atmospheric-pressure microplasma," 2015.

[21] S Saito, M. Razzak, S Takamura, and M. Talukder, "Development of asymmetric double probe formula and its application for collisional plasmas," *Journal of Applied Physics*, vol. 107, 123306, 2010.

[22] T. R. Tejumola, A. Tanaka, A. Khan, M. Cho, H.-I. P. Team, *et al.*, "Development of low cost double probe plasma measurement system for a lean satellite horyu-iv," *Transactions of the japan society for aeronautical and space sciences, aerospace technology Japan*, vol. 14, Pr_39–Pr_46, 2016.

[23] R. G. Ewing, D. A. Atkinson, G. Eiceman, and G. Ewing, "A critical review of ion mobility spectrometry for the detection of explosives and explosive related compounds," *Talanta*, vol. 54, 515–529, 2001.

[24] M. Mäkinen, M. Nousiainen, and M. Sillanpää, "Ion spectrometric detection technologies for ultra-traces of explosives: A review," *Mass spectrometry reviews*, vol. 30, 940–973, 2011.

[25] J. R. Verkouteren and J. L. Staymates, "Reliability of ion mobility spectrometry for qualitative analysis of complex, multicomponent illicit drug samples," *Forensic science international*, vol. 206, 190–196, 2011.

[26] G. Eiceman, E. Nazarov, B Tadjikov, and R. Miller, "Monitoring volatile organic compounds in ambient air inside and outside buildings with the use of a radio-frequency-based ion-mobility analyzer with a micromachined drift tube," *Field Analytical Chemistry & Technology*, vol. 4, 297–308, 2000.

[27] W. Vautz, D. Zimmermann, M. Hartmann, J. I. Baumbach, J. Nolte, and J. Jung, "Ion mobility spectrometry for food quality and safety," *Food additives and contaminants*, vol. 23, 1064–1073, 2006.

[28] L. Viehland and E. Mason, "Transport properties of gaseous ions over a wide energy range, iv," *Atomic Data and Nuclear Data Tables*, vol. 60, 37–95, 1995.

[29] K. Giles, S. D. Pringle, K. R. Worthington, D. Little, J. L. Wildgoose, and R. H. Bateman, "Applications of a travelling wave-based radio-frequency-only stacked ring ion guide," *Rapid Communications in Mass Spectrometry*, vol. 18, 2401–2414, 2004.

[30] D. R. Hernandez, J. D. DeBord, M. E. Ridgeway, D. A. Kaplan, M. A. Park, and F. Fernandez-Lima, "Ion dynamics in a trapped ion mobility spectrometer," *Analyst*, vol. 139, 1913–1921, 2014.

[31] F. Fernandez-Lima, D. Kaplan, and M. Park, "Note: Integration of trapped ion mobility spectrometry with mass spectrometry," *Review of Scientific Instruments*, vol. 82, 126106, 2011.

[32] I. Buryakov, "Detection of explosives by ion mobility spectrometry," *Journal of Analytical Chemistry*, vol. 66, 674–694, 2011.

[33] D Collins and M Lee, "Developments in ion mobility spectrometry–mass spectrometry," *Analytical and bioanalytical chemistry*, vol. 372, 66–73, 2002.

[34] J. N. Dodds and E. S. Baker, "Ion mobility spectrometry: Fundamental concepts, instrumentation, applications, and the road ahead," *Journal of the American Society for Mass Spectrometry*, vol. 30, 2185–2195, 2019.

[35] N. E. Bradbury and R. A. Nielsen, "Absolute values of the electron mobility in hydrogen," *Physical Review*, vol. 49, 388, 1936.

[36] A. M. Tyndall and C. F. Powell, "The mobility of ions in pure gases," *Proceedings of the Royal Society of London. Series A, Containing Papers of a Mathematical and Physical Character*, vol. 129, 162–180, 1930.

[37] H. Ellis, R. Pai, E. McDaniel, E. Mason, and L. Viehland, "Transport properties of gaseous ions over a wide energy range," *Atomic data and nuclear data tables*, vol. 17, 177–210, 1976.

[38] M. Wiśnik-Sawka, E. Budzyńska, and J. Puton, "Application of ion mobility spectrometry for permeability studies of organic substances through polymeric materials," *Molecules*, vol. 25, 2983, 2020.

[39] J. K. T. Soriano, T. Torii, M. C. C. Lacdan, and M. Wada, "Development and characterization of ion mobility spectrometer," *Plasma and Fusion Research*, vol. 14, 3406093–3406093, 2019.

[40] W. Davis, *Radio Frequency Circuit Design* (Wiley Series in Microwave and Optical Engineering). Wiley, 2011.

[41] J. K. Soriano, "Novel plasma-based ambient desorption/ionization source," PhD thesis, Doshisha University, 2019.

[42] M. C. C. Lacdan and M. Wada, "Characterization of atmospheric pressure plasmas by a gerdien condenser," *Plasma and Fusion Research*, vol. 11, 2401015–2401015, 2016.

[43] V. Godyak, "Rf discharge diagnostics: Some problems and their resolution," *Journal of Applied Physics*, vol. 129, 041101, 2021.

[44] A. Kramida, Yu. Ralchenko, J. Reader, and and NIST ASD Team, NIST Atomic Spectra Database (ver. 5.10), [Online]. Available: `https://physics.nist.gov/asd` [2017, April 9]. National Institute of Standards and Technology, Gaithersburg, MD. 2022.

[45] T. Wegner, C. Küllig, and J. Meichsner, "On the eh transition in inductively coupled radio frequency oxygen plasmas: I. density and temperature of electrons, ground state and singlet metastable molecular oxygen," *Plasma Sources Science and Technology*, vol. 26, 025006, 2017.

[46] K. N. M. Penado, A. V. B. Catapang, and M. Wada, "Low electric field drift tube ion mobility analysis for atmospheric pressure plasma," *Plasma and Fusion Research*, vol. 18, 1406029–1406029, 2023.

[47] M. C. C. Lacdan and M. Wada, "Effect of electrode material to current-voltage characteristics of a gerdien condenser," *Plasma and Fusion Research*, vol. 11, 1401121–1401121, 2016.

[48] T. C. O'Haver, A. F. Fell, G. Smith, P. Gans, J Sneddon, L Bezur, R. Michel, J. Ottaway, J. Miller, T. Ahmad, *et al.*, "Derivative spectroscopy and its applications in analysis," in *Analytical Proceedings*, Royal Society of Chemistry, vol. 19, 1982, 22–46.

[49] M. Santos, A. Cortez, J. Perdigoto, J Escada, R Veenhof, P. Neves, F. Santos, C. Conde, and F. Borges, "Experimental ion mobility measurements in ar-n2," *Journal of Instrumentation*, vol. 13, P11016, 2018.

[50] L. A. Viehland and C. C. Kirkpatrick, "Relating ion/neutral reaction rate coefficients and cross-sections by accessing a database for ion transport properties," *International journal of mass spectrometry and ion processes*, vol. 149, 555–571, 1995.

[51] L. C. Pitchford, L. L. Alves, K. Bartschat, S. F. Biagi, M.-C. Bordage, I. Bray, C. E. Brion, M. J. Brunger, L. Campbell, A. Chachereau, *et al.*, "Lxcat: An open-access, web-based platform for data needed for modeling low temperature plasmas," *Plasma Processes and Polymers*, vol. 14, 1600098, 2017.

[52] A. Tejero-del Caz, V. Guerra, D Gonçalves, M. L. Da Silva, L Marques, N. Pinhao, C. Pintassilgo, and L. Alves, "The lisbon kinetics boltzmann solver," *Plasma Sources Science and Technology*, vol. 28, 043001, 2019.

[53] J. Xu and W. B. Whitten, "Monte Carlo simulation of ion transport in ion mobility spectrometry," *International Journal for Ion Mobility Spectrometry*, vol. 11, 13–17, 2008.

[54] L. Ding, M. Sudakov, and S. Kumashiro, "A simulation study of the digital ion trap mass spectrometer," *International Journal of Mass Spectrometry*, vol. 221, 117–138, 2002.

[55] W. M. Haynes, *CRC handbook of chemistry and physics*. CRC press, 2016.

[56] E. A. Mason and E. W. McDaniel, *Transport properties of ions in gases*. Wiley Online Library, 1988, vol. 26.

[57] S. Luding, "Collisions & contacts between two particles," *Physics of dry granular media*, 285–304, 1998.